Linear and Nonlinear Rogue Waves in Optical Systems

Shanti Toenger

SPIM

Thèse de Doctorat

école doctorale **sciences pour l'ingénieur et microtechniques**

UFC UNIVERSITÉ DE FRANCHE-COMTÉ

Linear and Nonlinear Rogue Waves in Optical Systems

Vagues Scélérates Linéaire et Non-linéaire dans les Systèmes Optiques

SHANTI TOENGER

SPIM

Thèse de Doctorat

UFC

école doctorale **sciences pour l'ingénieur et microtechniques**

UNIVERSITÉ DE FRANCHE-COMTÉ

THÈSE présentée par

SHANTI TOENGER

pour obtenir le

Grade de Docteur de
l'Université de Franche-Comté

Spécialité : **Optique et Photonique**

Linear and Nonlinear Rogue Waves in Optical Systems

Vagues Scélérates Linéaire et Non-linéaire dans les Systèmes Optiques

Soutenue publiquement le 27 Juin 2016 devant le Jury composé de :

JÉRÔME KASPARIAN	Rapporteur	Professeur à l'Université de Genève
ARNAUD MUSSOT	Rapporteur	Professeur à l'Université de Lille 1
GOËRY GENTY	Examinateur	Professeur à l'Université technologique de Tampere
MARC HANNA	Examinateur	Professeur à l'Institut d'Optique Graduate School
HERVÉ MAILLOTTE	Examinateur	Professeur à l'Université de Franche-Comté
JOHN M. DUDLEY	Examinateur	Professeur à l'Université de Franche-Comté

Acknowledgements

It would not have been possible to write this doctoral thesis without the help and support of people around me, to only some of whom it is possible to mention here.

First and foremost, I would like to thank my supervisor, Prof. John M. Dudley, who had offered the opportunity to work in this fascinating, interdisciplinary area of research. During these three and a half years, I have learned a lot, not just from the academic point of view but also in many aspects of life. I am truly grateful for his invaluable guidance, encouragement, and example, from where I have learned the importance of focus, efficiency, and discipline in giving one best contribution. My sincere appreciation in particular for his support, patience, and understanding during this period of research.

I would like to thank all of the collaborators who contributed to the work included in this thesis, in particular Prof. Goëry Genty and Prof. Frédéric Dias, who have supported the completion of this work with their expertise. I also thank other collaborators, Minh, Cyril, Luc, Amaury, Mikko, Benjamin, Thomas, Yves, Miro, Thibaut, Jean-Marc, Laurant, Pierre-Ambroise, some of whom I have had the opportunity to work with and to learn from, both for the experimental work in the lab and the numerical simulations. My sincere gratitude also to my dissertation committee, Professors Hervé Maillotte, Jérôme Kasparian, Arnaud Mussot, and Marc Hanna, for their insightful comments, questions, and for letting my defense be an enjoyable moment.

I would also like to take this opportunity to record my sincere thanks to several people for their significant contributions to the completion of this thesis. I am especially grateful for the assistance given by Imad Faruque during the time this thesis was being written up. His support and guidance have been a great encouragement to the completion of this thesis. Special thanks to Rachel Yates for the generous time she has spent to proof-read this manuscript. Her prompt feedback has improved the quality of the manuscript and speeded up the writing process.

I am very grateful for all the amazing friends I have here during this period of time, who have made Besançon my home. The lab has been a wonderful place surrounded by warm and open-hearted people. Great time spent inside and outside of the lab, having lunch and sometimes dinner together, countless fun and enjoyable moments spent together not only with the fellow students in Optics but also with those from MN2S department is something I will always remember. I also thank those with whom I have shared the office most of the time, Irina, Bicky, Souleymane, Remi, Ismail, who have made the office a comfortable and stimulating place to work. Outside the lab, I am especially grateful for the community of Bonne Nouvelle church and Groupe Biblique Universitaire, who have always been very welcoming and caring. Your love and patience have also made the language difference not to be a barrier but a truly enjoyable moment of learning.

Finally I would like to thank my parents for their support and encouragement throughout my life. I am grateful to be raised in a family that values curiosity, passion, and freedom. Especially I dedicate this work to my mother who has always been a great example and a good friend.

Contents

List of Figures

List of Tables

Chapter 1

Introduction

We experience randomness in many aspects of our lives. In most cases, the random fluctuations vary over a limited range around some average value, and higher events occur with significantly lower probability, to the extent where their occurrence can be ignored. However, in some cases, events which are far from the average occur more frequently than expected. For example, studies show that typically around 20% of a population owns 80% of the wealth, or 20% of products (or customers) bring in 80% of the revenue, which is known as the Pareto principle [9–11]. In this case, the statistical population follows a heavy tailed distribution, a probability distribution with an outlier component ("tail") that is "heavier" than an exponential probability distribution [12]. Essentially, this means that events that are further from the average happen more frequently than expected.

In nature, similar phenomena are observed in the ocean, and these are generally known as "rogue waves" [13–17]. A rogue wave can be conveniently described as a huge wave with height much higher than the average, which suddenly appears and disappears in the ocean without any trace [18]. The unpredictability and intense power of rogue waves have made them notorious in sinking ships and damaging human constructions such as oil rigs. Rogue waves, however, were only considered as parts of mariners' tales and legends, until one was recorded quantitatively at the Draupner platform in the North Sea on January 1, 1995. The crest of this rogue wave reached an amplitude of 18.5 m with wave height of 25.6 m, which is more than twice the significant wave height (defined as the average of the largest one third of wave heights) of ~ 10.8 m [19].

This first scientific evidence of rogue waves in the ocean led to an extensive statistical study of such extreme events and their underlying mechanisms. The suggested mechanisms behind their appearance can be usefully categorized into linear interactions and nonlinear interactions, each of which has its own limitations (discussed in Chapter 2) [16]. Depending on the particular study, some of these mechanisms have been favoured over others, but no consensus has been reached on any single mechanism being the most influential [14, 20].

One significant challenge in the study of oceanic rogue waves comes from the lack of extensive experimental data due to the limitations of measurement techniques. To date, there is still a scarcity of actual field measurements of rogue waves [2, 21]. Moreover, the availability of reliable measurement data only from in-situ measurement techniques limits the possibility of understanding

the space-time localisation property of rogue waves. A sophisticated imaging technique with the capacity of measuring the spatio-temporal dynamics of ocean waves therefore still needs to be developed [15].

On the other hand, rogue wave phenomena have also been observed in other physical systems such as in the atmosphere [22], plasma [23], Bose-Einstein condensates [24], microwaves [25], and optics [26]. These rogue waves manifest in different physical systems over a wide range of scales (dimensions), yet sharing similarities with ocean waves such as the interplay of linear and nonlinear effects. If the rogue waves in different physical systems have the same underlying mechanims, then understanding the emergence and propagation of rogue waves in one system can be expected to strengthen the understanding in other systems. In particular, rogue waves in the ocean and in optics are known to share similar physical laws such as reflection, refraction, diffraction, dispersion, interference and nonlinearity. Since optical experiments can be conducted relatively easily, studying optical rogue waves can be beneficial in providing insight into the study of oceanic rogue waves [6, 27].

This thesis aims to contribute to clarifying the links (under certain conditions) between oceanic and optical rogue waves, in systems that support both the linear and nonlinear mechanisms of their emergence. The main purpose of this thesis is to understand the mechanism of oceanic rogue waves by means of optical systems. The outcomes of this study can be beneficial to predict and to control the appearance of rogue waves in the ocean and in optical systems. Although it is not the purpose here to investigate the universality of the underlying physics of the systems under study, this research does not restrict the possibility of extending the findings to other physical systems behind optics and oceanography. Indeed, the existence of a generic mechanism underlying the emergence of rogue wave phenomena is still under intense discussion [3, 28].

Understanding the physics of rogue waves is important not only to prevent a particular system under study from potentially hazardous impacts, but it can also provide a promising way to generate highly localised and intense waves. In optics, it can for example be beneficial for the generation of high intensity optical pulses and supercontinuum in optical fibre [29–31], and the formation of high intensity field in spatially extended optical systems, localised in space [32, 33] or in both space and time [34, 35].

1.1 Outline of the thesis

The thesis is a compilation of the research done by the author during a three and a half year period from 2012-2016. The work has been done under collaboration with several international institutes, including University College Dublin, Tampere University of Technology, University of Auckland, and the University of Québec.

The systems used in the course of this study are based on light propagation in the free space and in an optical fibre, where the first system is used to study the linear mechanism of rogue wave formation and the second is used to study the nonlinear mechanism based on the nonlinear Schrödinger equation (NLSE). Some parts of the results presented in this thesis have been published in several articles (or submitted for publication) during the period of the thesis, where the list can be found at the end of this manuscript.

The thesis is organized as follows.

We begin with a brief overview of the study of rogue waves in Chapter 2, focussing on hydrodynamic and optical systems. In this chapter, we first introduce the general definition of rogue waves and their emergence in different physical systems. We then discuss the statistical properties and the criteria used for classification of extreme events as rogue waves in oceanography and optics, followed by a detailed comparison between the generating mechanisms of these phenomena in both systems. For each system, both linear and nonlinear rogue wave generating mechanisms are presented, showing the similarity of these mechanisms in both systems.

In Chapter 3, we study the linear mechanism of rogue wave formation in a spatial optical system, consisting of free space propagation of a phase modulated optical beam. We investigate the link between the focussing of random phase spatial field in terms of caustics and the formation of rogue waves.

Nonlinear mechanism of rogue wave formation due to modulation instability (MI) described by the NLSE are then studied in Chapter 4 to 6. Theoretical aspects of modulation instability in terms of analytical solutions of the NLSE are covered in Chapter 4. In this chapter, we present a detailed numerical study on the formation of rogue waves from noise triggered modulation instability. We compare the spatio-temporal characteristics of the spontaneously emerging localised structures and the analytic solutions to the NLSE, and we perform various statistical analysis in the context of rogue waves.

The experimental realisation of this numerical study is then presented in Chapter 5. Real-time temporal measurements of spontaneous MI field generated in an optical fibre are realised using a time-lens magnifier system, where the large amount of data acquired allows us to perform statistical analysis on the recorded MI pulses.

In contrast with the last two chapters, we study in Chapter 6 the generation of modulation instability triggered by coherent and partially-coherent weak perturbation. The purpose of this study is to investigate the control aspect of the modulation instability, which may be beneficial to the generation or the stabilisation of rogue waves. We focus in this chapter on the frequency-domain properties of the stimulated MI field obtained both from numerical simulations and real-time spectral measurements based on the dispersive Fourier technique.

Finally, Chapter 7 presents some final remarks about this work and summarises its contributions, followed by a brief discussion and perspectives for future developments in this area of study.

Chapter 2

Rogue waves in the ocean and in optics

The phenomena of rogue wave have been a subject of intense study in oceanography over the past few decades. Apart from their general definition as unexpectedly large waves, however, there is still no precise definition that is commonly agreed, and their generating mechanisms are still under investigation [14, 20]. Furthermore, several possibilities have also been suggested, but there is no one universal process that can be identified.

> "They have, over the past twenty or thirty years, come to be recognized as a unique phenomena albeit with several possible causes."
>
> - National Weather Service / National Oceanic and Atmospheric Administration (NWS/NOAA), October 15, 2012

This chapter begins with a brief introduction on the definition of rogue waves commonly used in oceanography, followed by brief historical accounts and documented observations of these unexpectedly emerged giant waves in the ocean. This discussion is not aimed to present an exhaustive review of the phenomena, but to give a general background which is necessary to the study of rogue waves. Subsequently, the statistical properties of rogue waves in the ocean and in optics and the criteria commonly used in their characterisation are discussed.

On the interest of exploring the analogy of oceanic rogue waves and the optical counter part in detail, separate discussions on the physical mechanisms of rogue wave formation in both systems are presented, including both the linear and the nonlinear mechanisms. The former serves as a background study for Chapter 3 while the latter provides important context for Chapter 4, 5, and 6. The comparison of rogue wave generating mechanisms in both systems concludes the chapter, where we show that the analogy established in both systems implies that under some circumstances optical systems can be useful in the study of rogue waves in hydrodynamics.

2.1 General introduction to rogue waves

Rogue waves in the ocean

The term "rogue wave" was first introduced in oceanography to describe a huge wave that appeared unpredictably on the ocean surface. This term is used interchangeably with the term "freak wave", which was first introduced in scientific context by Draper [36]. This kind of giant oceanic wave that emerges unexpectedly from the sea with great destructive power and cannot be explained by other causes is also called "giant wave", "extreme wave", "monster wave", or even "killer wave". Interestingly, despite of different accounts from mariners encountering them, there are remarkable similarities between their description of these rogue waves. In general, their appearances may be specified as single waves, wave groups (sometimes called "three sisters"), pyramidal waves, walls of water, or holes in the sea. Some other terminologies are also used in the literature, such as "Steep Wave Events" [37], or "waves that appear from nowhere and disappear without a trace" [18].

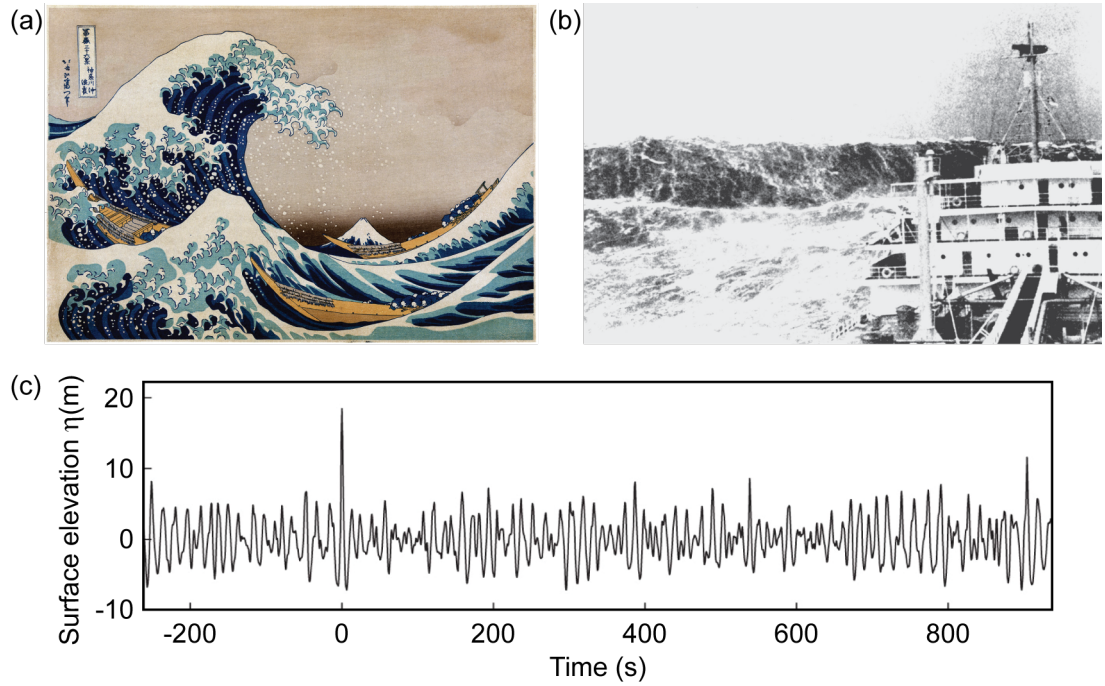

Figure 2.1: (a) The Great Wave off Kanagawa depicting rogue waves emergence. (b) Example of rogue wave in the form of "wall of water" emerging in the ocean. (c) The surface elevation time history of the Draupner wave measured by a down-looking laser device. *Source:* from Ref. [1].

The encounter with giant waves has been reported by seafarers in many occasions. An early example is reported by Captain Dumont d'Urville, a French scientist and naval officer in command of an expedition in 1826, and his colleagues, where they reported encountering waves with heights up to 30 m [15]. In 1933, the U.S. Navy oiler USS Ramapo encountered a huge wave of about 34 m (the height is triangulated by the crew) in the North Pacific. In 1942, Royal Mail Ship (RMS) Queen Mary, carrying 16,082 American soldiers from New York to Great Britain, was hit by a rogue wave that was estimated at height of 28 m, nearly capsizing the ship. Many other encounters have been reported, some of which are listed in Ref. [38] and [15].

Apart from the various accounts of seafarers' encounters with the giant waves, these phenomena have also been captured in paintings. For example, a famous woodcut print dating from ca. 1829 to 1833 "In the Hollow of a Wave off the Coast at Kanagawa" (also known as "The Great Waves") by the Japanese artist Katsushika Hokusai (Fig. 2.1(a)). This painting depicts a huge wave threatening boats, recently interpreted to be a rogue wave [39, 40].

Reliable quantitative recording of rogue waves by measuring instrument, however, was not made until January 1st 1995, when a giant wave with a crest height of 18.5 m above mean sea level hit the Statoil Draupner platform in the central North Sea off Norway (Fig. 2.1(b)). The wave height, defined as the vertical distance between the wave crest and the proceeding or the following trough (see Fig. 2.2), was 25.6 m, while the significant wave height (averaged over 20 min) was about 11.9 m. This giant wave, referred to as the "Draupner wave" or the "New Year's wave", has then generated much interest in rogue wave study and the collection of more evidence from different locations around the world [41–44].

Indeed, observations of rogue waves from testimonies of reported accidents are insufficient to carry out careful study on this phenomenon. Instrumental measurements providing data for quantitative analysis are needed. To date, several in situ instrumentation techniques that can track the surface elevation of the water (laser and radar altimeters, buoys, and subsurface instruments such as pressure gauges and acoustic devices) have been used [15, 45].

The number of rogue waves being recorded, however, are still very limited. The chance of detecting rogue waves from time series measurement is very small. As reported in Ref. [15, 21], multiple years of measurement done in different areas under different conditions and different devices result only in thousands of measured rogue waves. Moreover, the recorded waves taken at different conditions of sea do not compose a statistically uniform ensemble. Hence, there are no solid rogue wave data sets available that can be readily used to establish a realistic probability for rogue waves, and be compared to the theoretical analysis and wave simulations.

Improvement on the measurement techniques for rogue wave detection has therefore been a continous effort. In particular, reliable measurement data to date can only be obtained by in-situ measurement techniques mentioned above, while space-time measurement data covering large area of the sea surface are needed for the study of rogue wave formation. Satellite-based radars covering large spatial scales have been proposed, but the data have been shown to be not reliable enough [46–48]. Although covering only a small area of the ocean, another approach has recently been demonstrated to be an effective technique for space-time measurement by using of stereo video imaging and variational reconstruction techniques, from where space-time wave statistics can be derived [49–51]. These results also provide the first experimental proof that a space-time extremum is generally larger than that observed from a time series measurement.

Rogue waves in optics and other physical systems

The understanding of physical mechanisms generating rogue waves remains a very difficult task despite the enormous amount of study conducted into oceanic rogue waves. An alternative approach is therefore suggested through experiments in other physical domains possessing similar properties. Indeed, some qualitative and quantitative links between wave propagation in hydrodynamics and other physical systems have been known, in particular in optics. It is

therefore natural to consider the possibility of studying this phenomena in optical systems where an analogy in both systems can be drawn.

The analogy between nonlinear wave propagation in optics and hydrodynamics has been known for decades, where the focussing nonlinear Schrödinger equation (NLSE) applies in both systems in certain limits. The description of instabilities in optics as "rogue waves", however, is recent. In late 2007, significant experiments linking extreme events of fibre optical system with the generation of oceanic rogue waves were reported by Solli *et al.* [26]. The fluctuation of shot-to-shot instabilities in the nonlinear optical spectral broadening process of supercontinuum generation was shown to contain a small number of statistically-rare "rogue" events, where it yields long-tailed histograms for intensity fluctuations at long wavelengths. This extreme enhancement of spectral bandwidth was shown to generate localised temporal solitons with greatly increased intensity, which is linked to the generation of oceanic rogue waves. These results were intriguing and important, suggesting new possibilities to explore extreme value dynamics in a convenient benchtop optical environment. Therefore, it attracted broad interest of study and essentially opened up a new field of "optical rogue wave physics".

The growth of interest in the study of optical rogue waves has led to a considerable effort to study rogue wave phenomena in other areas of science as well [20]. The experimental realisations reported since 2007 include weak turbulence in superfluid Helium [52], transport in microwaves systems [25], parametrically driven capillary waves [53], and plasmas [54]. Numerical simulations in different contexts have also been performed, such as in plasmas [23], Alfvén waves [55], and Bose-Einstein condensates [24]. Consequently, what is generally accepted as the meaning of the terminology of 'rogue wave' is now very broad: a high amplitude event in a system appearing in the tails of an associated probability distribution which satisfies particular statistical criterion [6, 20, 56].

2.2 Rogue wave statistics

Propagation of waves can in principle be described by deterministic physical models, which implies that the evolution is predictable given the initial state. Waves travelling through a complex system, however, are known to exhibit randomness and the emergence of extremely large waves [57]. In the case of ocean wave, this unpredictability of the wave dynamics is due to the complexity of the system and incomplete information about the initial state of the system [15]. Whilst in the case of optical wave, randomness is introduced by different factors depending on the optical system under study, as investigated for example in Ref. [58]. In both systems, nonlinearity can lead to a sensitive dependence to initial conditions behaviour (also known as chaos) which increase the randomness of the wave dynamics.

Statistical approach is therefore an important aspect in the study of rogue waves. Even though evolution of the random wave cannot be predicted, their statistical properties can describe the dynamics of the realisation and can be used to estimate the probability of a particular wave condition. The statistical properties of the wave dynamics can be obtained from a direct measurement, stochastic simulations (using deterministic models to compute a number of random realisations), or a direct computation of the statistical wave parameters of a certain

model. The study of rogue waves, as extremely rare and intense events, can therefore not be separated from its statistical properties [59].

In this section, we discuss the statistical criteria commonly used in defining rogue waves. Although a universal description of rogue waves has not been defined, in general, two criteria are often used either independently or simultaneously in the study of rogue waves. The first one is the deviation of the probability from the one predicted by the standard models, which is often associated with the Gaussianity of the distribution. While the second one is the exceedence of the waves above a certain defined threshold. A brief summary of the criteria used in both oceanic and optical rogue waves study is given, where we shall see that the criteria used in optics are often adopted from those used in oceanography.

2.2.1 Deviation of distribution from the standard model

Ocean waves

Ocean wave evolves as a function of space and time in an irregular and unpredictable way, manifesting a random wave dynamics. Although any random system has a chance to produce extreme events, an important concern is when can we actually say that a system statistically exhibits the appearance of a rogue wave. A common definition of rogue waves adopts the nomenclature of Bacon [60] on freak waves, they are 'defined as waves of a height occurring more often than would be expected from the "background" probability distribution', contrasting them with other large amplitude waves representing the tail of some typical statistical distribution of wave heights (generally a Rayleigh distribution) [61, 62]. However, this distinction is not always made, and the term rogue waves is also often used when referring to "classical" extreme events (described by conventional physics, models, and statistics) [63].

Statistical properties of ocean waves based on the simplest linear model was developed by Longuet-Higgins in 1952 [64]. In this work, ocean wave is comprised of a superposition of a large number of wave components with different frequencies and directions, with random relative phases. Under assumption that the frequency dispersion of the wave is not too large (the wave spectrum is narrowband), he exploited the central limit theorem to derive a large number of statistical properties of such random wave superpositions [64, 65]. In particular, he showed that under this hypothesis, the wave components are decorrelated and the resulting surface elevation η is described by a Gaussian distribution, while the wave envelope A is described by a Rayleigh distribution.

The wave envelope is defined as the smooth curve outlining the crests (or troughs) of the wave, which is plotted as dashed line in Fig. 2.2. In this definition, waves are described in terms of an underlying series of individual sinusoidal (carrier) wave cycles being slowly modulated by the envelope. The wave envelope $A(t)$ at a particular location is related to the surface elevation $\eta(t)$ through

$$\eta(t) = A(t)\cos(\omega t),$$

where ω is the frequency of the wave.

However, although wave envelope is a well defined mathematical quantity, the physical quantity wave height $H(t)$ is in general preferred, which is defined by the total vertical distance from the

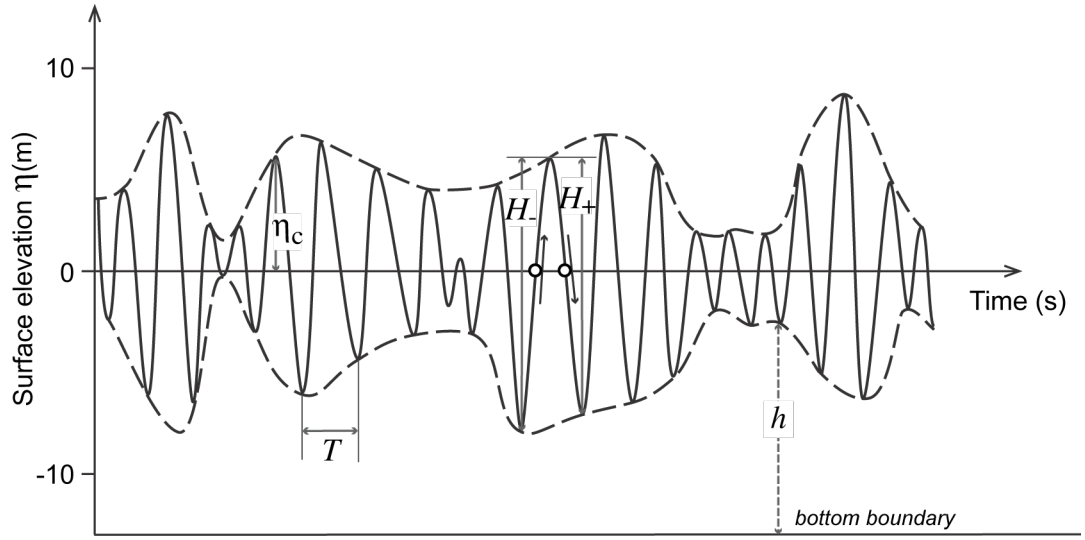

Figure 2.2: Illustration of ocean surface wave characteristics (extracted from a small portion of Draupner wave plotted in Fig. 2.1). The surface elevation η is the elevation of water surface above or below the reference level (average level); η_c is the height of the crest (the point of maximum elevation); H is the wave height, defined either as the distance from the crest to the trough (down-crossing) H_-, or the distance from the trough to the crest (up-crossing) H_+; T is the average wave period and h is the water depth.

wave trough to the wave crest (up-crossing), or from the wave crest to the wave trough (down-crossing), as illustrated in Fig. 2.2. For linear waves with narrow-banded spectrum, the crests and troughs are symmetric and lie practically on the envelope, thus the wave height H can be assumed to be twice the crest height η_c ($H \simeq 2\eta_c$). In this case, the probability distribution of crest height and wave height of the random Gaussian wave are closely related to the one of the envelope, i.e. the Rayleigh distribution.

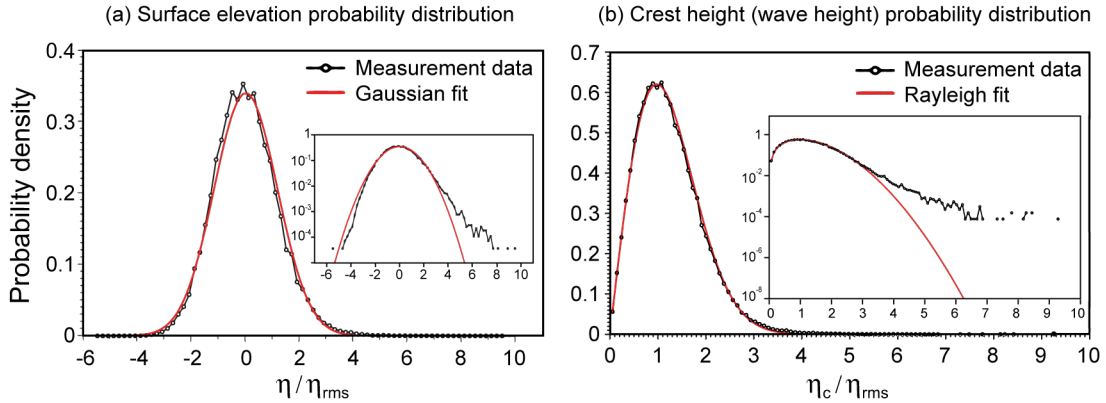

Figure 2.3: Probability density function of measurement data recorded from the Sea of Japan [2] (black), fitted with the predicted distributions. (a) Surface elevation data and a Gaussian fit. (b) Wave height data and a Rayleigh fit. Both functions are plotted on linear and logarithmic scales (inset). Both distributions are normalised to the root-mean-square surface elevation η_{rms}. *Source:* from Ref. [3].

Following this pioneer work of Longuet-Higgins, different types of modified distributions have been proposed and compared with the measurement data. Specifically, although these statistics were found to agree well with some field observations [66, 67], some recent field measurements show

that extreme wave amplitudes have much higher probability than those predicted [2, 3, 67–69] (see Fig. 2.3), indicating that the linear Longuet-Higgins theory is too simplistic and a more realistic theory is needed. In particular, the large-amplitude steep waves nature of rogue waves suggests the important role of nonlinearity. It was numerically and theoretically shown in Refs. [70] and [71] that if the ratio between the wave steepness (the ratio of the wave height to the wavelength) and the spectral bandwidth, called the Benjamin-Feir index (to be explained in the following section) is large, a departure from the Rayleigh distribution is observed.

It is important to note, however, that the Rayleigh distribution has also sometimes been found to overpredict the observed wave height [72, 73]. Some explanations have been proposed in order to explain this observation for example in Ref. [74, 75]. More details of the ocean wave statistics can be found in Ref. [14, 17, 20, 76].

Optical waves

The measurable quantity in optics is the intensity of light. The association of rogue waves with the deviation of field amplitude statistics from Gaussiannity, therefore, often translates into the deviation of intensity probability distribution from an exponential statistics [20, 77–79]. Indeed, the first link between extreme events in nonlinear optics to the one in the ocean is partly due to the experimental observation of 'L-shaped' long-tailed distributions, which signifies the non-negligable probability of the extreme events [26]. Following this work, several studies of rogue waves in different optical systems have been done, displaying various types of distributions depending on the system under study [20]. In some works, rogue events are associated with particular extreme-value probability distributions, such as Weibull [80–83], Pareto [80, 83], Log-normal [57], or stretched-exponential distribution [5, 33, 77, 84]. Fig. 2.4 contrasts the long tail property of these distributions to an exponential distribution.

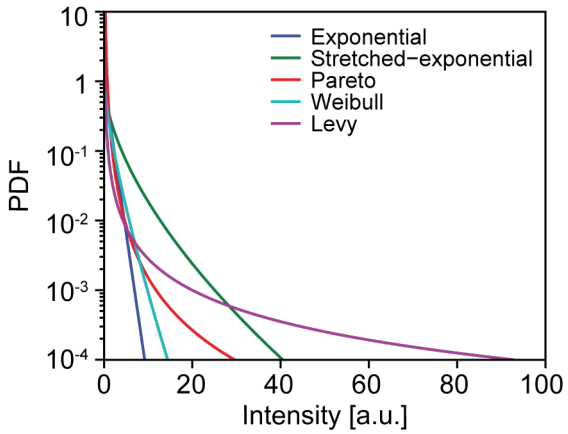

Figure 2.4: Examples of heavy-tailed distributions commonly reported in the study of optical rogue waves, compared to an exponential distribution.

In other cases, however, a particular probability distribution might not be identified due to the complexity of the system, or the statistical approach taken. Therefore, in general, optical rogue wave phenomena are linked with a class *long-tailed distribution* (for example in Ref. [32, 85–89]) or *heavy-tailed distribution* (for example in Ref. [28, 57, 78, 81–83, 90–93]). Although sometimes

used interchangably, it is important to note that these distributions do not actually have the same signification. Heavy-tailed is defined as distributions with heavier-than-exponential tails [12]. It is a general term referring to probability distribution function that descends slower than exponential function, which signifies a more probable realisation of extreme values than in a normal distribution. Whilst long-tailed is defined as distributions whose tails are asymptotically self-similar under shifting by a constant, and is a subclass of heavy-tailed distribution [94].

2.2.2 Classification of extreme events as rogue waves

Different simplified criteria in defining oceanic rogue waves have been proposed in the literature. A pragmatic approach is to call a wave a rogue wave whenever the wave height H or the crest height η_c exceeds a certain threshold related to the sea state, called the significant wave height (SWH) H_{S}. In the literature, SWH is commonly defined either as the average of the largest one third of wave heights $H_{1/3}$ [56], or as four times the standard deviation of the surface elevation. In general $H_{1/3}$ turns to be approximately 4σ, although it has been shown that the results could be different ($H_{1/3}$ is typically $5\% - 10\%$ lower than the value of 4σ) [73, 95]. Since standard deviation is the fundamental quantity used in oceanography, the definition of SWH as 4σ is preferred instead of the original definition in most of recent studies of oceanic rogue waves [14, 17, 20]. Subsequently, following one of these definitions, a rogue wave is defined commonly as a wave with wave height $H > 2H_{\mathrm{S}}$ and/or crest height $\eta_c > 1.25H_{\mathrm{S}}$, or both [96]. These simplistic criteria have been argued however, to be not sufficient as they do not take into account the nature (state) of the sea in which the waves occur [97].

Apart from the rogue threshold criteria, the kurtosis (fourth order statistical moment) of the distribution has also been suggested to be a suitable parameter for the identification of rogue waves in a short-term wave record [98–100]. Indeed, kurtosis is a parameter that measures the heaviness of the tail of the distribution [101], which is related to the probability of rogue wave occurrence.

Similarly, rogue waves in optics have also been identified in a number of different ways. One approach is to associate rogue events with particular extreme-value probability distributions, where such functions have been shown to provide good fits to the tails of optical intensity fluctuation histograms [30, 80, 81]. Another approach adapts one of the oceanographic definition of a rogue wave, where rogue wave height is defined as $H_{\mathrm{RW}} \gtrsim 2H_{1/3}$. The accessible data in optics however, is not the field amplitude but rather the intensity, and such data can take a variety of forms: an intensity time series, the levels of a two-dimensional camera image, or the space–time intensity evolution of an optical field. The oceanographic definition of rogue waves is therefore often modified to define a threshold $I_{\mathrm{RW}} \gtrsim 2I_{1/3}$, where the 'significant intensity' $I_{1/3}$ is the mean intensity of the highest third of events. This definition, although somewhat arbitrary, has been applied in several studies [83, 86, 102, 103].

2.3 Oceanic rogue waves

In recent years, considerable interest in understanding the origin of oceanic rogue waves has led to the development of various physical models to explain their generating mechanisms. Apart from its practical significance to engineers and naval architects, the study of the origin of oceanic rogue

waves is also useful as guidance in setting up different kind of laboratory experiments in related studies. In this section we review the generation of oceanic rogue waves from linear and nonlinear effects, where we focus only on the generation of oceanic rogue waves in the deep water (open sea).

2.3.1 Linear mechanisms

A random sea can be regarded as the result of wave superposition of an infinite number of small amplitude linear waves with different wave amplitudes and frequencies traveling in different directions

$$\eta(\mathbf{x}, t) = \sum_k a(\mathbf{k}) \cos(\mathbf{k}.\mathbf{x} - \omega t + \alpha(\mathbf{k})), \tag{2.1}$$

where η is the elevation, $\mathbf{x}$ is a position vector, and t is the time. The wave number $k = |\mathbf{k}|$ and the frequency ω satisfy the dispersion relation

$$\omega^2 = gk \tanh(hk), \tag{2.2}$$

where g is the gravitational acceleration and h is the water depth. The amplitude a and phase α are random variables, uncorrelated for each $\mathbf{k}$.

In the deep water regime, $h \gg \lambda$, $\tanh(kh) \sim 1$, and the dispersion relation can be written as

$$\omega = \sqrt{gk}. \tag{2.3}$$

Since the relationship between ω and k is not linear, this implies that deep water waves are dispersive, with phase velocity v_{ph}

$$v_{ph} = \frac{\omega}{k} = \sqrt{\frac{g}{k}} = \frac{g}{\omega} \tag{2.4}$$

and group velocity v_{gr}

$$v_{gr} = \frac{\mathrm{d}\omega}{\mathrm{d}k} = \frac{1}{2}\sqrt{\frac{g}{k}} = \frac{g}{2\omega} = \frac{v_{ph}}{2}. \tag{2.5}$$

From here we can see that both the phase velocity and the group velocity are dependent on the frequency (wavelength), where longer waves travel faster.

Spatial / geometrical focussing (spatial caustics)

Geometrical focussing is a well known local amplification process for waves of any physical nature and is related to spatial variation of wave fronts. In the simplest case, a wave front with cylindrical curvature is known to focus into one point. When the curvature of the wave front is complex, however, the focussing may result in spatially distributed focussing areas known as caustics. These caustics can then be considered as rogue waves when the condition described in Section 2.2 is fulfilled.

The curvature of wave front can be modified by the variation of water depth h, as described by the dispersion relation shown in Eq. 2.2. However, this situation is only relevant in the formation of rogue waves in shallow water (coastal zone). In deep water, geometrical focussing can result

from inhomogeneous wind flow (also known as "crossing sea", see Fig. 2.5(a)) and atmospheric pressure in storm areas, or from the wave interaction with variable currents [13, 14, 16]. Indeed, rogue waves have been observed very often in strong currents, for example in the Agulhas current that passes along the South African coast, suggesting that giant waves are produced by refraction of waves into a caustic region [104–106].

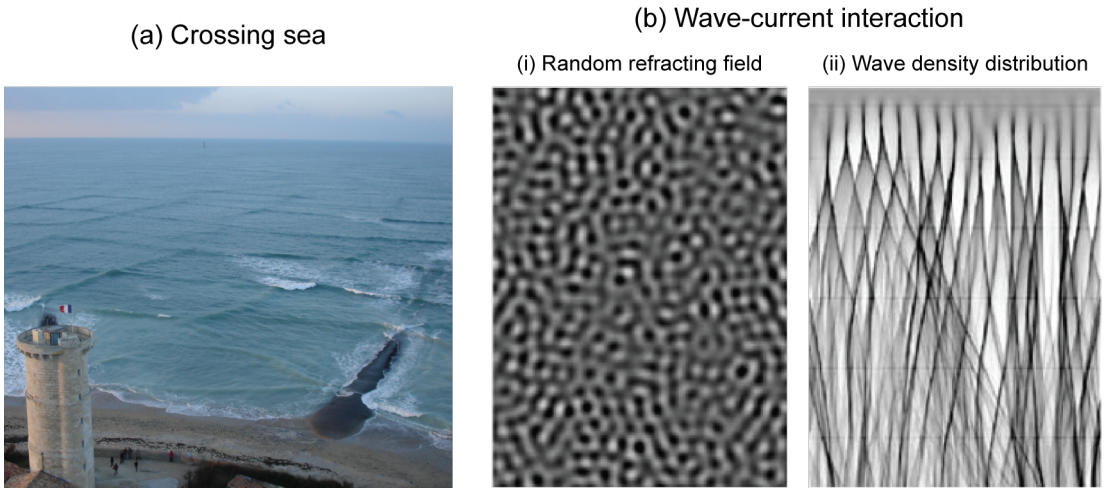

Figure 2.5: (a) Crossing sea, superposition of two wave systems travelling at different directions. (b) Study of wave energy density in a random refracting field for an initial set of parallel rays corresponding to a single plane wave: (i) The random velocity field acting as random refracting medium (darker shades indicate higher velocity); (ii) The focussing of uniform plane wave passing through the random refracting medium from top to bottom (darker areas correspond to higher energy density). *Source:* from Ref. [4].

Furthermore, it is also pointed out that even small random current fluctuations can result in focussing provided their scale is sufficiently large (on the order of 10 km), as shown in Fig. 2.5(b) [4, 62, 107]. Consequently, the sensitivity of caustics to the small variation of the initial conditions, results in the appearance and disappearance of the focuses at "random" points and "random" times, explaining the rare and short-lived character of the rogue wave phenomenon [13]. Additionally, under hypotheses that the mean current is constant and the random current fluctuations are small, the probability distribution for the formation of the freak waves is shown to be dependent only on the distance scale parameter, independent of the details of the current distribution [62].

Spatio-temporal focussing (dispersive focussing / space-time caustics)

The effect of geometrical focussing in deep water is significant, but the effect of temporal focussing also needs to be taken into account [16]. As we have seen earlier, deep water waves are dispersive with phase and group velocities inversely proportional to the frequency (Eq. 2.4 and 2.5), and may travel along different directions. Consequently, the locations of caustics are frequency-dependent and rogue waves are formed from space-time caustics [108]. Rare extreme wave events can therefore be interpreted as the local intercrossing of a large number of monochromatic waves with appropriate phases and directions [13].

For unidirectional surface waves, it can be understood that when long waves overtake short waves due to dispersion, large-amplitude waves can appear at some fixed time owing to the superposition of all the waves located at the same place, and then the long waves will be in front

of the short waves, forming a short "life time" freak wave. The formation of space-time caustics has been demonstrated in water wave tanks [109]. The idea is to create a long wave group with a properly designed chirp (linearly decreasing frequency) such that it will contract at a given position (to a few wavelengths) as the effect of dispersion.

In two-dimensional space, space-time caustics are formed by the combination of both dispersion and spatial focussing. It has been proposed that although the exact time and location of the wave focussing events are unpredictable, the expected spatio-temporal structure of the wave field in the vicinity of such events is largely predictable [108]. When superimposed with a random-wave field, this dispersion focussing effect will then only be apparent when the amplitude of the chirped wave train is higher than the standard deviation of the surface elevation [14].

It is important to note that although the physical mechanisms that produce the contrived phase relations and chirped wave trains have not been confirmed [14], it is suggested that this rare circumstance can be generated for example by the increase of wind speed that yields the generation of short waves followed by longer waves [15].

2.3.2 Nonlinear mechanisms

Linear theory is based on the assumption that the wave components are harmonic and independent from each other. When the waves are too steep however, the linear wave theory is no longer valid and nonlinear contribution becomes significant. In contrast to the linear theory, nonlinear wave interaction facilitates the exchange of wave energy between different wave components. This implies that random wave background might act on propagating coherent waves (uniform waves), leading to instability of the amplitude modulation of the waves. The effect of nonlinearity in rogue wave formation is therefore actively studied, where it is often associated to the increase in rogue wave probability beyond the conventional linear (or quasi-linear) theories, corresponding to a longer tail in the distribution [20].

Weakly nonlinear waves and the NLSE

Weakly nonlinear theory has been widely suggested to explain the emergence of rogue waves [98]. In general, the degree of wave nonlinearity regardless of the water depth can be measured in terms of a dimensionless parameter known as the wave steepness $s = kH/2$, where k is the wave number of the carrier wave and H is the wave height. Typical intense ocean wave trains are characterised by the steepness $s \approx 0.07 - 0.1$. It is known that uniform waves over deep water will grow when the initial steepness is large and then break when reaching a steepness of $s \approx 0.4$ [13, 16, 110]. This phenomenon shows that even though the wave breaking is a strongly nonlinear process, its final effect is to keep the water wave dynamics in a statistically weak nonlinear regime, thus justifying the weakly nonlinear approach [20].

Several reduced mathematical models have been developed for the study of deep-water waves. Among them, the nonlinear Schrödinger equation (NLSE) is often preferred to describe the spontaneous formation of extreme waves "out of nowhere" due to its simplicity and its universality. The NLSE is generic to all conservative systems that are weakly nonlinear and dispersive [111, 112], which was first derived by Zakharov in 1968 [113].

Under assumption of quasi-monochromatic waves, a slowly varying envelope approximation can be made and the surface elevation up to first order of nonlinearity can be written as

$$\eta(x,t) = \frac{1}{2}\left[A(x,t)\exp\left[i(k_0 x - \omega_0 t)\right] + c.c\right],$$

where $A(x,t)$ is the complex wave envelope (slowly vaying function of x and t), k_0 and ω_0 are the wave number and frequency of the carrier wave, *c.c.* denotes the complex conjugate.

The complex envelope $A(x,t)$ obeys the nonlinear model of deep-water wave trains, which in the lowest order in wave steepness and spectral width can be written as

$$i\left(\frac{\partial A}{\partial t} + v_g\frac{\partial A}{\partial x}\right) - \frac{\omega_0}{8k_0^2}\frac{\partial^2 A}{\partial x^2} - \frac{1}{2}\omega_0 k_0^2|A|^2 A = 0, \tag{2.6}$$

where $v_g = \partial\omega/\partial k$ is the group velocity. The second term of this equation takes into account the dispersive behavior of the surface elevation, while the last one is the nonlinear term. This equation is also known as the *space* NLSE, describing the space/time dynamics of the complex envelope function $A(x,t)$ of a deep-wave train which propagates in the x direction as a function of time. This formulation of the NLSE is appropriate for the space series analysis of data whose behavior is approximated by $A(x,0)$, as obtained by remote sensing technology [114].

In comparison with experimental results in wave tank facilities, the NLSE is often written as an evolution equation in space rather than in time, called the *time* NLSE

$$i\left(\frac{\partial A}{\partial x} + \frac{1}{v_g}\frac{\partial A}{\partial t}\right) - \frac{k_0}{\omega_0^2}\frac{\partial^2 A}{\partial t^2} - k_0^3|A|^2 A = 0. \tag{2.7}$$

This equation is suitable for the time-series analysis of measured wave trains whose behavior is approximated by $A(0,t)$. Time series observations of ocean waves are typically obtained by in situ instrumentation located at a fix spatial position.

Subsequently, it can be shown that the *time* NLSE can be transformed into the *dimensionless time* NLSE

$$i\frac{\partial\psi}{\partial\xi} + \frac{1}{2}\frac{\partial^2\psi}{\partial\tau^2} + |\psi|^2\psi = 0. \tag{2.8}$$

This equation is obtained by normalizing and introducing characteristic scales for the relevant physical quantities. This equation can be further transformed into the fibre NLSE (discussed in section 2.4), which describes the evolution of short pulses propagating in fibre optical system. The derivation of the transformation between different forms of the NLSE can be found in Appendix A.1

It is important to note that although the one-dimensional NLSE is an idealisation for the real ocean wave propagation which is two-dimensional in nature, the model is widely studied due to the many advantages it provides. It reduces the mathematical complexities which is beneficial for both analytical and numerical studies, thus enabling us to concentrate on the physical mechanisms of the formation of rogue waves. Moreover, the equation is known to be integrable [115] and the analytical solutions can be useful in identifying rogue waves in random wave trains [116–118], as we shall see in Chapter 4.

This model is relevant in the study of rogue waves emerging in a unidirectional propagation of swells in the ocean. Rogue waves in the form of "walls of water" may for example be described within this framework (Fig. 2.1(b)). Significantly, it allows theoretical-experimental comparison of a unidirectional water wave propagation conducted in a wave tank [116, 119–121].

Modulation instability

Nonlinear wave interaction results in instability when the wave amplitude is high enough and the perturbation modulating the wave is sufficiently long (there are sufficiently many waves under the perturbation). In its simplest form, the instability causes an exponential growth of a weak periodic perturbation on a continuous wave (CW) background (carrier wave), as shown in Fig. 2.6 (top). This instability is called the modulation instability (MI).

This growth of perturbation can also be seen as a result of energy transfer from the carrier wave to the perturbation wave, as shown in the bottom part of Fig. 2.6. Here, the carrier is represented by the intense spectral peak at ω_0 and the perturbation is represented by the spectral "satellites" with frequency Ω. This nonlinear wave interaction is a four-wave interaction, where the waves at frequency $\omega_0 + \Omega$ and $\omega_0 - \Omega$ are created from the carrier waves at frequency ω_0 [122]. As we shall see, this energy exchange can take place under perturbation with frequency Ω within a certain range close to ω_0, and therefore it is also known as side-band instability or spectral instability.

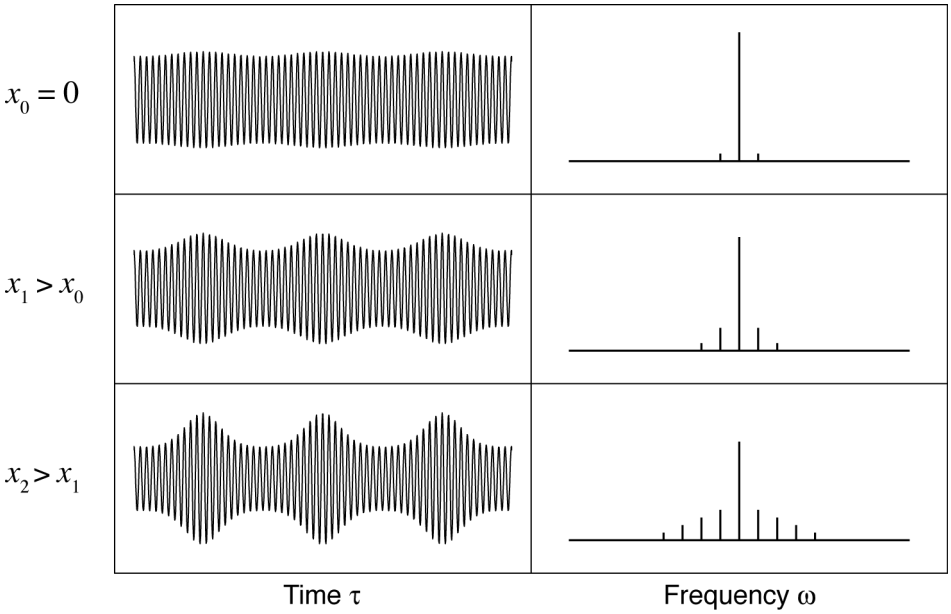

Figure 2.6: Modulation instability: amplification of a weak modulation imposed on a harmonic wave by nonlinearity, leading to the generation of spectral-sidebands through four-wave mixing process.

The phenomenon of modulation instability has been observed in different physical systems, including plasmas [123–125], laser light [126, 127], and in Bose-Einstein condensates [128]. This phenomena was discovered theoretically and experimentally in various studies conducted in the 1960s [122].

In the context of water wave, the study was pioneered by the works of Whitham, Lighthill, Benjamin and Feir, and Zakharov [113, 129–132]. However, this phenomenon is commonly called the Benjamin-Feir instability because they were the first in discovering the sideband nature of the instability [131]. They showed that this instability takes place if the criterion $kh > 1.363$ (k is the wave number of the underlying wave and h is the water depth) is fulfilled, which is in accordance with the discovery of Whitham showing that the nonlinear dispersive equation governing water wave is of elliptic type under this criterion [133]. Additionally, they also experimentally demonstrated the instability for the first time in a laboratory water tank [131, 132].

The condition leading to the instability in deep water wave trains can be derived by considering a small-amplitude modulated carrier wave of the form

$$\eta(x,t) = a_0\left[1+\epsilon\cos(Kx-\Omega t)\right]\cos\left[k_0x-\omega_0\left(1+\frac{1}{2}k_0^2a_0^2\right)t\right], \tag{2.9}$$

with a_0, k_0, and ω_0 being the amplitude, wave number, and frequency of the carrier wave; and ϵ, K, and Ω being the small modulation amplitude, modulation wave number, and modulation frequency [134]. It can be shown that by inserting this small-amplitude modulation to the *space* NLSE followed by linearization, one can obtain the *modulation dispersion relation*

$$\Omega^2 = \frac{\omega_0^2}{8k_0^2}\left(\frac{K^2}{8k_0^2}-k_0^2a_0^2\right)K^2, \tag{2.10}$$

which shows that the modulated wave train $\eta(x,t)$ can undergo exponential growth in the early evolution when the modulation wave number K lies in the range of $0 < K < K_\mathrm{c}$, with $K_\mathrm{c} = 2\sqrt{2}k_0^2a_0$ being the cut-off modulation wave number. The MI gain can be obtained from Eq. 2.10 by defining $g = \Im\{\Omega\}$, with maximum gain $g_\mathrm{max} = \frac{1}{2}\omega_0k_0^2a_0^2$ obtained at modulation wave number $K_\mathrm{max} = \pm K_\mathrm{c}/\sqrt{2} = \pm 2k_0^2a_0$. The gain curve is plotted in Fig. 2.7.

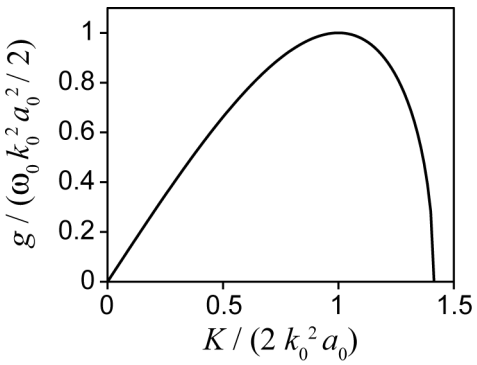

Figure 2.7: Modulation instability gain spectrum in hydrodynamics.

This instability condition is also often expressed by the so-called *Benjamin-Feir index (BFI)* I_{BF}

$$I_\mathrm{BF} = \frac{K_\mathrm{c}}{K} = \frac{2\sqrt{2}k_0^2a_0}{K} = \frac{2\sqrt{2}k_0a_0}{K/k_0} = \frac{\sqrt{2}k_0a_0}{\Omega/\omega_0}, \tag{2.11}$$

where it means that the waves under modulation are unstable for $I_\mathrm{BF} > 1$. The last equality results from the dispersion relation of deep water wave mentioned in Eq. 2.3.

The MI theory developed above is in the context of deterministic wave packets. The real ocean waves, however, is random and often characterised by a spectrum of limited bandwidth (describing the distribution of wave energy among different frequencies). The theory of MI for narrow-banded random wave was developed by Alber in 1978, where he demonstrated that instability can be suppressed significantly by wave randomness (characterised by the spectral bandwidth) [135]. In this context, the *BFI* can then be defined in terms of the ratio of the average steepness and the spectral width of the random waves

$$I_{\mathrm{BF}} = 2\frac{k_0 a_{\mathrm{rms}}}{\Delta k/k_0} = \frac{k_0 a_{\mathrm{rms}}}{\Delta\omega/\omega_0} = \frac{\text{steepness}}{\text{spectral width}}, \tag{2.12}$$

where a_{rms} is the root mean-square wave amplitude and $\Delta\omega/\omega_0$ is the relative spectral width of the wave ($\Delta\omega$ is estimated as the full width width at half maximum of the spectrum) [20, 98]. This implies that the *BFI* is essentially the ratio of nonlinear and dispersive effects, thus estimates the significance of the nonlinear wave interaction on the stochastic wave dynamics [15, 16].

The effect of randomness on the process of MI can also be understood by considering the ratio of the correlation length of the random waves to the modulation length. Considering the modulation is at the maximum MI gain and defining the correlation length of the random wave to be the inverse of the variance σ_r of the spectrum, this ratio can be written as

$$\frac{\text{correlation length}}{\text{modulation length}} \propto \frac{\sigma_r^{-1}}{K_{\mathrm{max}}^{-1}} \propto \frac{k_0 a_{\mathrm{rms}}}{\sigma_r/k_0}, \tag{2.13}$$

which is proportional with the BFI. The instability of random wave described by the criteria $BFI > 1$ can therefore be seen as the condition when the correlation length is longer than the length of the modulation [16]. As we shall see in Chapter 6, the effect of randomness on reducing the MI amplification is also observed in our optical system when MI is seeded by partially-coherent or incoherent seed.

The growth of perturbation from the modulation instability produces large waves and increases the population of rogue waves. Additionally, further focussing of these large waves can produce even larger waves with surface elevation η_{max} more than three times the initial average amplitude of the modulated waves. Further discussion on the relation between modulation instability and the statistics of rogue waves can be found in Chapter 4.

2.4 Optical rogue waves

Although most research on optical rogue waves has focussed on light propagation in optical fibres and in particular in regimes analogous to hydrodynamics, the terminology "optical rogue wave" has now been generalised to describe other noisy processes in optics with heavy-tailed probability distributions, irrespective of whether they are observed in systems with a possible oceanic analogy. Optical rogue waves have been seen for example as localised breathers in modulation instability (MI), in optical amplifiers, in instabilities in lasers, and high power pulse filamentation [6], as well as in speckle and other spatial patterns in cavities, multimode fibre, and photorefractive systems [5, 33, 77, 82, 136]. Detailed review and classification of various optical rogue wave study can be found in Ref. [20] and [6], which are summarised in Table 2.1.

Modulation Instability (NLSE)	Supercontinuum Generation and Solitons	Dissipative Systems	Spatial Instabilities	Linear Systems
Generation of Soliton on Finite Background (SFB) solutions [137–140] Stimulated MI [141] Spontaneous MI [142–144]	Continuous pumped SC [145, 146] Picosecond pulse SC [26, 30, 31] Femtosecond pulse SC [147]	Raman amplifiers [148] Parametric amplifiers [90, 149] Lasers (mode-locked lasers [86, 150, 151], CW Raman fibre laser [152], passively Q-switched lasers [87])	Nonlinear cavity [77] Single (femtosecond) filamentation [80, 136] Multi filamentation [82, 153] Photorefractive systems [33, 154]	Multimode optical fibre [5] Free space [32, 84, 155]

Table 2.1: Rogue waves in different optical systems

In this section, we aim to make a parallel comparison between the generating mechanisms of optical rogue wave and their hydrodynamic counterparts which is presented in section 2.3. For this purpose, only the mechanisms with direct insight into the formation of oceanic rogue waves are discussed, where they are classified into the linear or nonlinear effect in a similar way as presented earlier. The linear mechanisms are based on spatial focussing or spatio-temporal focussing, while the nonlinear mechanisms are based on the NLSE. This section is also constructed to provide some background to the discussions in the following chapters.

2.4.1 Linear mechanisms

Linear mechanism of optical rogue wave formation is similar to the oceanic counterpart discussed in Section 2.3.1. Localisation of waves is formed from linear superposition of waves of different frequencies travelling in different group velocity and directions.

In optics, the dependence of the velocity of light propagating in a medium to the frequency is described by the refractive index n. The phase velocity v_p of the light can therefore be written as

$$v_p = \frac{\omega}{k} = \frac{c}{n},$$

where ω and k are the frequency and the wave number of the light and c is the speed of light in the vacuum. It follows that the dispersion relation governing the propagation of light is then

$$\omega = \frac{ck}{n},$$

and the group velocity v_g is

$$v_g = \frac{\mathrm{d}\omega}{\mathrm{d}k} = \frac{c}{n} - \frac{ck}{n^2}\frac{\mathrm{d}n}{\mathrm{d}k} = v_p\left(1 - \frac{k}{n}\frac{\mathrm{d}n}{\mathrm{d}k}\right).$$

Indeed, this dependency of the group velocity to the wave frequency (through the refractive index) is known to be responsible for the broadening of optical pulses.

Spatial / geometrical focussing

Geometrical focussing mechanisms leading to deviations from Gaussian wave statistics in optics are often induced by spatial inhomogeneities imposed on the systems [20]. This linear mechanism of rogue wave formation has been studied in several recent optical experiments, conducted mainly in 2D spatially-extended systems, such as in multi-mode fibre or in free space (see Table 2.1). In general, the inhomogeneity imposed to the system is originated from intensity or waveform (phase) variation realised by an obstacle or a spatial light modulator (SLM), a device that spatially modulates a coherent beam of light. An arbitrary profile can be written into an SLM (see Chapter 3), which then modulates accordingly the spatial distribution of the light (the intensity, phase, polarisation state, or propagation direction) being refracted or reflected from it.

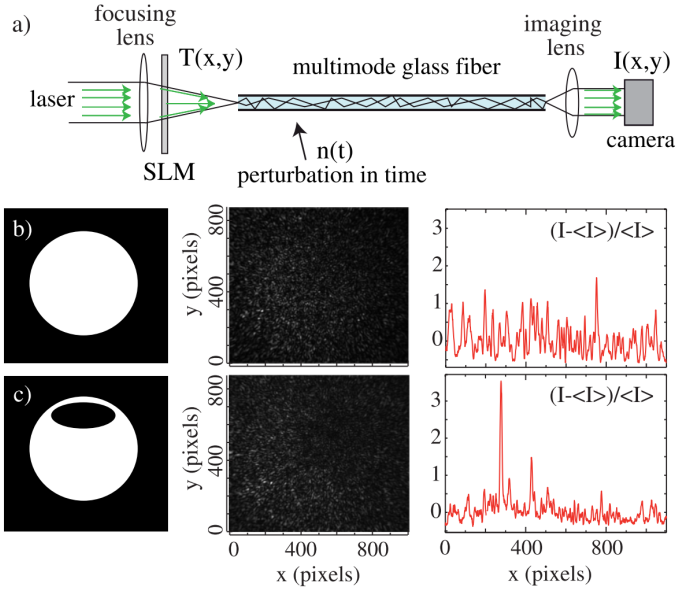

Figure 2.8: Linear rogue waves experiment. (a) Experimental set-up used to investigate rogue waves in the speckle pattern at the output of a multimode fibre. A spatial light modulator (SLM) is used to control the input beam profile. (b), (c) Measured speckle patterns (centre) and corresponding intensity distributions taken at a selected y-coordinate (right) when the SLM transmission mask (left) is uniform (b) and inhomogeneous (c). An optical rogue wave is observed in (c). *Source:* from Ref. [5].

In the experiment conducted by Arecchi *et al.*, optical rogue waves from geometrical focussing are observed in 2D chaotic wave fields at the output of a multimode fibre [5]. The setup is shown in Fig. 2.8(a). Laser beam of 532 nm wavelength is coupled into a multimode fibre, where the input intensity profile of the beam is controlled by an SLM. Two different masks are used, a uniform mask and an inhomogeneous mask (Fig. 2.8(b,c)). Intensity distributions at the output of the

fibre form speckle patterns as shown in the centre of the figure. Comparing the recorded speckle patterns from the two different masks, they show that rare high-intensity spots are observed when inhomogeneous mask is used, yielding a sub-exponential intensity distribution. A cross section of the intensity profiles are shown in the right side of the figure, where the optical rogue wave can be clearly distinguished.

In more recent experiments, optical rogue waves induced by inhomogeneity are shown in free space propagation systems [32, 84]. In one experiment, it has been shown that speckle patterns exhibiting non-Rayleigh statistics can be generated by redistribution of intensity among the speckle grains [32]. Specifically, heavy-tailed statistics of the intensity distribution are produced by generating high contrast speckle pattern (for example by squaring the field of a standard Rayleigh speckle). In another experiment, three-dimensional rogue waves in a speckle distribution of a spatially modulated optical beam are studied [84]. In this experiment, more rogue events are formed by blocking larger part of the beam (using a sharp blade), which also highlights the role of inhomogeneity in increasing the probability of extreme event generation [84].

It is important to mention that all of the experiments mentioned above study the focussing of speckle pattern. In this context, it is suggested that two main ingredients jointly play the role in the formation of optical rogue waves, namely the inhomogeneity and granularity [5, 156], where the latter signifies the fragmentation of the wave field in fundamental grains of activity (elementary objects of finite size) which in this case are the speckles. In this perspective, the inhomogeneity causes the clustering of the speckles forming stronger localisation.

In Chapter 3 we will see that granularity is not an absolute ingredient in the formation of rogue waves from linear mechanism. To this end, we conduct an experiment that compares rogue wave formation in a caustic network and in a (partially-developed) speckle pattern. In this system, the effect of inhomogeneity in caustic network formation and granularity in speckle formation is naturally separated [155]. Specifically, we show that intensity peaks satisfying statistical criteria for rogue waves are seen with higher probability in the case of the caustic network, highlighting the role of inhomogeneity as the main linear wave focussing mechanism in rogue wave formation.

Spatio-temporal focussing

In a uni-directional optical system, random appearance of high amplitude waves is routinely observed in optical communications in quasilinear regime (domination of dispersion over nonlinear effects) [157]. When short time slots are allocated for the transmitted symbols (in high-speed data communication), dispersion plays an important role causing short optical pulses to broaden and overlap with the neighbouring bits. This massive overlapping creates more randomness to the uncorrelated data streams and fluctuation of the signal power that greatly exceeds the average power. These high-intensity fluctuations occur in a reasonable time period due to the large number of realisations, and therefore can cause damaging in the signal transmission. However, the probability of occurrence of these high-intensity fluctuations is not higher than those described by a Gaussian distribution, and therefore, depending on the definition used, can be called rogue waves (as presented in Ref. [157–159]) or not (as argued in Ref. [160]).

In a two-dimensional optical system, spatio-temporal focussing yields an ultrafast subwavelength localisation of light, as shown recently in a photonic crystal resonator integrated

on a chip [35]. In this experiment, a particular shape of resonator which allows the generation of strongly incoherent waves is used. Statistical analysis of this fully random field is shown to follow a Rayleigh law, confirming the predicted statistics for the limit of an infinite number of interfering waves, and therefore is called "photonic sea". Significantly, it is shown that spontaneous synchronization of these incoherent waves can be triggered by suitably engineered losses, generating giant nanostructures of light, which results in a long-tailed distribution.

2.4.2 Nonlinear mechanisms

The analogous nonlinear mechanism of rogue wave formation between optical and ocean waves has its origin in the validity of the NLSE in governing nonlinear wave propagation in both systems [113, 161]. In optics, dispersion and nonlinearity are experienced by an intense, short pulse propagating in an optical fibre. Understanding of the nonlinear wave propagation in fibre optics therefore is crucial, and will be briefly summarized in this section. For more details on this topic, readers are referred to Ref. [162].

The propagation of optical fields in fibres, as for all electromagnetic phenomena, is governed by Maxwell's equations. It can be shown that these equations can be used to obtain the wave equation that describes light propagation in optical fibres (homogeneous, source-free medium)

$$\nabla^2\mathbf{E} = -\frac{1}{c^2}\frac{\partial^2\mathbf{E}}{\partial t^2} - \mu_0\frac{\partial^2\mathbf{P}}{\partial t^2},$$

where $\mathbf{P}$ is the induced electric polarisation, $c = 1/\sqrt{\mu_0\epsilon_0}$ is the speed of light in vacuum, μ_0 is the vacumm permeability, and ϵ_0 is the vacuum permittivity.

In optical fibres, as in any dielectric, the response of the material to intense electromagnetic fields becomes nonlinear due to the anharmonic motion of bound electrons under the influence of the applied field. Considering the material response is local and time invariant, the total polarisation $\mathbf{P}$ can be approximated using a series expansion [162, 163]

$$\mathbf{P}(\mathbf{r},t) = \mathbf{P}^{(0)}(\mathbf{r},t) + \mathbf{P}^{(1)}(\mathbf{r},t) + \mathbf{P}^{(2)}(\mathbf{r},t) + \mathbf{P}^{(3)}(\mathbf{r},t) + \dots,$$

where the general term of this series can be expressed as

$$\mathbf{P}^{(i)}(\mathbf{r},t) = \epsilon_0 \int_{-\infty}^{t} dt_1 \dots \int_{-\infty}^{t} dt_i \times \chi^{(i)}(t-t_1,\dots,t-t_i) \mid \mathbf{E}(\mathbf{r},t_1)\dots\mathbf{E}(\mathbf{r},t_i),$$

where $\chi^{(i)}$ is the i-th order susceptibility that represents the material response for the electric field. The vertical line "|" represents the tensor multiplication of $\chi^{(i)}$ with electric fields $\mathbf{E}(\mathbf{r},t_1),\dots,\mathbf{E}(\mathbf{r},t_i)$. The linear susceptibility $\chi^{(1)}$ is the dominant contribution to the total polarisation $\mathbf{P}$, while the higher order susceptibility terms govern the nonlinear effects. For optical fibre, the second-order susceptibility $\chi^{(2)}$ vanishes due to the inversion symmetry property of the material SiO_2. Including only the third-order nonlinear effects governed by $\chi^{(3)}$, the induced polarisation can be written as

$$\mathbf{P}(\mathbf{r},t) = \mathbf{P_L}(\mathbf{r},t) + \mathbf{P_{NL}}(\mathbf{r},t),$$

where the linear part $\mathbf{P_L}$ and the nonlinear part $\mathbf{P_{NL}}$ are related to the electric field by the relations [162, 163]

$$\mathbf{P_L}(\mathbf{r},t) = \epsilon_0 \int_{-\infty}^{t} \chi^{(1)}(t-t') \mid \mathbf{E}(\mathbf{r},t')dt' \tag{2.14}$$

$$\mathbf{P_{NL}}(\mathbf{r},t) = \epsilon_0 \int_{-\infty}^{t} dt_1 \int_{-\infty}^{t} dt_2 \int_{-\infty}^{t} dt_3 \times \chi^{(3)}(t-t_1, t-t_2, t-t_3) \mid \mathbf{E}(\mathbf{r},t_1)\mathbf{E}(\mathbf{r},t_2)\mathbf{E}(\mathbf{r},t_3) \tag{2.15}$$

Under assumption of instantaneous response of the material (neglecting the contribution of molecular vibrations to $\chi^{(3)}$), the linear and nonlinear part of the induced polarisation can be reduced to

$$\mathbf{P_L}(\mathbf{r},t) = \epsilon_0 \chi^{(1)} \cdot \mathbf{E}(\mathbf{r},t) \tag{2.16}$$

$$\mathbf{P_{NL}}(\mathbf{r},t) = \epsilon_0 \chi^{(3)} \vdots \mathbf{E}(\mathbf{r},t)\mathbf{E}(\mathbf{r},t)\mathbf{E}(\mathbf{r},t). \tag{2.17}$$

Weakly nonlinear waves and the NLSE

Since the nonlinear effects in silica fibres are relatively weak, the nonlinear polarisation $\mathbf{P_{NL}}$ can be treated as a small perturbation to $\mathbf{P_L}$. Assuming that the polarisation of the optical field (the orientation of the electric field) is maintained along the propagation (chosen to coincide with the x axis) and the optical field is quasi-monochromatic (the spectral width $\Delta\omega$ is much smaller than the center frequency ω_0), a slowly varying envelope approximation can be made and the electric field can be written as

$$\mathbf{E}(\mathbf{r},t) = \frac{1}{2}\hat{x}\left[F(x,y)A(z,t)\exp\left[i(\beta_0 z - \omega_0 t)\right] + \text{c.c.}\right], \tag{2.18}$$

where $\hat{x}$ is the polarisation unit vector, $F(x,y)$ is the modal distribution, and$A(z,t)$ is the slowly varying pulse envelope. β_0 is the wave number obtained from the dispersion relation of the material in terms of the propagation constant $\beta(\omega)$, which can be expressed by using a Taylor series around the carrier frequency ω_0

$$\beta(\omega) = n(\omega)\frac{\omega}{c} = \beta_0 + (\omega-\omega_0)\beta_1 + \frac{1}{2}(\omega-\omega_0)^2\beta_2 + \frac{1}{6}(\omega-\omega_0)^3\beta_3 + \cdots, \tag{2.19}$$

with

$$\beta_m = \left(\frac{d^m\beta}{d\omega^m}\right)_{\omega=\omega_0} \qquad (m = 0,1,2,\ldots).$$

Parameter β_1 is related to the group velocity n_g through $\beta_1 = c/n_g$, while β_2 represents the dispersion of the group velocity, known as the *group velocity dispersion* (GVD).

For a single mode fibre, $F(x,y)$ corresponds to the modal distribution of the fundamental fibre mode, which in practice is often approximated by a Gaussian distribution. Assuming this modal distribution does not vary much over the pulse bandwidth, and assuming there is no loss, the equation for the pulse evolution inside a single-mode fibre can be expressed by the evolution of the slowly varying pulse envelope

$$\left(\frac{\partial A}{\partial z} + \beta_1\frac{\partial A}{\partial t}\right) + i\frac{\beta_2}{2}\frac{\partial^2 A}{\partial t^2} - i\gamma(\omega_0)|A|^2A = 0, \tag{2.20}$$

where γ is the fibre nonlinearity in units of $\mathrm{W}^{-1}\mathrm{m}^{-1}$.

Eq. 2.20 is known as the *time* NLSE of nonlinear fibre optics and it can equally be written in the *co-moving / retarded frame* (a frame of reference moving with the pulse at the group velocity v_g) as

$$i\frac{\partial A}{\partial z} - \frac{\beta_2}{2}\frac{\partial^2 A}{\partial T^2} + \gamma |A|^2 A = 0 \tag{2.21}$$

by defining

$$T = t - z/v_g \equiv t - \beta_1 z. \tag{2.22}$$

In a similar way to the hydrodynamic counterpart, it can be shown that Eq. 2.21 can also be transformed into the *dimensionless time* NLSE (Eq. 4.1)

$$i\frac{\partial \psi}{\partial \xi} + \frac{1}{2}\frac{\partial^2 \psi}{\partial \tau^2} + |\psi|^2 \psi = 0$$

by introducing dimensionless variables

$$\xi = \frac{z}{L_{\mathrm{NL}}}, \qquad \tau = \frac{T}{T_0}, \qquad \psi = \frac{A}{\sqrt{P_0}},$$

where $L_{\mathrm{NL}} = (\gamma P_0)^{-1}$, $T_0 = \sqrt{|\beta_2| L_{\mathrm{NL}}}$, and P_0 is the incident power (see Appendix A.1). The analytical solutions of this NLSE can be found in Chapter 4.

The NLSE is the simplest nonlinear equation taking into account the third-order nonlinear effects in optical fibre. In the case of ultrashort pulses, higher-order nonlinear effects (self-steepening, intrapulse Raman scattering) and third-order dispersion need also to be included, and the equation governing the pulse evolution is approximated by the so-called the generalised NLSE (the GNLSE)

$$\frac{\partial A}{\partial z} + \frac{\alpha}{2}A + \frac{i\beta_2}{2}\frac{\partial^2 A}{\partial T^2} - \frac{\beta_3}{6}\frac{\partial^3 A}{\partial T^3} = i\gamma\left(|A|^2 A + \frac{i}{\omega_0}\frac{\partial}{\partial T}(|A|^2 A) - T_R A\frac{\partial |A|^2}{\partial T}\right), \tag{2.23}$$

where α is the absorption coefficient (the loss) of the fibre. Note however, that the Raman term in this equation approximates a linear Raman response and can only accurately describe pulse propagation of < 5 THz (corresponding to a pulse width $T_0 > 60$ fs) [164]. However, the slowly varying envelope approximation is still applied here, which implies that the ultrashort pulses should still be wide enough ($T_0 > 100$ fs) in order to have many optical cycles underneath [162].

Comparing Eq. 2.21 and 2.23, we can see that the GNLSE can be reduced to the NLSE when the third-order dispersion term, the parameters $(\omega_0 T_0)^{-1}$ and T_R/T_0 are very small such that these terms can be neglected. This condition can be obtained when the pulse width $T_0 > 5$ ps and the carrier wavelength is far enough from the zero-dispersion wavelength.

Modulation instability

The theory of modulation instability (MI) in optics (electromagnetics) was developed around the same time as the one in hydrodynamics, where it was stimulated in particular by the rapid progress in studies of lasers and related problems of nonlinear optics [122]. The phenomenon of

MI on electromagnetic waves propagating in nonlinear dispersive medium (dielectric) was predicted for the first time by Ostrovskii in 1963 [165]. The theory was developed later in 1967, showing that the propagation of a plane wave in an isotropic weakly-nonlinear medium can be described by 1D coupled equations, and the wave is unstable under perturbations [166]. The first experimental realisation of these theoretical results was then conducted by Zagryadskaya and Ostrovskii in 1968, where propagation of an electromagetic wave in a transmission line containing nonlinear inductances of ferrite was shown to be unstable under modulation within certain range of frequency [167]. Following this work, a stronger effect in lines containing nonlinear capacitors of semiconductor diodes was later shown by Ostrovskii and Soustov[168].

It is important to mention that although the first prediction is made by Ostrovskii, the theory of MI of electromagnetic waves is first developed by Bespalov and Talanov in 1966 [126]. The context of the study, however, is on the formation of filamentation, where 2D beam propagation is considered and the MI observed is in the form of spatial instability. They showed that small irregularities in the beam profile of high intensity wave propagating in a nonlinear medium can rapidly increase along the propagation, which leads to the break-up of the beam into several hot spots (multiple filaments) due to the MI.

On the interest of light propagation in a single-mode optical fibre, the MI theory developed by Ostrovskii is of particular significance as the formulated 1D coupled equations can be shown (under certain conditions) to be equivalent to the NLSE shown in Eq. 2.6 [122]. In this context, the MI is proposed to be observed in the propagation of light at wavelength in the anomalous regime of the single-mode fibre by Hasegawa and Brinkman in 1980 [169]. The first experimental observation is reported by Tai *et al.* in 1986, where the MI side-bands of a quasi continuous wave (100 ps pulse width) are shown to grow from the noise. Additionally, the dependence of the modulation frequency upon the fibre parameters and the laser power is also studied [127].

The condition leading to instability in optical fibres can be derived by means of linear stability analysis. We start by considering the propagation of CW field in an optical fibre, where the amplitude of the wave envelope $A(z,T)$ is independent of T at the input of the fibre at $z = 0$. Assuming that it remains time independent along the propagation, the fibre NLSE shown in Eq. 2.21 can be solved to obtain the steady state solution

$$A = \sqrt{P_0}\exp(i\phi_{\mathrm{NL}}),$$

where P_0 is the incident power and $\phi_{\mathrm{NL}} = \gamma P_0 z$ is the nonlinear phase shift induced by self phase modulation (SPM).

If we consider a small perturbation $a(z,T)$ to the steady state in the form

$$A = (\sqrt{P_0} + a)\exp(i\phi_{\mathrm{NL}}), \tag{2.24}$$

and substituting this solution to the NLSE (Eq. 2.21) followed by linearization in a, we obtain

$$i\frac{\partial a}{\partial z} = \frac{\beta_2}{2}\frac{\partial^2 a}{\partial T^2} - \gamma P_0(a + a^*).$$

Solving this equation yields a solution of the form

$$a(z,T) = a_1 \exp\left[i\left(Kz - \Omega T\right)\right] + a_2 \exp\left[-i\left(Kz - \Omega T\right)\right], \tag{2.25}$$

where K and Ω are the wave number and the frequency of perturbation respectively. Note that the actual wave number and the frequency of the perturbation are $\beta_0 \pm K$ and $\omega_0 \pm \Omega$ because the factor $\exp\left[i(\beta_0 z - \omega_0 t)\right]$ has been factored out in Eq. 2.18.

It can then be shown that K and Ω satisfy the *modulation dispersion relation*

$$K = \pm\frac{1}{2}\left|\beta_2\Omega\right|\left[\Omega^2 + \mathrm{sgn}\left(\beta_2\right)\Omega_\mathrm{c}^2\right]^{1/2}$$

with $\mathrm{sgn}\left(\beta_2\right) = \pm 1$ depending on the sign of β_2 and $\Omega_\mathrm{c}^2 = 4\gamma P_0/|\beta_2|$. This shows that the perturbation $a(z,T)$ will grow exponentially with propagation distance z when $\beta_2 < 0$ and $|\Omega| < \Omega_\mathrm{c}$. In other words, a CW beam is inherently unstable when experiencing anomalous dispersion inside fibre, where it can undergo spontaneous temporal modulation and be transformed into a pulse train.

In addition, the MI gain can be obtained from Eq. 2.24 and 2.25 by defining $g = 2\Im\{K\}$, where the maximum gain $g_\mathrm{max} = 2\gamma P_0$ is at modulation frequency $\Omega_\mathrm{max} = \pm\Omega_\mathrm{c}/\sqrt{2} = \pm\sqrt{2\gamma P_0/|\beta_2|}$. The gain curve is plotted in Fig. 2.9.

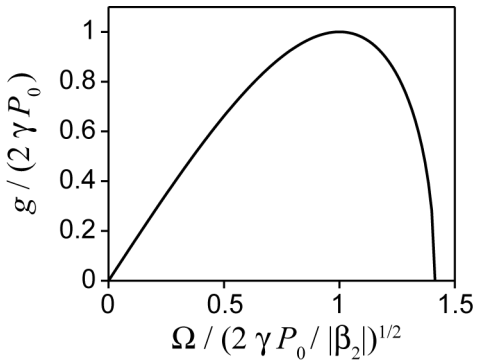

Figure 2.9: Modulation instability gain spectrum in optics.

The instability condition here can also be expressed by the *Benjamin-Feir Index (BFI)* I_BF defined as

$$I_\mathrm{BF} = \frac{\Omega_\mathrm{c}}{\Omega} = \frac{2\sqrt{\frac{\gamma P_0}{|\beta_2|}}}{\Omega} = \frac{\sqrt{\frac{2\gamma P_0}{\pi c|D|}}}{\Omega/\omega_0}, \tag{2.26}$$

where D is the dispersion parameter of the fibre which is related to β_2 through the relation $D = -\frac{2\pi c}{\lambda^2}\beta_2$. Similarly, the modulated waves are unstable when $I_\mathrm{BF} > 1$.

In the case of partially coherent optical wave, *BFI* can also be derived from the analogy with the ocean wave

$$I_\mathrm{BF} = \frac{\sqrt{\frac{2\gamma \bar{P}_0}{|\beta_2|}}}{\Delta\Omega} = \frac{\sqrt{\frac{\gamma \bar{P}_0}{\pi c|D|}}}{\Delta\Omega/\omega_0}, \tag{2.27}$$

where $\bar{P}_0$ is the average power of the propagating light [170]. This implies that the MI is suppressed when the bandwidth of the spectrum becomes comparable to the MI frequency $\Delta\Omega = \bar{\Omega}_\mathrm{max} =$

$\sqrt{2\gamma\bar{P}_0/|\beta_2|}$. This formalization of the *BFI* can be used to predict the possibility of a partially incoherent wave to undergo MI, as experimentally confirmed in Ref. [171].

2.5 Optical - oceanic rogue waves comparison

In this chapter, we have briefly reviewed the historical context of oceanic rogues waves and the beginning of scientific endeavor of rogue wave study. Motivated from the rogue wave phenomena observed in the ocean, the study of rogue waves has been expanded in many other physical systems, and especially in optics. Although analogy with oceanic rogue waves are found in some cases, other studies of rogue waves often cannot be compared meaningfully with the oceanic counter part. Furthermore, the terminology of rogue waves becomes hardly distinguishable from the general definition of extreme events. Therefore, although they have been observed in many physical systems, the strict definition of rogue waves can sometimes still be argued.

The definition of rogue waves in a random dynamical system cannot be separated from the statistics. In particular, we have discussed two main criteria commonly used in categorizing extreme events as rogue waves, i.e. the deviation of the statistics from Gaussiannity (as property of a fully random system) and the threshold above which the wave is classified to be rogue waves. Although, in general, rogue waves are defined in a system exhibiting a heavy-tailed distribution, this definition is not always strictly followed in recent studies. Instead, the threshold criteria is more commonly used to define rogue waves, i.e. $H_{\mathrm{RW}} > 2H_{\mathrm{S}}$ in oceanography and the adopted criteria $I_{\mathrm{RW}} > 2I_{\mathrm{S}}$ in optics.

Apart from the ambiguity on the definition of rogue waves, the physical mechanism causing their emergence is also still under investigation. We have seen that in general, these mechanisms can be categorised into linear or nonlinear mechanism. Specifically, we show that the same rogue wave generating mechanisms known in the ocean can also be found in optics. This similarity provides the possibilities of exploring oceanic rogue wave in convenient table-top optical experiments. The study of extreme events in optical systems can therefore be beneficial not just for its applications in optics but also to improve the general understanding of rogue waves.

Linear mechanism

Following the discussion in Section 2.3.1 and 2.4.1, we can see that rogue waves in the ocean and in optical systems can be generated in a purely linear regime through focussing processes. The linear focussing can in general be categorized into spatial (geometrical) focussing and spatio-temporal (dispersive) focussing, introduced by spatial or spatio-temporal inhomogeneity in the system.

Nonlinear mechanism

Many physical and natural systems exhibit nonlinear dispersive waves, including ocean and optical waves. We have shown that the propagation of ocean waves (under certain circumstances) and light in fibre optics are governed by the same equation, i.e. the NLSE (Fig. 2.10). This implies that although in this case rogue waves are still random events, their unexpected appearances are in fact a result of deterministic process, arising due to sensitivity to the initial conditions.

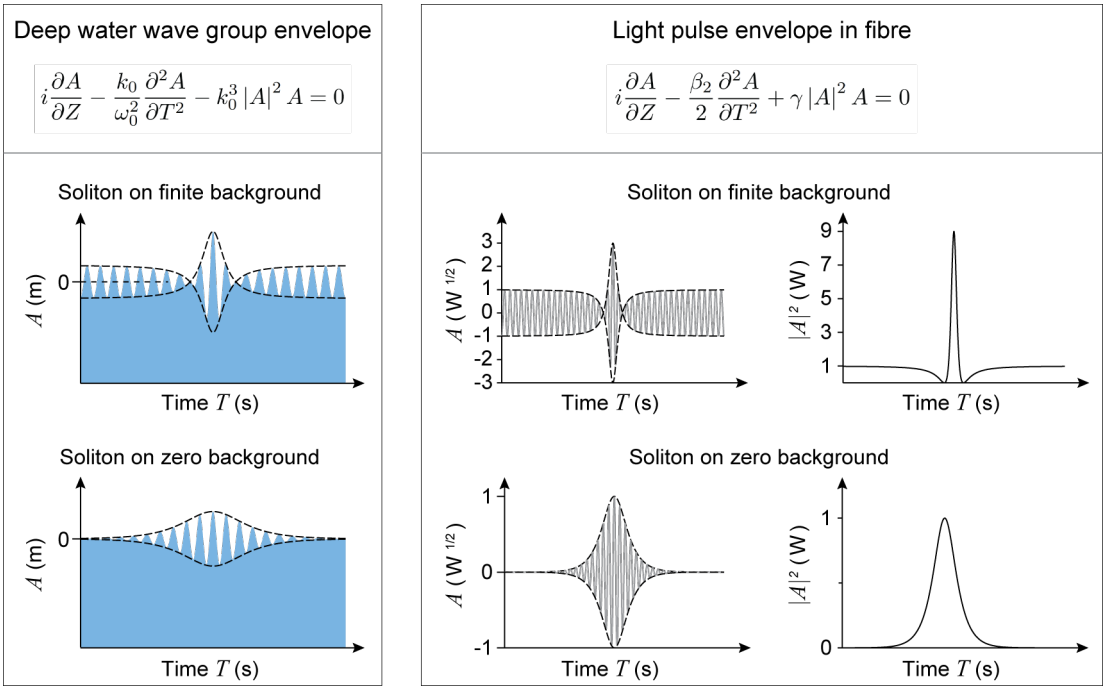

Figure 2.10: The NLSE describes wave evolution in different physical systems. (a) Wave group envelope u on deep water. (b) Light pulse envelope A in an optical fibre with anomalous group velocity dispersion. The figure illustrates solitons on finite background (top) and solitons on zero background (bottom). Note that for the ocean wave case, there is always deep water underneath $u(z,t)$. For the water wave NLSE, k_0 is the wave number and ω_0 is the carrier frequency; for the fibre NLSE, $\beta_2 < 0$ is the group velocity dispersion and γ is the nonlinear coefficient. *Source:* from Ref. [6].

Nonlinear dispersive systems governed by the NLSE are known to exhibit wave amplification process called the modulation instability (MI). As we have seen in section 2.3.2 and 2.4.2, this instability causes periodic perturbations on a continuous-wave background to grow exponentially along the propagation. For this reason, MI has been proposed to be the generating mechanism of rogue waves in various physical systems [71, 98, 122]. The study of MI within the framework of the NLSE and their relation with rogue waves is discussed further in Chapter 4.

Chapter 3

Rogue waves in a linear optical system

Although much attention has been paid to the role of nonlinearity in generating rogue waves [18, 144, 172–174], rogue wave behaviour in purely linear systems has also been reported in oceanography [13, 14, 17] and in electromagnetics (optical and microwave frequencies) [5, 25, 32, 84]. As discussed in the previous chapter (Section 2.3.1), linear mechanisms of oceanic rogue wave formation are in general linked to spatially or spatiotemporally wave focussing, which is also known as caustics [13, 14, 61, 62, 104–108, 175–177].

In optics, caustics are a well-known phenomenon, associated with distinct regions of high intensity field being formed from an envelope of light rays reflected or refracted by a curved surface [178, 179]. They are commonly observed when light shines on a drinking glass producing a curved region of bright light, or in the form of caustic networks formed on the floor of a swimming pool when light shines through the wavy water surface. Essentially, they are focus areas generated from wave front with random curvature, similar to a focus point generated from a wave front with cylindrical curvature. In spite of the abundance of observations, however, the link between the formation of caustics and rogue wave events in optical systems has not been studied in detail.

Motivated by the study of rogue wave formation by caustics in oceanography, we investigate in this chapter the link between caustic formation and rogue wave events in optical system. We perform a detailed study of rogue wave formation from the focussing of random coherent spatial field. Specifically, we investigate the occurrences of both two-dimensional and three-dimensional focussing, with a direct analogous to the rogue waves formation in the ocean for the two-dimensional case.

3.1 Experimental setup

The system we use is conceptually very simple, involving the application of random initial phase to a coherent optical field, followed by subsequent free space propagation. As shown schematically in Fig. 3.1(a), we first use a phase spatial light modulator (SLM) to modulate the phase of the incident

coherent laser beam (without any change of the intensity), and then we record the evolution of the modulated beam profile using an imaging system. We apply here different phase patterns (phase masks) to the SLM in order to study the formation of rogue waves from linear focussing effects.

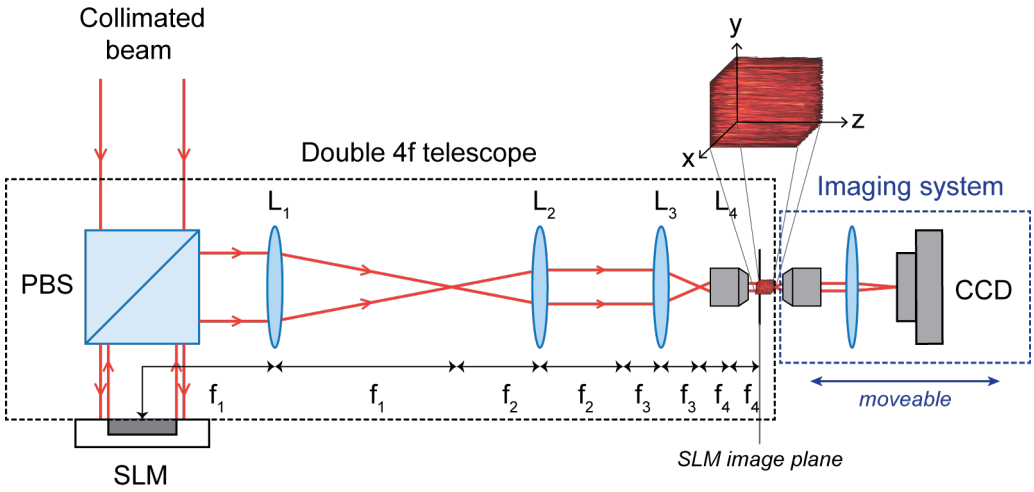

Figure 3.1: Experimental setup. An SLM encodes random spatial phase on a coherent beam from a He-Ne laser. Free space propagation transforms this random phase to random intensity spatial fluctuations. An imaging system is used to reduce the size of the beam so that it can be recorded on a CCD camera which can be translated longitudinally over an extended measurement volume. All measurement distances given in the text are relative to the origin $z = 0$ of the axes shown. Here $f_1 = 500$ mm, $f_2 = 250$ mm, $f_3 = 100$ mm, $f_4 = 9$ mm.

A coherent beam from a continuous wave laser (Helium Neon laser with $\lambda = 632.8$ nm) is expanded to fill the aperture of a Hamamatsu LCOS-SLM (liquid-crystal-on-silicon spatial light modulator), X-10468 series (see Fig. 3.1). The SLM is an electrically addressed reflection type phase SLM with 800×600 pixels array over dimensions of 16×12 mm. The refractive index (the optical path length) at each pixel in the SLM is varied by applying the electric field that controls the angle of rotation of the liquid crystal molecules inside the device, thus modulating the phase of the light being reflected from it. We use in our experiments a square random spatial phase pattern of 600×600 pixels with 256 grayscale levels. As we shall see in the next sections, the spatial phase patterns applied have either one-dimensional or two-dimensional randomness, where the phase variations are smoothed over typically 10 pixels so that one can consider the SLM as physically equivalent to a random continuous refracting surface.

Imaging systems are used to reduce the size of the beam after the SLM to the measurement region indicated in Fig. 3.1 and to fill the aperture of the detector. The first imaging system consisted of four lenses with $f_1 = 500$ mm, $f_2 = 250$ mm, $f_3 = 100$ mm, $f_4 = 9$ mm, yielding a demagnification of $\approx \times 22$. The transversal dimensions of the measurement region obtained were 0.54×0.54 mm. The pattern detection system used an IDS uEye UI-3240CP CCD camera with a 1280×1024 pixels array over dimensions 6.78×5.43 mm and with a 10 bit analog-to-digital converter (ADC). The second imaging system was then used to magnify the beam ($\approx \times 15$) to fill the CCD camera aperture. Translation of the CCD camera was possible over a 500 μm range from the input plane of the measurement zone using a Newport ILS-LM Series precision translation stage that was scanned in steps of 5 μm.

3.2 Two-dimensional focussing

The study of two-dimensional focussing can be realised by applying an SLM phase mask with random pattern varied only along one transverse direction (with identical pattern repeated in another transverse direction). This way, the coherent incoming light is refracted only along that specific phase modulated transverse direction and the beam evolution can be treated as two-dimensional propagation problem.

We show in this section that extreme intensity focussing (spatial caustics) can be formed along the propagation, even with relatively weak and smooth modulation of phase. We study the effect of the modulation strength and show that stronger modulation of phase can indeed form sharper caustics with higher peak intensities. This study can be linked to the caustic formation in water waves (see Section 2.3.1) due to the common equation governing the evolution of waves in both systems, i.e. the two-dimensional Helmholtz equation [180, 181].

Numerical simulation results modelling the experimental setup with one-dimensional variation of phase mask are shown in Fig. 3.2. The simulations discretised the incident field profile to match the experimental SLM pixellation, upon which a smoothed random phase function was applied. A truncated Gaussian fit to the experimental laser beam incident on the SLM was used as the input field. The Angular Spectrum of Plane Waves method [182] was then used to numerically propagate this beam through the optical system described above (see Appendix B.1).

We compare the evolution of light being refracted by two different spatial phase patterns with different modulation strength. Fig. 3.2(a)(i) plots a phase modulation of maximum $\varphi_{\max} = 2\pi$, while Fig. 3.2(b)(ii) plots a stronger phase modulation of maximum $\varphi_{\max} = 10\pi$. Different random patterns are used in these two cases in order to highlight the most pronounced extreme focussing for each case. Fig. 3.2(a,b)(ii) plot the unwrapped slices of the phase distributions along y-direction (the vertical axis in Fig. 3.2(a,b)(i)).

A direct obervation of the two-dimensional evolution of the refracted light plotted in Fig. 3.2(a,b)(iii) shows that some focussings yield significantly higher intensity than others. Their intensity contrast is highlighted in Fig. 3.2(a,b)(iv-vi), comparing the intensity distribution of the field evolution before, during, and after the extreme focussings. For phase modulation with $\varphi_{\max} = 2\pi$ (Fig. 3.2(a)), the intensity of the rogue peak is 7.5 (normalised relative to the maximum intensity of the input Gaussian beam incident on the SLM), which is ≈ 4.4 times the average peak intensity calculated to be 1.7. While for phase modulation with $\varphi_{\max} = 10\pi$ (Fig. 3.2(b)), the intensity of the rogue peak is 14.3, which is ≈ 5.7 times the average peak intensity calculated to be 2.5. This comparison shows that stronger phase modulation (for a given average transverse size of phase variation) leads to stronger focussing with narrower and higher intensity of localised peaks.

In the relation to the focussing mechanism of water waves, these results can be linked to the suggested generating mechanism of oceanic rogue waves, as for example from wave-current interaction. As discussed in Section 2.3.1, strong currents in the ocean can act as random refracting fields of the incoming waves. Since the random phase variation of SLM mask used here acts as a random refracting field and the equation governing the propagation of waves in both systems are the same, the phase modulation in this setup can be meaningfully linked to the random current acting on water waves, showing that stronger random currents yield larger amplitude waves.

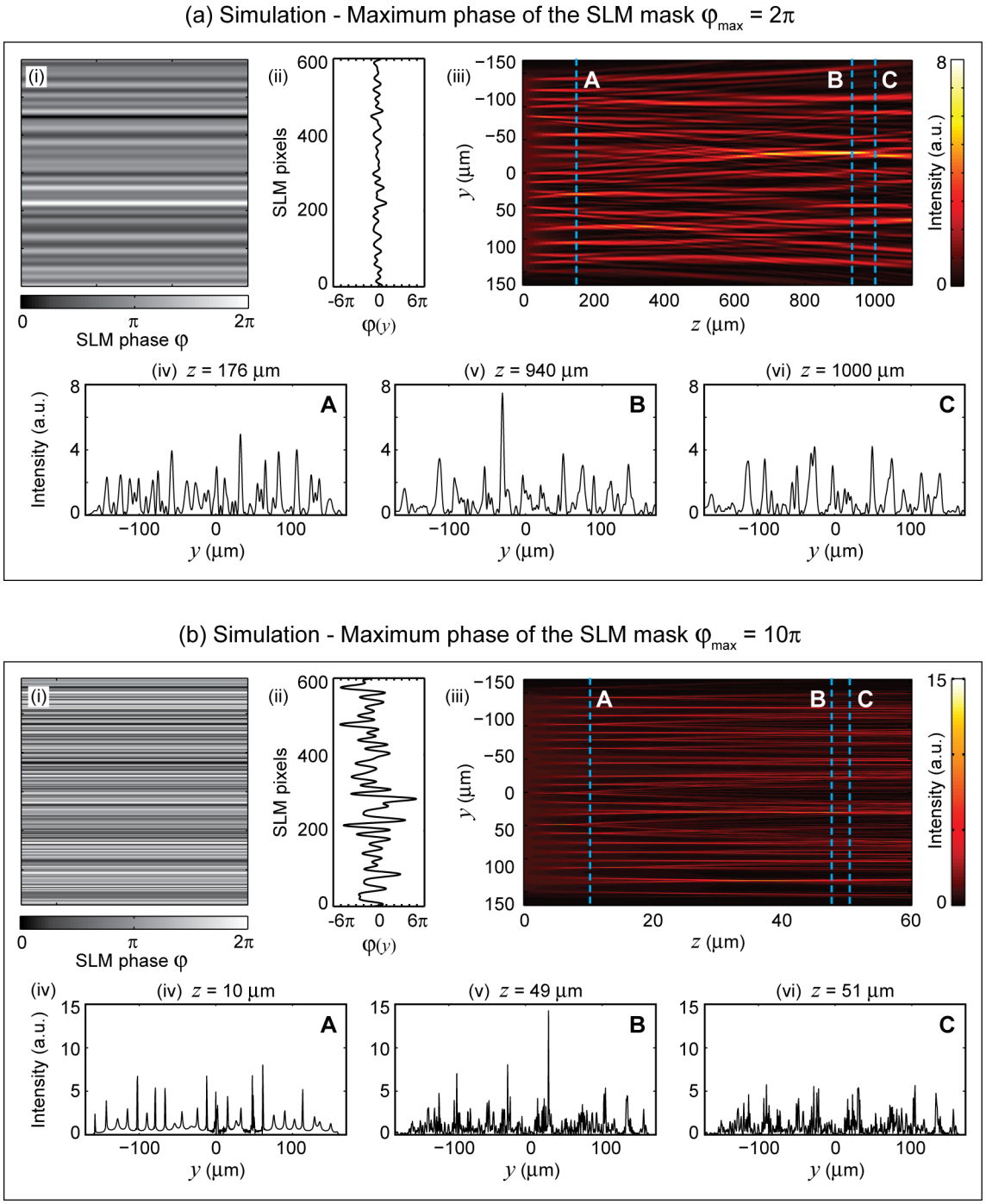

Figure 3.2: Numerical simulations of one-dimensionally phase modulated beam with (a) weak phase modulation of 2π and (b) strong phase modulation of 10π. For each case, (i) shows the applied phase distribution to the SLM; (ii) shows the unwrapped slice of the applied phase distribution along y-direction; (iii) shows the two-dimensional evolution of the refracted light observed in yz-plane; (iv-vi) shows the slice of the intensity distribution at different location along z, highlighting the contrast of the intensity distribution before, during, and after an extreme focussing. The intensity here is normalised to the intensity of incident beam.

It is important to notice however, that although the nature of these results is similar to the studies reported in Ref. [62, 107, 183] (see Fig. 2.5 in Chapter 2), the refraction of the incoming waves simulated here occurs only at a specific position $z = 0$, while the waves entering a zone of currents undergo a continuous refraction due to the wave-current interaction along the propagation. This observation therefore shows that even short interaction of plane waves with random refracting field can already lead to significant focussing along the propagation.

3.3 Three-dimensional focussing

We investigate in this section the focussing of light in three-dimensional space, where refraction and reflection of light by refractive-index inhomogeneities is known to produce caustic network [178]. At the same time, the propagation of continuous-wave laser light being reflected from rough surfaces or transmitted through diffusers are known to exhibit fine scale fluctuations of intensity in space, which is known as "speckle" [182]. In this context, it has been shown that a coherent field with random phase will initially evolve into a regime of caustic focussing before developing progressively into a granular speckle pattern with propagation distance [184].

The precise nature of the evolution and the structure of these observed patterns depend in detail on the magnitude of the random phase variation. It determines the random focussing of different portions of the beam at any particular distance. In particular, it has been shown that a partially-developed speckle pattern (instead of a fully-developed speckle pattern) is formed when light is scattered from a random refracting field with small roughness [185–187]. Indeed, a high contrast speckle can only be formed when the surface roughness allows for a difference typical phase deviation of $> \pi$ (i.e. typical path difference of $> \lambda/2$), commonly expressed by the standard deviation of the phase $\sigma_\varphi > \pi/2$ [187–189], such that a complete destructive interference can be observed at some points in the speckle pattern. When this condition is not satisfied, the specular field component of the light I_0 does not extinct and is superposed with the diffuse field component (the component responsible for the formation of speckle pattern) I_d, yielding a low contrast speckle with a total mean intensity $\langle I \rangle = I_0 + \langle I_d \rangle$ being formed. In this case, the speckle contrast, defined as

$$\rho = \sigma_I / \langle I \rangle \tag{3.1}$$

is then less than 1, where σ_I is the standard deviation of the speckle intensity variation.

In this section, we highlight the difference in form and statistics between partially-developed speckle and caustic structures, generated respectively by weak and strong scatterers. Using the setup shown in Fig. 3.1, we perform simulations and experiments of coherent light propagation being refracted by two-dimensional random surface and follow the three-dimensional evolution of the beam profile.

3.3.1 Numerical modeling

We use the same numerical simulations as explained in the previous section to model the propagation of light through the experimental setup shown in Fig. 3.1. Similarly as before, random phase variation of 2π and 10π are used here to simulate weak and strong

two-dimensional random refracting surface. Fig. 3.3(a,b)(i) show the applied phase distributions to the SLM, while Fig. 3.3(a,b)(ii) show the unwrapped slices of the phase distributions along y-direction (the vertical axis in Fig. 3.3(a,b)(i)).

The subsequent propagation of the phase modulated beam results in the development of random intensity maxima and minima in the spatial beam profile, starting from the formation of caustic network then followed by the well-known physics of the development of optical speckle [182, 184, 190]. The different nature between the structures of caustic network (Fig. 3.5(a)(i,ii)) and speckle patterns (Fig. 3.5(b)(i,ii)) implies the difference in their intensity distribution. In the case of caustic network, connected "web" of light is formed due to the concentration of light envelope in those regions, while for speckle patterns, it is a randomly distributed granular structure that is produced. This signifies that the formation of caustic network along the propagation of the beam can be identified by the generation of significantly high intensity localised structures.

We plot in Fig. 3.3(a,b)(iii) the evolution of the maximum intensity detected in each xy-plane along the propagation distance z. The black solid curve at each figure plots the maximum intensity evolution for the specific phase mask under study, while the blue dotted curve plots the average maximum intensity evolution calculated from 10 masks with different random phase distribution patterns of the same $\varphi_{\max}$. We can see that for both weak ($\varphi_{\max} = 2\pi$) and strong ($\varphi_{\max} = 10\pi$) phase modulation, intensity extrema are found in the initial propagation of the beam. The intensity distributions taken at the extrema points of the black solid curves are presented in Fig. 3.4(a)(i,ii) and 3.5a(i,ii), which show the formation of caustic networks in this initial propagation regime (the caustic regime).

Comparison between Fig. 3.3(a)(iii) and (b)(iii) shows that stronger phase modulation leads to the formation of higher intensity caustic network occurred at a shorter distance. For the specific phase masks used in this study, the maximum intensity of the caustic network generated by the phase modulation with $\varphi_{\max} = 10\pi$ is ≈ 8 times higher than that from $\varphi_{\max} = 2\pi$, while being formed at a distance of ≈ 10 times shorter. The dependency of the maximum intensity and the distance to the caustic regime, on the phase modulation strength, are plotted in Fig. 3.3(c). Note that in order to reduce the fluctuation on the curve due to the randomness of the phase mask, the graphs are plotted using the average value of each parameter taken from the average maximum intensity evolution curve (the blue dotted curve) plotted in Fig. 3.3(a,b)(iii).

The relation between the maximum intensity of the caustic structures I_{caustic} and the phase modulation strength $\varphi_{\max}$ (purple open circles in Fig. 3.3(c)) is linear, where it can be well fitted by a linear function $I_{\text{caustic}} = 1.85\,\varphi_{\max}$ with coefficient of determination $R^2 = 0.9994$. Whilst the relation between the distance to the caustic regime z_{caustic} and the phase modulation strength $\varphi_{\max}$ (green asterisks in Fig. 3.3(c)) can be approximated by a power function $z_{\text{caustic}} = 314\,/\varphi_{\max}$ μm with coefficient of determination $R^2 = 0.9146$, which shows the inverse proportional relation between the two quantities.

These relationships can be understood as follows. A thin lens with focal length f is known to impart a quadratic phase shift to the transverse parameter x, y of the input electric field [191], which in one-dimension can be written as

$$\phi(x) = -\frac{kx^2}{2f}.$$

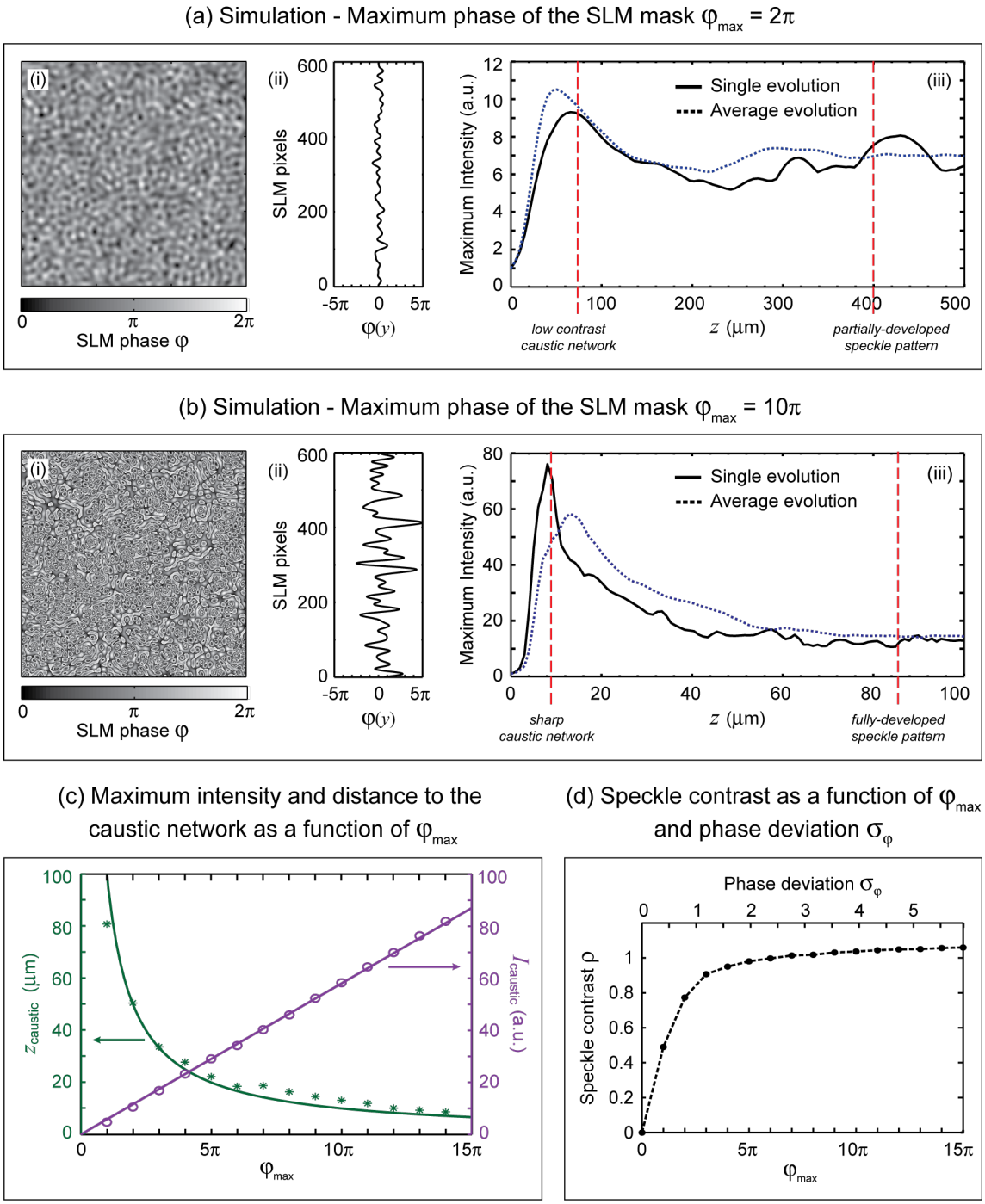

Figure 3.3: Numerical simulations of two-dimensionally phase modulated beam with (a) weak phase modulation of 2π and (b) strong phase modulation of 10π. For (a) and (b), (i) shows the applied phase distribution to the SLM; (ii) shows the unwrapped slice of the applied phase distribution at $x = 0$; (iii) plots the evolution of the maximum intensity of the spatial patterns along the propagation distance z. Black solid curve plots the evolution for the phase mask plotted in (i), while blue dotted curve plots the evolution of the averaged maximum intensity calculated from 10 different phase masks with the same $\varphi_{\max}$. Vertical red dashed lines correspond to the locations from where each intensity patterns plotted in Fig. 3.4 and 3.5 are taken. (c) The maximum intensity I_{caustic} (green asterisks) and the distance to the caustic regime z_{caustic} (purple open circles) as function of phase modulation strength $\varphi_{\max}$. The solid curves are the approximated functions, $I_{\text{caustic}} = 1.85\,\varphi_{\max}$ (green line) and $z_{\text{caustic}} = 314\,/\varphi_{\max}$ μm (purple line). The intensity here is normalised to the intensity of the incident beam. (d) Speckle contrast ρ as function of phase modulation strength $\varphi_{\max}$. The curves plotted in (c) and (d) are averaged from 10 different phase masks for each $\varphi_{\max}$.

For a lens with diameter D, the maximum phase shift imparted across the center of the lens can then be related to the focal length f by evaluating the above equation with $x = D/2$,

$$\phi_{\max} = \frac{kD^2}{8f}.$$

Considering that a random refracting surface is constituted of randomly distributed tiny lenses with typical transverse width $\bar{d}$ and typical maximum phase shift (approximated by two times the phase deviation $2\sigma_\varphi$), the distance to the caustic regime z_{caustic} can then be approximated by

$$z_{\text{caustic}} = \frac{k\bar{d}^2}{16\sigma_\varphi} = \frac{\pi\bar{d}^2}{8\lambda\sigma_\varphi} \approx \frac{75}{\sigma_\varphi} \approx \frac{589}{\varphi_{\max}},$$

where the typical transverse width $\bar{d}$ here is 11 μm obtained from the calculated autocorrelation function. Relating the maximum phase shift $\varphi_{\max}$ to the standard deviation of the phase σ_φ is obtained from numerical modelling as $\varphi_{\max} \approx 7.85\,\sigma_\varphi$.

Although the coefficient of $\varphi_{\max}^{-1}$ here is quite different with the calculated value ($314\,/\varphi_{\max}$), this approximation clearly shows that the distance to the caustic regime is indeed inversely proportional to the phase modulation strength. The discrepancy of the coefficient obtained here is mainly due to the approximation of typical maximum phase shift as two times the phase deviation $2\sigma_\varphi$.

The proportionality of the maximum intensity I_{caustic} and the phase modulation can be understood as stronger focussing power yields smaller size of formed caustic structures (similar to the area of a beam being focalised by a lens), thus stronger intensity caustics.

At longer distance along the propagation, the evolution of the maximum intensity curve plotted in Fig. 3.3(a,b)(iii) also shows a significant difference. For $\varphi_{\max} = 2\pi$, relatively high maximum intensity (almost comparable to the one generated in the caustic regime) can still be found in further propagation distance. Whilst for $\varphi_{\max} = 10\pi$, the maximum intensity decreases monotonically with propagation to an intensity much lower than the one generated in the caustic regime, which indicates a more pronounced difference between the caustic and speckle regime. Indeed, this contrast can be expected considering that only a low contrast caustic network and a partially-developed speckle are formed when the phase modulation is weak (Fig. 3.4(a,b)(i,ii)), while a sharp (high contrast) caustic network and a fully-developed speckle pattern are formed in the case of a strong phase modulation (Fig. 3.5(a,b)(i,ii)).

We plot in Fig. 3.3(d) the relation between the phase modulation and the corresponding speckle contrast ρ (Eq. 3.1) being formed, where the curve shows similar properties as those reported in Ref. [186] and [187]; for weak phase modulation, the speckle contrast is linearly proportional to the phase modulation, but further increment of the phase modulation leads to the deviation from this linear dependency to the saturation of the speckle contrast ρ towards 1. We plot the speckle contrast ρ here as a function of both the maximum phase modulation $\varphi_{\max}$ and the standard deviation of the phase variation σ_φ (following the convention used in Ref. [186] and [187])).

Fig. 3.4 plots the simulation results of the phase modulated beam with $\varphi_{\max} = 2\pi$ (the phase mask is shown in Fig. 3.3(a)(i)). A caustic network structure with very low contrast is formed in the early stage of the propagation, followed by the evolution towards a partially-developed speckle

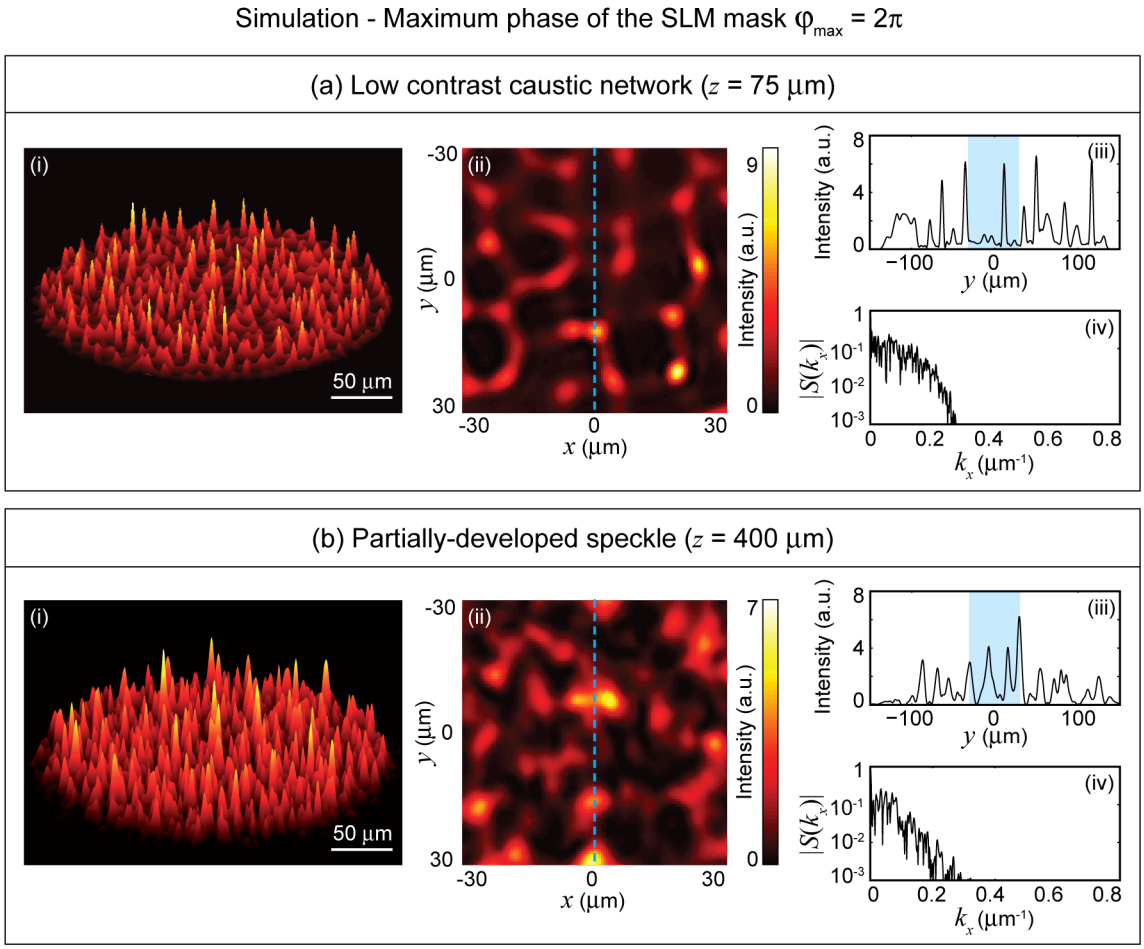

Figure 3.4: Numerical simulations with phase modulation of $\varphi_{\max} = 2\pi$ taken at two different regimes: (a) caustic regime and (b) speckle regime. The caustic network formed in this case has low contrast structures and the speckle pattern is partially developed. For each case, (i) shows the computed intensity distribution; (ii) shows a zoom over a more limited region (the highlighted region in (iii)) looking down on the pattern; (iii) shows a slice of the intensity distribution taken at $x = 0$ (indicated by the dotted line in (ii)); (iv) shows the calculated spatial spectrum corresponding to the intensity distribution in (iii). The intensity here is normalised to the intensity of incident beam.

pattern along the propagation. The caustic network plotted in Fig. 3.4(a) is taken at $z = 75$ μm from the SLM, while the partially-developed speckle plotted in Fig. 3.4(b) is taken at $z = 400$ μm, which corresponds to the distances marked as red dashed lines in Fig. 3.3(a). The low contrast properties of the partially-developed speckle is confirmed by the speckle contrast that is less than 1 (≈ 0.82).

Fig. 3.5 plots the simulation results of the phase modulated beam with $\varphi_{\max} = 10\pi$ (the phase mask is shown in Fig. 3.3(b)(i)). A significantly high contrast (sharp) caustic network of lines along which light is strongly focussed is formed in the early stage of the propagation, followed by the evolution towards a fully-developed speckle pattern along the propagation. The caustic network plotted in Fig. 3.5(a) is taken at $z = 9$ μm from the SLM, while the speckle plotted in Fig. 3.5(b) is taken at $z = 85$ μm, which correspond to the distances marked as red dashed lines in

Fig. 3.3(b). The high contrast properties of the speckle is also confirmed by the speckle contrast that is very close to 1 (≈ 0.99).

In particular, we can observe some clear "hot spots" of intensity peaks being formed at the intersections of caustic lines that construct the network structure, yielding the extreme focussings of light. Notice also that the maximum intensity of this sharp caustic network is an order of magnitude (10.4 times) higher than the one of partially-developed speckle (Fig. 3.4(b)). This particular intensity contrast between these two types of random intensity patterns is therefore the main interest of the experiments presented below.

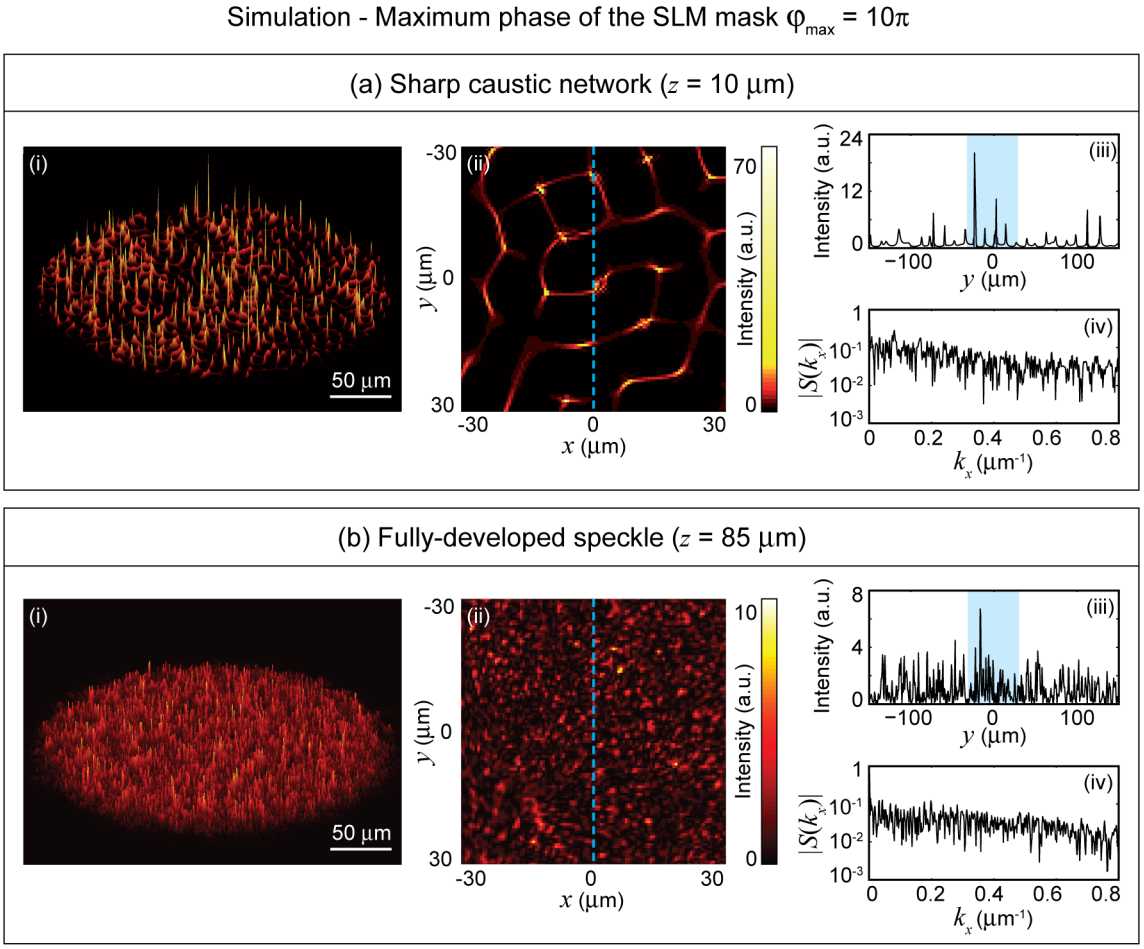

Figure 3.5: Numerical simulations with phase modulation of $\varphi_{\max} = 10\pi$ taken at two different regimes: (a) caustic regime and (b) speckle regime. The caustic network formed in this case is significantly sharper than the one in Fig. 3.4 and the speckle pattern is fully developed. For each case, (i) shows the computed intensity distribution; (ii) shows a zoom over a more limited region (the highlighted region in (iii)) looking down on the pattern; (iii) shows a slice of the intensity distribution taken at $x = 0$ (indicated by the dotted line in (ii)); (iv) shows the calculated spatial spectrum corresponding to the intensity distribution in (iii). The intensity here is normalised to the intensity of incident beam.

The difference of these intensity patterns is also manifested in their very different spatial spectra. Taking a slice of each spatial pattern at $x = 0$ (Fig 3.4(a,b)(iii) and 3.5(a,b)(iii)) and calculating their corresponding spatial spectrum (Fig 3.4(a,b)(iv) and 3.5(a,b)(iv)), much broader spectrum is observed for the case of strong phase modulation. The spatial spectrum $S(k_x, k_y = 0)$

is defined here as:

$$S(k_x, k_y) = \left| \int_{-\infty}^{\infty} I(x, y) e^{i(k_x x + k_y y)} dx\, dy \right|,$$

where k_x and k_y are the spatial frequencies. Note that only the positive spatial frequencies are plotted for each case, since the results are symmetric about $k_x = k_y = 0$.

A quantitative comparison of the spectrum can be made by taking the spatial spectral width (FWHM) of the spatial spectrum Δk_x. In the case of weakly modulated phase, $\Delta k_x \approx 0.1$ μm^{-1}, which is consistent with the typical transverse size of the intensity peaks in the pattern of $\Delta x \approx 8.5$ μm (calculated from its autrocorrelation function). These results confirm the smooth intensity variations typical of a partially-developed speckle. Whilst for strongly modulated phase, $\Delta k_x \approx 2.0$ μm^{-1}, which is consistent with the smaller transverse peak size of $\Delta x \approx 0.5$ μm (measured using autocorrelation function).

3.3.2 Experimental results

We focus here on the experimental study of partially-developed speckle pattern generated by phase modulation with $\varphi_{\max} = 2\pi$ and caustic network structure by phase modulation with $\varphi_{\max} = 10\pi$, corresponding to the simulation results shown in Fig 3.4(b) and 3.5(a), respectively. These two particular intensity patterns are of particular interest due to their resemblance with different elements constituting an ocean wave, which is the topic of our discussion in the next section. Specifically, a smooth partially-developed speckle pattern has a qualitative resemblance to the Gaussian random waves in the ocean, while caustic is the linear mechanism suggested to cause the appearance of rogue waves (see Chapter 2 for related discussions on ocean waves and the linear mechanism of rogue wave formation).

Comparison of the experimental results in Fig. 3.6(a,b) with the numerical results in Figs 3.4(b) and 3.5(a), respectively, shows an excellent qualitative agreement. An exact quantitative agreement between the experimental and simulated patterns is not expected due to the extremely sensitive dependence of the beam profile evolution to any residual phase aberrations present in the experimental system. Nonetheless, the experiments clearly show the same characteristic features seen in the numerical modelling—a smoothly varying intensity distribution for the partially-developed speckle and a more distinct network structure in the caustic regime. Note that the intensities here are normalised relative to the maximum intensity of the partially-developed speckle in Fig. 3.6(a), in order to highlight the contrast of the intensity peaks between the two intensity patterns. Also, different intensity scales are used in order to have a good contrast of the intensity distributions.

Notice however, that because of the limited dynamic range in experiments, the recorded structures in Fig 3.6 are not as apparent as those observed in simulations. Moreover, in order to capture the peak intensities of the structures, the lower intensity structures could not be resolved, as can be seen in Fig. 3.6(a,b)(iii). Nonetheless, we are still able to identify the caustic network structure, and significantly, the experimentally-measured enhancement of the intensity peaks in the caustic regime is a factor of 9.6, which is comparable to that seen in simulations (10.4). The experimentally-measured spectral characteristics are also comparable to simulations, with transverse peak size in the partially-developed speckle $\Delta x \approx 7.3$ μm and in the caustic network $\Delta x \approx 1.5$ μm.

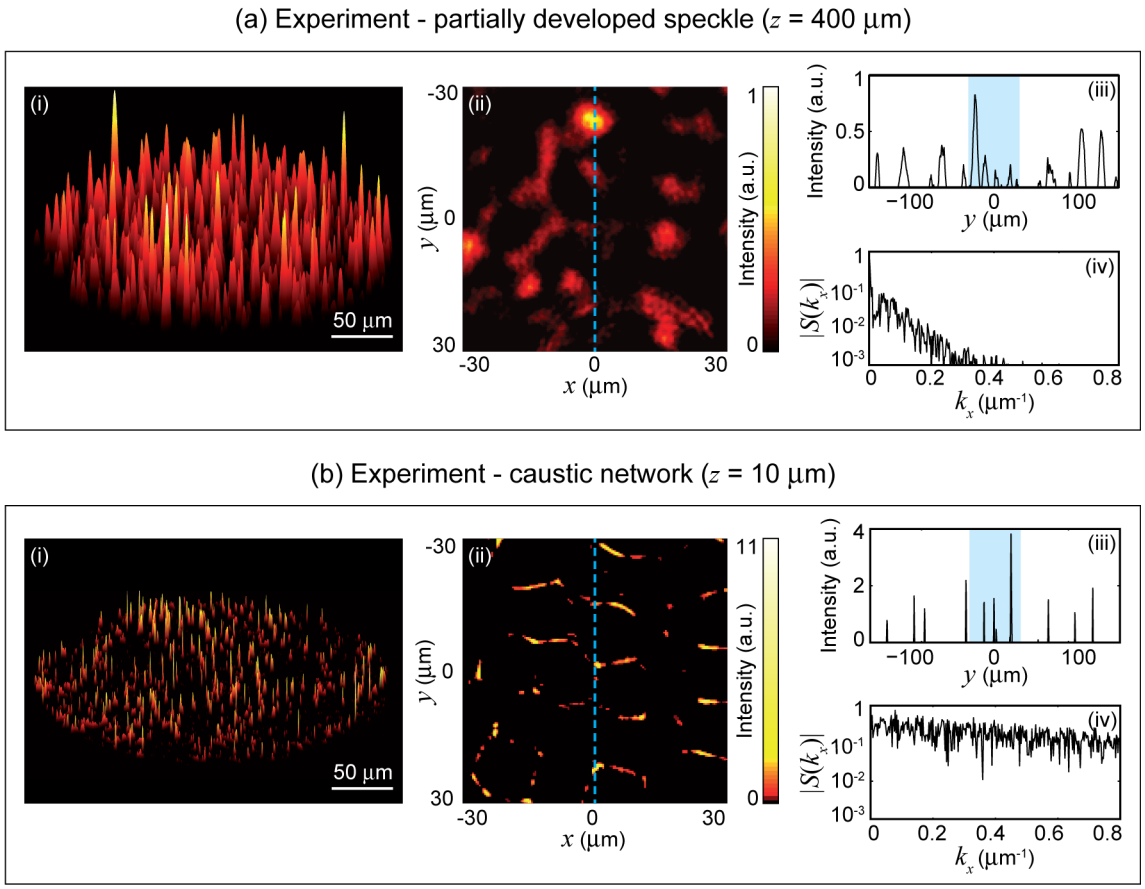

Figure 3.6: Experimental results contrasting (a) partially-developed speckle and (b) a caustic network. For each case, (i) shows the recorded intensity distribution; (ii) shows a zoom over a more limited region (highlighted region in (iii)) looking down on the pattern; (iii) shows a slice of the intensity distribution at $x = 0$ (indicated by the dotted line in (ii)); (iv) shows the calculated spatial spectrum corresponding to the intensity distribution in (iii). The intensities shown here are normalised relative to the maximum intensity for the partially-developed speckle in (a).

3.3.3 Statistical properties and rogue waves

The studies of linear mechanisms of optical rogue wave formation are mostly performed in speckle regime of the optical field, where the statistics is taken from the intensity distribution and/or the intensity peaks of the intensity pattern under study [5, 32, 84]. In a similar way, we use in what follows these two statistical approaches. However, due to the truncation of the low intensity data from the measurement (see Fig. 3.6(a,b)(iii)), the intensity distribution statistics are taken only from the simulation results. Nonetheless, the intensity peak statistics can still be computed from the experimental results, and shown to be in a good agreement with the statistics computed from the simulation results.

Statistical analysis of intensity distribution

Fig. 3.7 plots the probability density distributions of all intensity points of the intensity patterns shown in Fig. 3.4 and 3.5. For both weakly and strongly phase modulated beam, we compare the

statistical distributions of the intensity patterns taken in the caustic and speckle regime. For the case of $\varphi_{\max} = 2\pi$, plotted in Fig. 3.7(a), similar distributions are obtained from the intensity patterns taken both in the caustic regime (black circles) and the speckle regime (blue asterisks). Whilst for the case of $\varphi_{\max} = 10\pi$, plotted in Fig. 3.7(b), different statistics are clearly observed between the one taken in the the caustic regime (black circles) and the speckle regime (blue asterisks). In particular, we can see that the strong focussing in the form of the sharp caustic network results on a stretched exponential distribution, which significantly increase the occurrence of high intensity events compared to the statistical distribution of the speckle pattern.

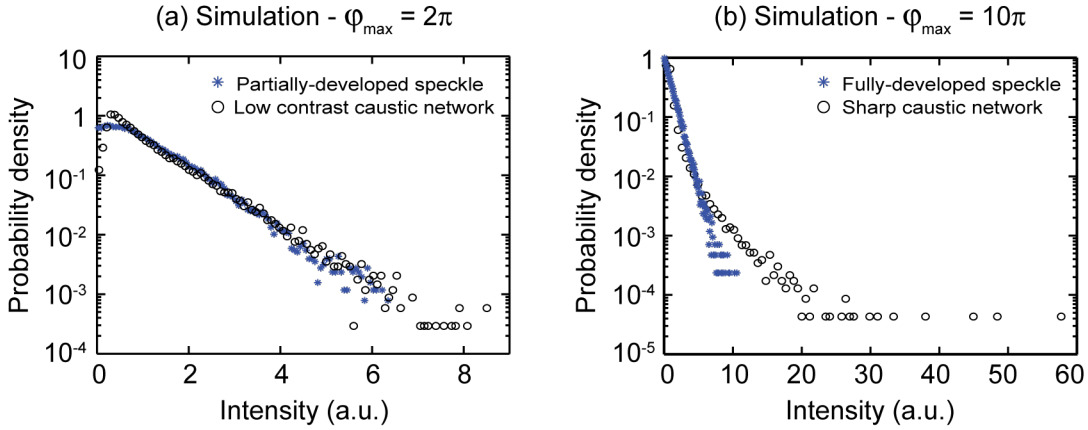

Figure 3.7: Probability distributions of intensity calculated over all field points (taken within the beam profile area) of the simulation results shown in Fig. 3.4 and 3.5. The figure plots the statistical distributions of phase modulated beam with (a) $\varphi_{\max} = 2\pi$ and (b) $\varphi_{\max} = 10\pi$. For each, the statistics between the intensity patterns taken in the caustic regime (black circles) and in the speckle regime (blue asterisks) are compared.

Notice that the shape of the probability distribution calculated from the intensity pattern in the speckle regime is also in correspondence with the type of the speckle pattern observed. Indeed, the intensity statistics of a fully-developed speckle pattern has been known to follow a negative exponential distribution, follows by the transition towards less skewed distribution for a partially-developed speckle [186, 192–194].

Statistical analysis of intensity peaks

Fig. 3.8 compares the probability distributions of intensity peaks computed from the numerical simulation results (black circles) and experimental results (red asterisks). The intensity peaks are detected over the two-dimensional spatial intensity patterns, from the partially-developed speckle patterns in Fig. 3.4(b) and Fig. 3.6(a) (the statistics are compared in Fig. 3.8(a)), and from the caustic network in Fig. 3.5(a) and Fig. 3.6(b) (the statistics are compared in Fig. 3.8(b)). The peak detection was carried out using an 8-connected neighborhood regional maximum search, using thresholding to avoid counting the subsidiary maxima of primary peaks.

Unlike the well-known exponential distribution of speckle pattern intensity, the statistics of the intensity peaks are more complex [190, 195]. In the context of rogue waves, it is of particular interest to examine whether these intensity peak distributions show any evidence of significant long tails with events exceeding accepted criterion for rogue waves. To this end, the rogue wave intensity

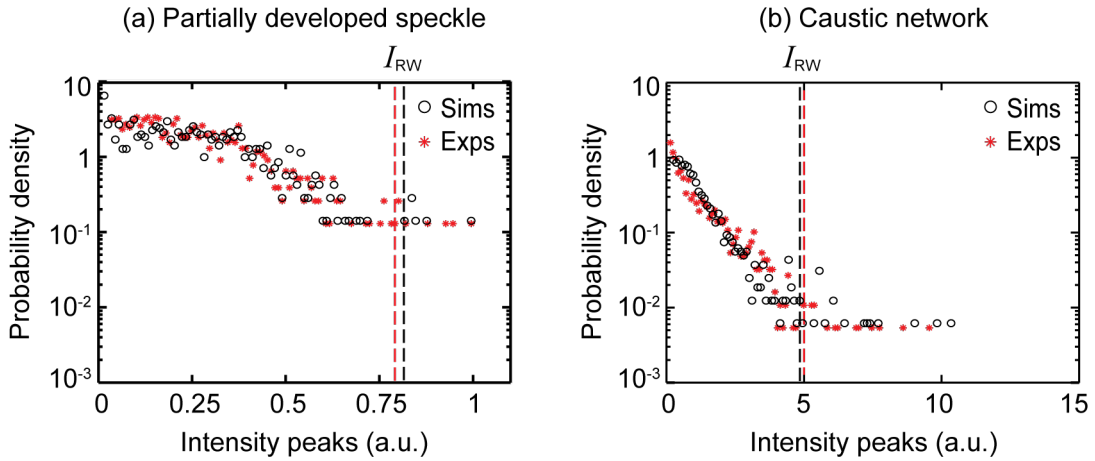

Figure 3.8: Probability distributions from intensity peak analysis of (a) partially-developed speckle pattern and (b) caustic network. For each, the statistical distributions computed from the simulation results (black circles) are compared to the one of the experimental results (red asterisks). The black dashed lines correspond to the rogue wave intensity criterion I_{RW} calculated from the numerical simulation results, while the red dashed lines correspond to the criterion calculated from the experimental results.

threshold, adapted from the oceanographic definition (see Section 2.2), is defined as $I_{\mathrm{RW}} = 2I_{\mathrm{S}}$, where the "significant intensity" I_{S} is the mean of the upper third of events in the distribution [6]. The threshold calculated from the simulation results are marked as black dashed lines, while those calculated from the experimental results are marked as red dashed lines.

We can see the qualitative agreement between the statistics extracted from simulations and experiment for both the partially-developed speckle and the caustic regime, where the general form and width of the probability distribution seen in experiment are well reproduced by the simulations. Concerning the rogue wave criteria, 2.3 % of events in the simulated caustic network are found to exceed the criterion I_{RW}, while it is only 0.2 % for the partially-developed speckle. In experiment, 1.3 % of events in the caustic network are found to exceed the criterion I_{RW}, compared to only 0.5 % for the partially-developed speckle. In conclusion, the results here highlight the physical connection between the formation of caustic networks in the optical field and the formation of high intensity peaks that greatly exceed the calculated rogue wave criterion.

3.4 Generation of an "Optical Sea"

Although a direct mathematical analogy between the three-dimensional focussing mechanism above and the focussing of ocean waves cannot be drawn, the spatial patterns of the beam formed at a certain distance could bear some resemblence with the surface variation of the ocean at a certain time. In particular, one could find a similarity between the smoothly varying partially-developed speckle pattern and the two-dimensional sea surface variation. Motivated from this observation, we aim here to construct a spatial pattern mimicking the spatial variation of sea surface under the influence of some focussing effects, from where similar statistical properties of ocean waves with a small number of rogue waves can be obtained (see Section 2.2).

The phase mask used in this experiment is shown in Fig. 3.9(a). The pattern of the mask is generated from the superposition of a weak amplitude fluctuation pattern of short spatial period

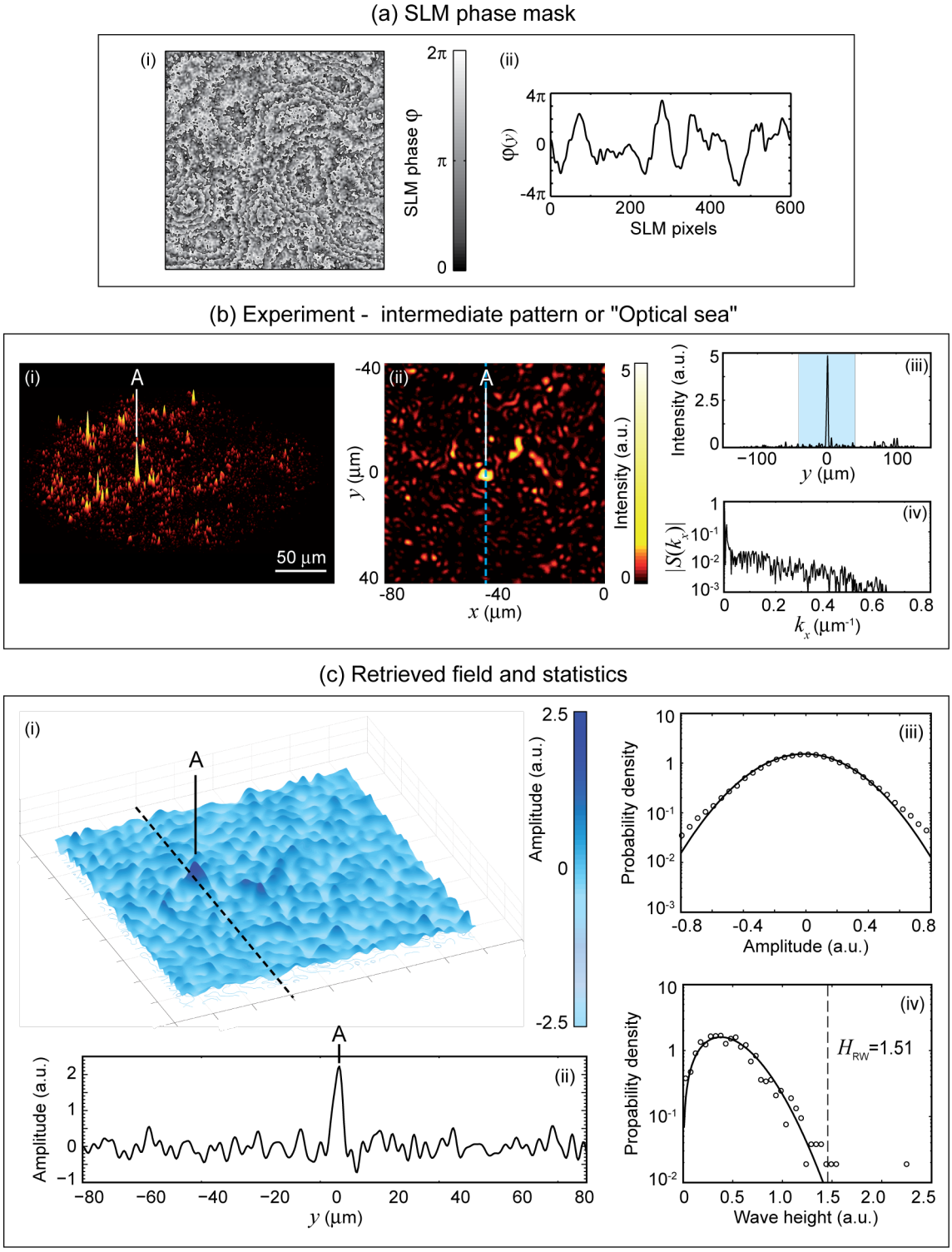

Figure 3.9: Experimental results showing a spatial pattern with resemblance to a random sea surface, which we refer to as an "optical sea". (a) Shows the applied SLM phase. (b) Measured intensity pattern at 220 μm, presented in a similar way as above. The intensity here is also normalised relative to the maximum intensity for the partially-developed speckle in Fig. 3.6(a). (c) Shows (i) the retrieved amplitude pattern; (ii) a slice taken at the position where the highest peak A with amplitude ≈ 2.23 is observed, dashed line in (i); Computed statistics of (iii) elevation and (iv) wave height. The solid lines in (iii) and (iv) plot Gaussian and Rayleigh distribution fits respectively. The label H_{RW} indicates the rogue wave height threshold.

(similar to the one shown in Fig. 3.3(a)(i)) and a strong amplitude fluctuation of larger spatial period. In this way, the generated field exhibits the superposition of a smooth random wave background and a spatial focussing pattern, corresponding to a spatial spectrum intermediate between that of the partially-developed spectrum and the caustic network as shown in Fig. 3.9(b)(iv).

The experimental results showing this superposition intensity pattern are plotted in Fig. 3.9(b). In a similar way as presented above, Fig. 3.9(b)(i) and Fig. 3.9(b)(ii) show the recorded intensity pattern from different angle of view, while Fig. 3.9(b)(iii) plots the slice of the intensity pattern at $x = 0$ and Fig. 3.9(b)(iv) plots the spatial spectrum corresponding to this slice. We can indeed see that the intensity pattern formed in this case exhibits the characteristics of both the partial speckle and the caustic patterns described above. In particular, we see more strongly localised peaks than in the partially-developed speckle shown in Fig. 3.6(a), but without the network structure of the caustic regime in Fig. 3.6(b). Quantitatively, we can also see that the peak intensity value of ≈ 5 is also intermediate between that observed for the partially-developed speckle and the caustic network.

As discussed in Section 2.2, the main quantities of interest of ocean wave statistics are the surface elevation and the wave height (measured trough-to-crest or crest-to-trough relative to the zero-level of the undisplaced water surface). A closer approach to the study of ocean wave statistics therefore requires the extraction of amplitude variation from the intensity pattern recorded by the CCD camera. To this end, we use optical phase retrieval techniques to recover the associated phase and reconstruct the electric field distribution for the propagating field [196, 197]. The phase retrieval technique involved recording the two-dimensional intensity patterns at a number of planes in the measurement region and using the iterative Gerchberg-Saxton algorithm [196]. In our case, we recorded intensity patterns at 100 longitudinal points (spaced by 5 μm) and we used similar algorithm applied in Ref. [197]. Details of the algorithm we applied here can be found in Appendix B.2.

Fig. 3.9(c)(i) plots the retrieved field amplitude extracted from the intensity profile shown in Fig. 3.9(b), where fluctuation with both positive and negative values relative to a mean value of zero is obtained. This amplitude profile clearly shows a visual resemblance to the perturbed surface of a fully-developed sea [15, 95], which can also be seen from the slice plotted in Fig. 3.9(c)(ii).

Based on this two-dimensional wave field, it is then straightforward to determine the statistics of the field amplitude (corresponding to surface elevation) and the wave height. For each, the probability distributions are calculated from the histograms, which are plotted on log scale (circles) in Fig. 3.9(c)(iii) and (c)(iv). We found that the statistics of the field amplitude can indeed be well-fitted over the central region by a Gaussian distribution (solid line in Fig. 3.9(c)(iii)), while the corresponding wave height (calculated trough to crest) distribution can be well-fitted by a Rayleigh distribution (solid line in Fig. 3.9(c)(iv)). The wave height are extracted from the two-dimensional field profile by taking a series of slices parallel to the x-direction separated in y by a distance greater than the average wavelength estimated from the average zero-crossing period [49] and then measure (up-crossing) heights based on trough-to-crest distance across a zero-crossing point.

In both cases, some outliers at larger elevation and larger wave height are found to exceed the fitted distributions, which are associated with the rare high amplitude waves corresponding to the

higher spatial frequencies in the spectrum. Indeed, these deviations of statistics of elevation and wave height from Gaussian and Rayleigh distributions show that the emergence of rogue waves can be expected from a fully linear theory. Note that the probability distribution fits (Gaussian, Rayleigh) shown to the data in Fig. 3.9(b) were confirmed using a Kolmogorov-Smirnov test, with the null hypothesis accepted at the 0.05 significance level.

Additionally, the rogue wave threshold for the wave height statistics is calculated from $H_{\mathrm{RW}} = 2H_{\mathrm{S}} = 1.51$, where the significant wave height H_{S} is the mean of the upper third of events in the distribution. This threshold is plotted as dashed line in Fig. 3.9(c)(iv), where 0.2 % of the wave heights are found to exceed this threshold and therefore can be described as rogue waves. We also see clearly how the deviation from the Rayleigh fit in the tail occurs at a wave height close to the calculated H_{S}. Note that the general features of the statistics (Gaussian for elevation and Rayleigh for wave height) are observed over a range of measurement distances in the experimental setup, and also that the wave height statistics does not depend on the particular direction in which the field slices are taken.

3.5 Conclusions

The use of a spatial light modulator to impose random phase on a coherent field has provided a flexible means of studying the rogue wave formation and their statistics in purely linear optical system. We investigate two-dimensional and three-dimensional focussing and detect the occurrence of extreme localisations in both cases. Specifically, we compare the effect of refraction by weakly and strongly random refracting surfaces.

Based on the similarity of the equation governing the wave propagation in both systems, the study of two-dimensional focussing can be linked directly to the formation of rogue waves in the ocean generated by spatial caustic (discussed in Section 2.3.1). Moreover, since the propagation of light in this setup can still be predicted accurately by the paraxial wave equation, we suggest that these results can also be observed in a linear (dispersive) propagation of temporally modulated light in an optical fibre, where the transversal dimension y in this case is replaced by time t.

In the case of three dimensional focussing, we identify the development of caustic network structure as the physical mechanism generating large amplitude events that satisfy commonly-applied criteria for rogue waves. We have shown that the transverse size of the high intensity peaks in the pattern can be correlated with the corresponding spatial spectral width, complementing studies in oceanography that show how spectral content is very important in rogue wave generation [3]. We also perform statistical analysis of the optical intensity distribution and show that a purely linear system can indeed exhibit heavy tailed statistics. Qualitative agreement between simulation and experimental results on the statistics of intensity peaks have also been shown.

Finally, the ability to perform phase retrieval on the recorded intensity pattern has allowed us to determine their amplitude statistics. In particular, we study a superposition pattern of a partially-developed speckle and a caustic network, which is designed to generate an amplitude distribution of an “optical sea”, a pattern similar to ocean wave exhibiting small number of rogue waves. The statistical analysis of this specific pattern shows the effect of high frequencies on extending the tails of Gaussian distribution for the elevation and Rayleigh distribution for the wave height.

Chapter 4

Rogue waves in spontaneous modulation instability

The emergence of rogue waves has often been associated with the role of nonlinearity through the phenomenon of modulation instability, as discussed in Section 2.3.2 and 2.4.2 [172–174]. In this context, the propagation of waves is generally described by the nonlinear Schrödinger equation (NLSE) or its extensions. The NLSE is a universal equation governing wave dynamics of many nonlinear dispersive systems, such as deep water wave groups, pulse propagation in optical fibres, plasmas and cold atoms [6, 20, 23, 24].

Modulation instability (MI), also known as Benjamin-Feir instability, is a phenomenon where a weak modulation on a continuous wave background undergoes exponential growth along the propagation [122, 131]. This initial exponential growth of the modulation is known to be followed by a decay of the modulation back to the initial state, leading to a growth-return evolution in a form of Fermi-Pasta-Ulam (FPU) recurrence [198]. Although the initial mathematical studies of MI were performed using linear stability analysis [122], the growth and decay dynamics of MI can also be described in terms of the analytical solutions of the NLSE in the form of "breather" or "soliton on finite background" (SFB) solutions [199–202].

Although these SFB solutions have been generated experimentally in both optical fibre systems and hydrodynamic wave tanks using controlled initial conditions, their relation to the coherent localised structures appearing randomly in a noise triggered MI field (spontaneous MI field) has not been a subject of detailed study. In particular, we analyze here the properties of the emergent peaks in the spontaneous MI field over their full intensity range, which differs from previous studies that are focussed on particular analytical solutions [7, 18, 203].

Other properties of spontaneous MI field are also investigated in more depth in this chapter, including the evolution of the MI spectrum along the propagation and the correlation to the emerged localised structures, the short term and long term behaviour of the temporal and spectral evolution along the propagation, and various statistical properties of the spontaneously emergent localised structures and their relation to the emergence of rogue waves.

Note that the results presented here are based only on numerical simulations. However, since the analysis is performed under the standard (dimensionless) form of the NLSE, these results may

apply to any physical system whose dynamics are governed by the equation. The experimental realisation of this study in fibre optics is discussed in the next chapter.

4.1 Modulation instability and breather solutions

In section 2.3.2 and 2.4.2, we have shown that both the *water wave* NLSE and *fibre-optics* NLSE can be transformed into the *dimensionless time* NLSE (the derivation can be found in Appendix A.1)

$$i\frac{\partial\psi}{\partial\xi} + \frac{1}{2}\frac{\partial^2\psi}{\partial\tau^2} + |\psi|^2\psi = 0 \tag{4.1}$$

with complex envelope $\psi(\xi,\tau)$ evolving as a function of propagation distance ξ and co-moving time τ. The second term of this equation takes into account the dispersion and the last term takes into account the nonlinearity.

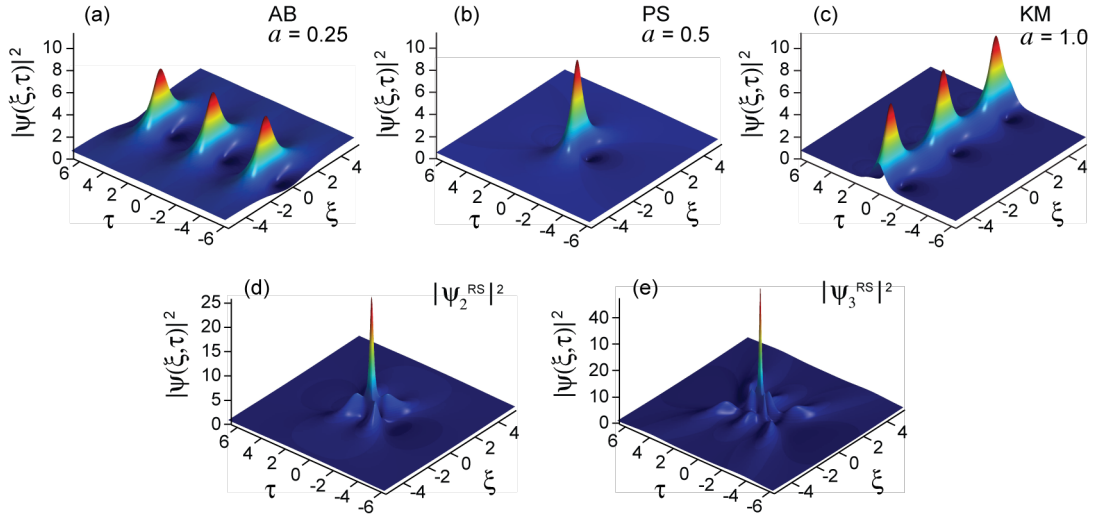

Figure 4.1: SFB solutions derived from Eq. 4.2 for different values of the parameter a as indicated: (a) Akhmediev breather (AB). (b) Peregrine soliton (PS). (c) Kuznetsov-Ma (KM) soliton. (d) and (e) second- and third-order solutions for the case of maximum intensity (the rational solutions).

4.1.1 First-order solutions

The NLSE is an integrable equation which can be solved via the Inverse Scattering Transform (IST). Since the pioneering work of Zakharov and Shabat [115], there has been continued interest in the mathematics and physics of the analytical solutions of the NLSE [204–207]. Although the most celebrated NLSE solution is the stationary propagation-invariant bright soliton, there is also extensive literature studying the properties of various types of "breather", localised nonlinear structures evolving upon a non-zero background plane wave, which is also known as "soliton on finite background" solutions.

In the context of our discussion here, we consider the SFB solutions to the *dimensionless* NLSE (Eq. 4.1) written in the form [199, 204]

$$\psi(\xi,\tau) = \left[1 + \frac{2(1-2a)\cosh(b\xi) + ib\sinh(b\xi)}{\sqrt{2a}\cos(\omega\tau) - \cosh(b\xi)}\right] e^{i\xi}, \tag{4.2}$$

where the second term of the equation is the "non-background" term, highlighting the fact that we have a dynamical structure evolving on a background. The properties of this solution are determined by one single positive parameter a ($a \neq 0.5$), through arguments $b = \sqrt{8a(1-2a)}$ and $\omega = 2\sqrt{1-2a}$. Fig. 4.1(a-c) shows how, as the parameter a varies, different behaviour in the solution is seen with localisation in space, time, or both.

Over the range $0 < a < 0.5$, Eq. 4.2 describes the Akhmediev breather (AB), a temporally-periodic pulse train that undergoes a single growth-decay cycle along ξ [18, 199]. In the context of nonlinear fibre optics, it is this growth phase of the AB solution that describes the initial exponential growth of a weak perturbation in the framework of MI. In this case, the real parameter ω gives the frequency of modulation on the perturbed plane wave, and the real parameter b governs the instability growth rate which is maximum for $a = 0.25$ ($\omega = \sqrt{2}$). The MI gain curve as a function of modulation frequency ω and parameter a is plotted in Fig. 4.2(a).

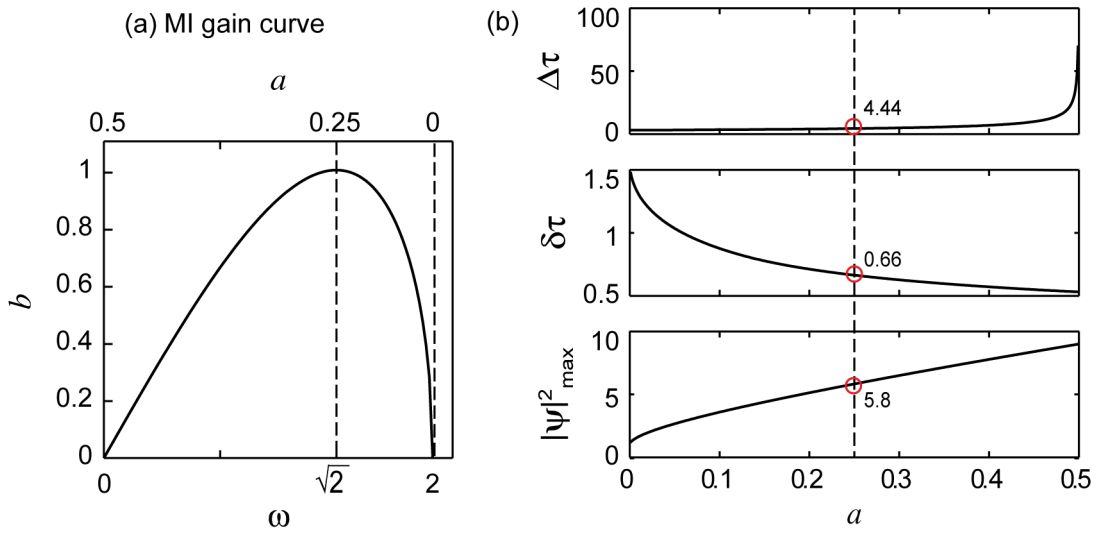

Figure 4.2: (a) Modulation instabiility gain as a function of modulation frequency ω and parameter a. Dashed lines indicate the modulation frequency at maximum MI gain ($a = 0.25$) and the cut-off frequency. (b) The evolution of temporal period $\Delta\tau$, temporal pulse width $\delta\tau$, and maximum intensity of AB structures as a function of parameter a. The red circles indicate the values of these quantities at the maximum of MI gain ($a = 0.25$).

As the parameter a increases, the modulation frequency ω decreases and the temporal period of the AB pulse train increases following

$$\Delta\tau = 2\pi/\omega = \pi/\sqrt{1-2a}. \tag{4.3}$$

The increase of the temporal period is accompanied by the narrowing of the temporal width $\delta\tau$ and the increase of the peak intensity $|\psi|^2_{\max}$, as shown in Fig. 4.2(b). The temporal width (full

width at half maximum) $\delta\tau$ can be calculated by (the derivation is shown in Appendix A.2)

$$\delta\tau = \frac{2}{\omega}\cos^{-1}\left[\frac{1}{\sqrt{2a}}\left(1-\frac{2(1-2a)}{\sqrt{|\psi|^2_{\text{HM}}+1}}\right)\right], \tag{4.4}$$

where $|\psi|^2_{\text{HM}}$ is the half maximum intensity of the AB structure that varies as a function of parameter a. For $a \leq 0.125$,

$$|\psi|^2_{\text{HM}} = 8a+1,$$

while for $a \geq 0.125$,

$$|\psi|^2_{\text{HM}} = \frac{1}{2}\left(2\sqrt{2a}+1\right)^2.$$

The peak intensity of the solution $|\psi|^2_{\text{max}}$ correponds to the intensity at distance $\xi = 0$ and time $\tau = 0$

$$|\psi|^2_{\text{max}} = |\psi(0,0)|^2 = \left(2\sqrt{2a}+1\right)^2. \tag{4.5}$$

It is of particular interest to calculate these quantities at the maximum of MI gain. Using the formulas above, for $a = 0.25$, we obtain the temporal periodicity $\Delta\tau = \sqrt{2}\pi$, the temporal width $\delta\tau = 0.66$, and the peak intensity $|\psi|^2_{\text{max}} = \left(1+\sqrt{2}\right)^2 \approx 5.8$. Note that for consistency with the studies of MI in optics, the results here are plotted and analysed in terms of intensity [6], but their derivations in terms of amplitude can also be found in Appendix A.2.

In the limit $a \to 0.5$ ($\omega \to 0$) the solution as written in Eq. 4.2 is replaced by the rational Peregrine soliton (PS) solution [200]

$$\psi_{\text{PS}}(\xi,\tau) = \left[1-\frac{4(1+2i\xi)}{1+4\tau^2+4\xi^2}\right]e^{i\xi}.$$

The PS solution corresponds to a single pulse with localisation in time τ as well as along the propagation direction ξ. It possesses the narrowest temporal width $\delta\tau_{\text{PS}} \approx 0.53$ and the highest intensity amongst all the family of AB solutions $|\psi_1^{\text{RS}}|^2_{\text{max}} = |\psi_{\text{PS}}|^2_{\text{max}} = 9$. The subscript of the field ψ denotes the order of the SFB solution, while the superscript "RS" is used to denote the rational solution property (solutions of the NLSE that can be expressed in the form of a ratio of two polynomials) [18, 203].

For $a > 0.5$, Eq. 4.2 remains a solution of the NLSE, but the physical nature of the solution changes as circular trigonometric functions become hyperbolic and vice versa (as the parameters b and ω become imaginary). In this case, we obtain the Kuznetsov-Ma (KM) soliton, which shows localisation in time τ but periodicity along ξ with spatial modulation period $\Delta\xi = 2\pi/(ib) = \pi/\sqrt{2a(2a-1)}$ [139, 201]. We can see that as a increases above 0.5, the spatial period $\Delta\xi$ decreases, where it goes to zero (i.e. no periodicity at all) as $a \to \infty$, approaching the fundamental sech-soliton solution (a pulse propagating in an invariant way along ξ).

Each of the solutions described by Eq. 4.2 is a limiting case of a more general two-parameter family of first-order solutions of the NLSE that exhibit periodicity in both transverse time τ and longitudinal propagation direction ξ (bi-periodic solution of the NLSE), which are described by Jacobi elliptic functions [204]. When one of the periods tends to infinity, we obtain either the AB or the KM solution, and when both of the periods are infinite, we obtain the PS which is the

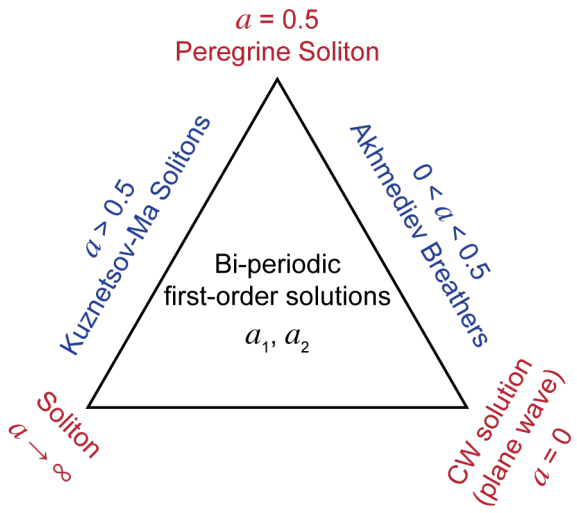

Figure 4.3: Schematic representation of the interrelation between various first-order solutions of the NLSE (adapted from Ref. [7]).

first-order rational solution. The relation between these solutions can be represented as shown in Fig. 4.3.

4.1.2 Higher-order solutions

The first-order solutions are also often referred to as "elementary" SFB solutions of the NLSE. In a real physical system where the MI is generated from noise, the wave is constructed from a nonlinear superposition of many elementary bi-periodic solutions, which can form more complex higher-order solutions. These solutions can be obtained using mathematical techniques such as the Darboux transformation [204]. These solutions possess even stronger localisation characteristics (along both time and space dimensions) and higher intensities than the PS limit.

The exact functional form of higher-order solutions and their highest intensity peaks are dependent on the properties of the elementary constituent breathers. In terms of AB collision, the constructed higher-order solution (higher-order breather) is dependent on the modulation frequency and the "velocity" (the angle formed by the line of maxima of the AB with respect to the *co-moving* time τ axis) of the constituent ABs, and their relative phase shift (the difference on their spatio-temporal center position (ξ_0, τ_0)) [7, 208]. Following the mathematical formulation shown in Ref. [7], each constituent AB can be described by an arbitrary complex number (within certain limits) $l = \mu + i\nu$, whose real part μ corresponds to the "velocity" and imaginary part ν corresponds to the modulation frequency.

The peak intensity of a higher-order breather is dependent on the peak intensities of the contituent ABs. As we have seen earlier, the peak intensity of an AB can be determined from its modulation frequency, represented by parameter a in the discussion above, or parameter ν in this formalism, where the two parameters are related by $\nu = \sqrt{2a}$. The range of AB with $0 < a < 0.5$ we have seen earlier therefore correponds here to $0 < \nu < 1$. A higher-order breather constructed from two ABs of $l = 0.8$ can therefore be expected to have higher intensity peak compared to the one constructed from two ABs of $l = 0.7$.

However, although in general this is indeed the case, the efficiency of an AB collision needs also to be taken into account. The structure of a higher-order breather and its peak intensity are dependent on the interaction between the constituent ABs, which is governed by the parameters ν, μ, and (ξ_0, τ_0) mentioned above. Indeed, as we shall see in the following sections, various structures (with infinite possibilities) of higher-order breathers are formed from noise, which can be described by random combination of these parameters.

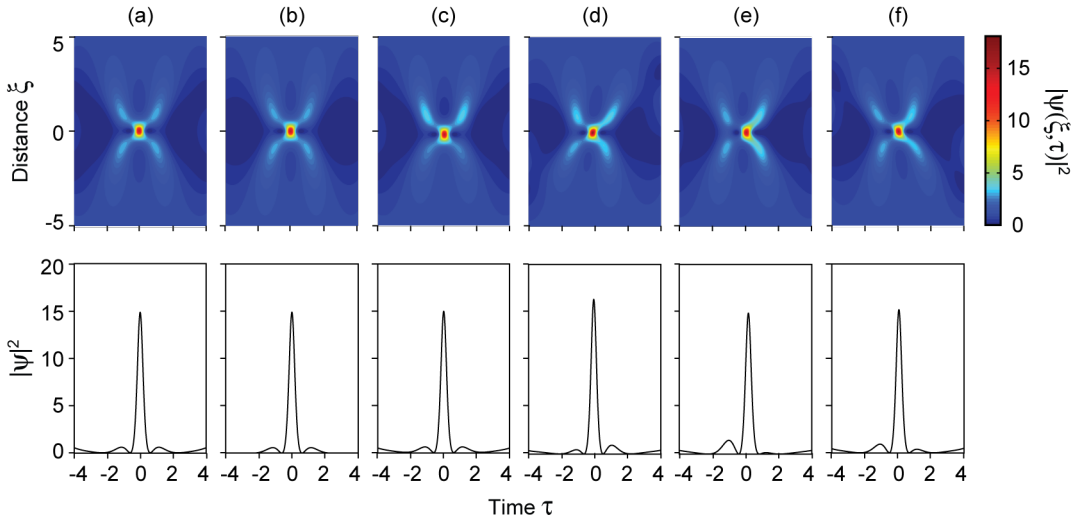

Figure 4.4: Different types of second-order breather structures that are constructed from different combinations of two AB collision with parameters shown in Table4.1. The maximum intensity in all cases is close to 15.

Fig.	ν_1	ν_2	μ_1	μ_2	ξ_{01}	ξ_{02}	τ_{01}	τ_{02}	$\lvert\psi\rvert^2_{\max}$	$\delta\tau$
(a)	0.7	0.73	0	0	0	0	0	0	14.9	0.395
(b)	0.5	0.93	0	0	0	0	0	0	14.9	0.397
(c)	0.7	0.77	0	0	0	$\pi/100$	0	0	15	0.394
(d)	0.7	0.77	0	0.2	0	$\pi/100$	0	0	15.2	0.391
(e)	0.7	0.84	0	0	0	0	0	$\pi/100$	14.9	0.398
(f)	0.7	0.84	0	-0.2	0	0	0	$\pi/100$	16.3	0.377

Table 4.1: Different combination of parameters corresponding to the plot of second-order breathers shown in Fig. 4.4.

To highlight the role of each of these parameters, we plot in Fig. 4.4 several examples of second-order breathers ψ_2, with peak intensity $|\psi|^2_{\max}$ around 15, but constructed from two ABs with different parameters. For each case, the spatio-temporal intensity profile is plotted in the top panel and the temporal cross section taken at the center of the peak intensity is plotted in the bottom panel. The parameters used for each plot, together with the peak intensities $|\psi|^2_{\max}$ and the temporal widths of the corresponding intensity peaks (FWHM) are given in Table 4.1. The notation of the parameters follow the explicit forms used to plot the higher-order breathers given in Appendix C.1.

We first plot in Fig. 4.4(a) and (b) two second-order breathers generated from the collision of two ABs of different modulation frequency, which are perfectly in phase with zero velocity. In figure

(a), the ABs are desribed by $l_1 = 0.7i$ and $l_2 = 0.73i$ (corresponds to $a_1 = 0.245$ and $a_2 = 0.266$), while in figure (b), $l_1 = 0.5i$ and $l_2 = 0.93i$ (corresponds to $a_1 = 0.125$ and $a_2 = 0.432$). We observe that very similar spatio-temporal structures are formed in the two cases. However, notice that although the peak intensities are practically the same, a small difference on the temporal width can be observed. As we shall see in Section 4.3, the possibility of having slightly different temporal width for the same peak intensity leads to the "band" formation observed in the scatter plot shown in Fig. 4.7.

The effects of relative phase and velocity of the contituent ABs can be observed in Fig. 4.4(c-f). Figure (c) and (d) plot two second-order breathers formed by the same modulation frequency combination, $\nu_1 = 0.7$ and $\nu_2 = 0.77$, where in (c) one is simply shifted in space by $\pi/100$, while in (d) one is shifted in space by $\pi/100$ and having a nonzero velocity at the same time. In (c), we observe that the effect of relative phase in space is on the formation of asymmetric breathers about the space ξ-axis, while in (d) the breather is oriented in a certain angle in the spatio-temporal field. Notice also that the maximum intensity together with the temporal width are slightly modified due to the different velocities between the two constituent ABs. Moreover, we can also see in the temporal profile of this breather, the asymmetricity of its two side-wings.

Similarly for the relative phase in time, figure (e) and (f) plot two second-order breathers formed by the same modulation frequency combination, $\nu_1 = 0.7$ and $\nu_2 = 0.84$, where in (e) one is simply shifted in time by $\pi/100$, while in (f) one is shifted and having a nonzero velocity at the same time. In (e), we observe an asymmetric breather about the time τ-axis, while in (f) we can see a "tilted" breather with modified maximum intensity and temporal width. We apply a different sign of velocity here to the one we applied in Fig. 4.4(d) in order to highlight their different effect on the orientation of the breather. Notice that in the two cases here we have the asymmetric side-wings of the temporal profile of the breather.

The maximum possible intensity of the higher-order solutions occurs when we have nonlinear superposition of Peregrine solitons with zero phase difference. In this case the solutions can be written in rational form

$$\psi_n^{\mathrm{RS}} = \left[(-1)^n + \frac{G_n(\xi,\tau) + i\xi H_n(\xi,\tau)}{D_n(\xi,\tau)}\right] e^{i\xi},$$

with G, H, and D are polynomials in the two variables ξ and τ [203]. The explicit expressions of this formalism can be found in Appendix C.2. The maximum intensity of the n-th order rational solution can be calculated by $|\psi_n^{\mathrm{RS}}|^2_{\max} = (2n+1)^2$, where the order n signifies the number of elementary constituent solitons, giving $|\psi_1^{\mathrm{RS}}|^2_{\max} = |\psi_{\mathrm{PS}}|^2_{\max} = 9$, $|\psi_2^{\mathrm{RS}}|^2_{\max} = 25$, and $|\psi_3^{\mathrm{RS}}|^2_{\max} = 49$ for $n = 1$, $n = 2$, and $n = 3$, respectively. Fig. 4.1(d,e) show the three-dimensional plots of these higher-order solutions.

4.2 Noise-driven modulation instability simulations

The aim of the study in this chapter is the properties of the spontaneous MI. To this end, we performed an extensive simulation of MI in the NLSE with a noise-perturbed plane wave initial condition, based on a standard split-step scheme (see Appendix B.3). Starting from a noise-perturbed plane wave of normalized amplitude $\psi(0,\tau) = 1 + \eta(0,\tau)$, the field is propagated along

a distance ξ in a system governed by the pure NLSE. The noise field $\eta(0,\tau)$ here is computed from the inverse Fourier transform of a broadband noise of one photon per mode spectral density with random phase. This is a common noise source used in modelling of spectral broadening processes in optics [209].

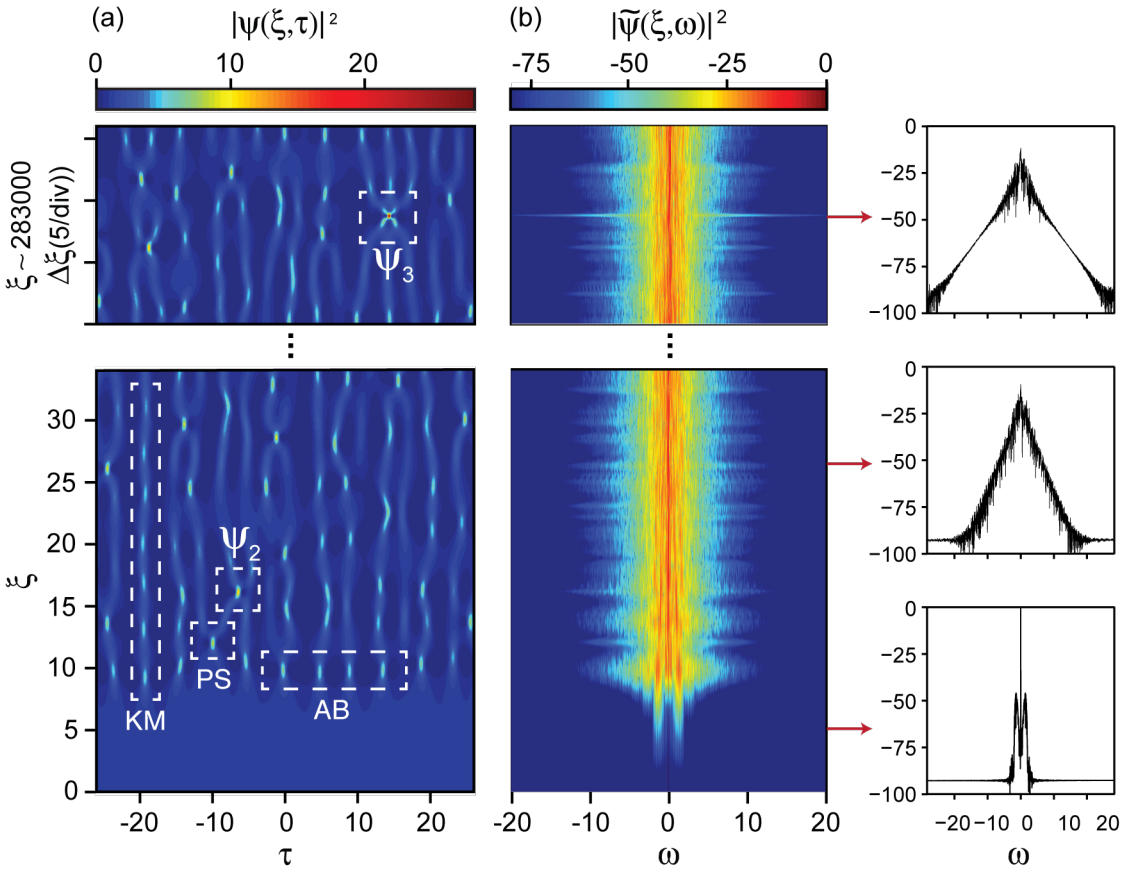

Figure 4.5: (a) Density map showing a small portion of the long term temporal evolution of a spatio-temporal MI field triggered by one photon per mode noise superimposed on a plane wave background. Local regions highlighted by white dashed lines correspond to the intensity profiles shown in Fig. 4.6. (b) Density map of the corresponding frequency evolution. Bottom subfigures plot evolution over $\xi = 0$ to $\xi = 34$; top subfigures plot evolution over a range around $\xi \sim 283000$. (c) The spectral cross section at different distance ξ along the propagation, contrasting the MI spectra at the initial stage $\xi = 5.5$, at a ttypical MI spectral broadening $\xi = 26.3$, and at the emergent of extreme collision of three ABs $\xi = 283211.5$.

To have sufficient data for the statistical analysis, the field is propagated up to $\xi_{\max} = 343750$ (using 6250000 ξ-points), with a temporal window extending to $\tau_{\max} = \pm 69.42$ (using 2048 τ -points). It yielded a total of 2853669 spontaneously emergent localised structures, and with typically 50 temporal points across each peak. Results showing the temporal ($|\psi(\xi,\tau)|^2$) and spectral ($|\widetilde{\psi}(\xi,\omega)|^2$) evolution of the chaotic MI field are shown in Fig. 4.5(a) and 4.5(b) respectively, with the spectral cross sections taken at different distance ξ along the propagation plotted in Fig. 4.5(c). Note that in order to make sure that our numerical results are not dependent on the resolution, we verified that the same results are reproduced for higher resolution (four times higher).

4.3 Spontaneously emergent breathers

We first analyse the time-domain evolution map in Fig. 4.5(a). We can see the spontaneous development of spatio-temporal localised structures from the input noisy plane wave due to the MI. The peaks take the form of a quasi-periodic temporal pulse train when they first appear around $\xi \approx 10$, but then evolve into chaotic MI field in further propagation, where we observe various forms of interaction (merging, splitting) between the individual structures taking place at random space and time.

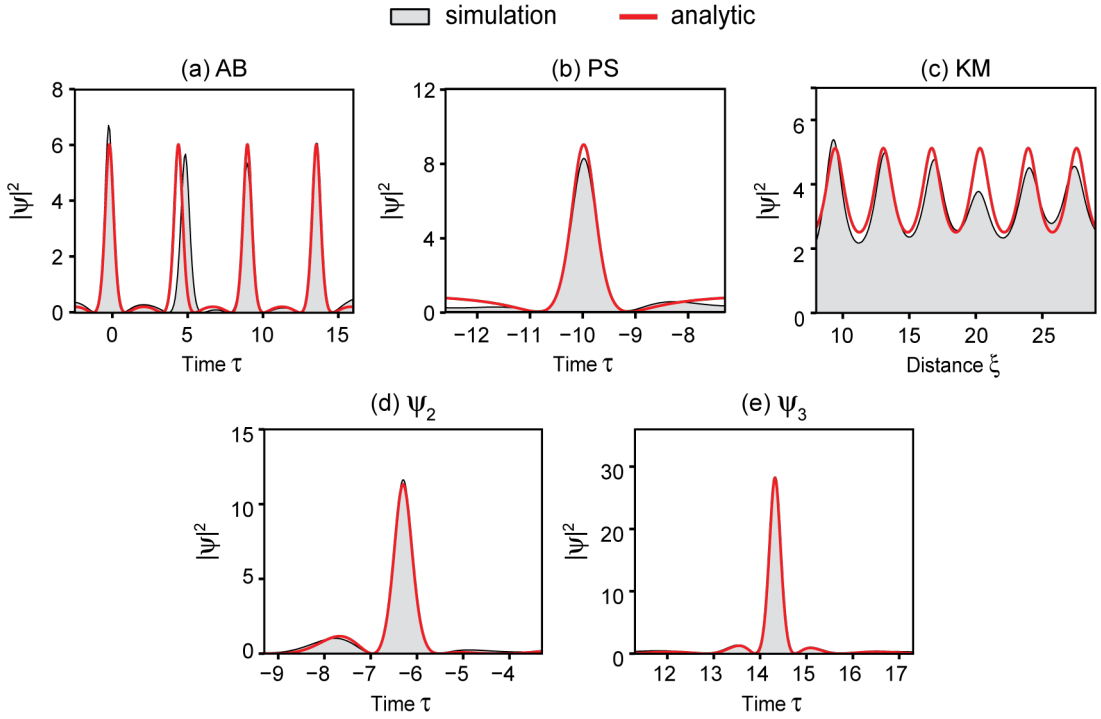

Figure 4.6: The gray shaded plots show the intensity profiles extracted from the regions of the chaotic MI field indicated in Fig. 4.5 for an AB, PS, KM, second-order superposition ψ_2, and third-order superposition ψ_3 respectively, compared with the corresponding analytical NLSE solutions (red solid line).

However, although these peaks emerge from noise, their temporal and spatial characteristics reveal clear signatures of the ideal analytic SFB solutions described above. For example, at the initial point of emergence around $\xi \approx 10$, the average temporal periodicity from the simulations is $\Delta\tau \approx 4.44$, which corresponds to the calculated AB periodicity at maximum MI gain (at $a = 0.25$). Similarly, the average temporal width and the peak intensity of these AB-like structures are also very close with those calculated before (see Fig. 4.2(b)).

In order to have a direct comparison between the emergent MI structures and the analytic SFB solutions, we plot in Fig. 4.6 the intensity profiles from different regions in the spatio-temporal MI field shown in Fig. 4.5(a). Indeed, we can readily identify in the evolution map some regions where the local properties of the MI field bear close resemblance to the analytic SFB solutions given above. We compare in Fig. 4.6(a-c), the cross section of elementary breather structures with the analytical first-order solutions, the AB, PS, and KM. For the AB and PS regions, we extract the temporal intensity taken at the point of maximum localisation (gray shaded), which can be

well fitted with the corresponding calculated AB solution for $a = 0.265$ and PS solution (red line). For KM region, we plot the evolution of the maximum intensity along ξ from simulation (gray shaded), agreeing well with the analytic KM soliton solution for $a = 4$ (red line). Of course, exact agreement is not to be expected given the random initial conditions, but these results very clearly show how the analytic solutions map very closely to the noise-generated structures.

The large data set of our simulation (with $\approx 3 \times 10^6$ distinct intensity peaks) allows us to identify higher-order NLSE solutions with intensities greater than the $|\psi_{\rm PS}|^2_{\rm max} = 9$ limit, which are shown in Fig. 4.6(d,e). A peak arising from the superposition of two breathers is labelled $|\psi_2|^2$ and a peak arising from the superposition of three breathers is labelled $|\psi_3|^2$. We plot in Fig. 4.6(d) and (e) the extracted temporal intensity profile at maximum localisation of second-order and third-order solutions (gray shaded) with peak intensity $|\psi_2|^2_{\rm max} = 11.5$ and $|\psi_3|^2_{\rm max} = 28$, fitted with the analytical solutions (red line) obtained from collision of two ABs of $l_1 = 0.6i$ and $l_2 = 0.7i$ with $\tau_{02} = \pi/100$, and collision of three ABs of $l_1 = 0.62i$, $l_2 = 0.72i$, and $l_3 = 0.82i$ with $\tau_{03} = \pi/8000$. We can see that the peak together with the wing profiles in both cases can be very well fitted by the analytical higher-order breather solutions.

These results strongly suggest a close correspondence between the properties of the analytic SFB solutions and the properties of the localised structures seen in noise-induced MI. In order to obtain more convincing evidence for this interpretation applied to all peaks in the data set, we compare the temporal widths (FWHM) and the peak intensities of these spontaneously emerged breathers with those expected for SFB solutions including elementary and higher-order solutions. In determining the intensity of these peaks, we used an 8-connected neighborhood regional maximum search. We emphasize that this technique needs to be applied carefully (using interpolation and smoothing/low pass filtering) to avoid the detection of small-scale fluctuations on top of the localised structures as distinct peaks. We further applied a minimum relative threshold of $|\psi|^2 = 1$ in order to avoid counting the subsidiary maxima of primary peaks. These results are shown in Fig. 4.7. Here, for each of the $\approx 3 \times 10^6$ peaks in the chaotic MI field, the scatter plot (gray circles) shows the temporal FWHM plotted against the corresponding peak intensity. It is clear that the circles span a continuous range of intensities up to a maximum intensity of ≈ 28, which is in the region of third-order solutions.

We can compare this scatter plot with theoretical predictions for the properties of SFBs using the well-known analytic properties of AB solutions (for intensities < 9), and by using the Darboux transformation to numerically construct higher-order solutions from superpositions of elementary AB solutions (for intensities > 9) [204]. For the AB solution, the temporal period $\delta\tau$ and the intensity peak are calculated from Eq. 4.4 and 4.5 for a range of modulation frequencies varies from $a = 0.001$ to $a = 0.449$. Whilst for the higher-order SFB solutions, only one of the constituent elementary AB is varied from $a = 0.001$ to $a = 0.449$ and the other(s) are set to $a = 0.449$. It is important to note that this particular way of constructing the theoretical curve (the red curve in Fig. 4.7) is crucial to allow the continuity of the curve from the elementary solutions to the higher-order solutions. Indeed, the first-order rational solution (PS) can only be considered as the superposition of two ABs of $a_1 \to 0.5$ and $a_2 \to 0$ (not as the superposition of $a_1 = 0.25$ and $a_2 = 0.25$, for example), and the second-order rational solution can be considered as the superposition of three ABs of $a_1 \to 0.5$, $a_2 \to 0.5$, and $a_3 \to 0$.

It is clear that the scattered points extracted from the chaotic MI field cluster closely around this calculated curve, providing additional confirmation that the analytic SFBs of the NLSE are

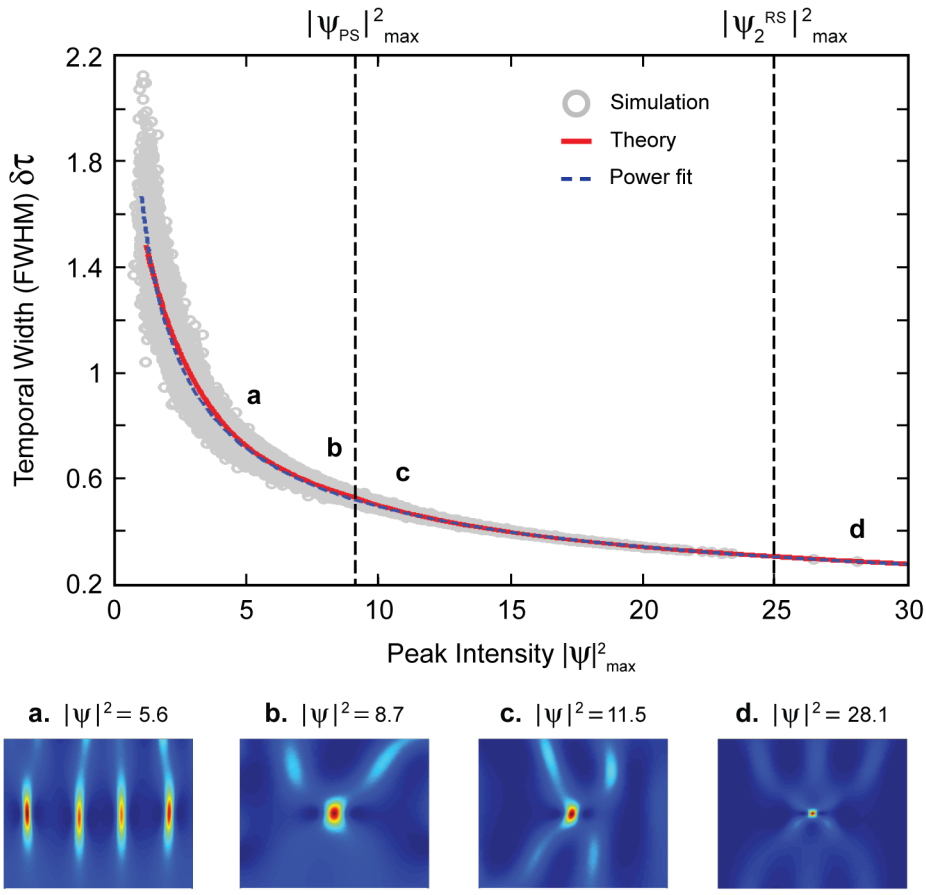

Figure 4.7: Scatter plot of temporal width (FWHM) against peak intensity for the 2853669 intensity peaks in the chaotic MI field from simulations (gray circles) compared with theoretical predictions for the properties of SFBs (red solid line). A comparison is also made with a power function of $\delta\tau_{\text{fit}} = 1.678/(|\psi|^2_{\text{max}})^{0.532}$ (blue dotted-dashed line). The peak intensities of the spontaneously emergent localised structures are obtained using specific peak detection over a full two-dimensional spatio-temporal computational window, and their corresponding temporal widths are calculated in the same way as the calculation done for the analytical SFB structures explained in Appendix A.2. In the bottom panel, we plot several examples of spatio-temporal structures of the spontaneously emerging breathers to highlight the nature of the breathers typically found around the region. These breathers correspond to the temporal intensity profiles plotted in Fig. 4.6(a,b,d,e).

indeed the appropriate framework to describe the emergent peaks in noise-induced MI. The scatter about the calculated curve is to be expected since the calculated higher-order solutions assume only one combination of constructing elementary breathers at each peak intensity (following the modulation frequency we just described above, and under the assumption of zero velocity and zero relative phase difference of constituent ABs for the higher-order solutions). For the elementary breather solutions, the observed scatter arises mainly from the fact that the spontaneously emergent breathers are in general not perfectly symmetric and not perfectly oriented perpendicular to the time τ-axs as in the case of the analytical solutions we consider here. As for the higher-order breathers, the observed scatter arises from different possibilities of elementary ABs combinations constructing the higher-order breathers (see Fig. 4.4 and Table 4.1 for some examples).

Additionally, we also compare this plot with a power fit function $\delta\tau_{\rm fit} = 1.678/(|\psi|^2_{\rm max})^{0.532}$ (blue dotted-dashed line). Although this curve cannot fit perfectly the theoretical curve of SFBs (very well fitted for higher-order breathers, but deviates slightly for the elementary breathers), we can see that this fit lies well in the middle of the scatter plot. It shows that the relation between the temporal width and the peak intensity of SFB solutions could be approximated roughly by a power function.

4.4 Temporal-spectral correlation

Fig. 4.7 shows clearly how higher intensity peaks are associated with shorter temporal durations. This suggests that the presence of higher-order solutions may also appear in the spectral domain through increased bandwidth. Although some suggestion of this can be seen from inspection of the temporal and spectral evolution in Fig. 4.5, we examine this relation quantitatively in Fig. 4.8 by plotting suitable measures of temporal and spectral width as a function of propagation distance. To characterize the temporal width of the evolving field, we calculate the intensity auto-correlation function: $g^{(2)}(\xi,\tau_{\rm ac}) = \left\langle |\psi(\xi,t)|^2 |\psi(\xi,t+\tau_{\rm ac})|^2 \right\rangle$ and compute the width (the FWHM) $\Delta\tau_{\rm ac}$ of the central coherence peak. This gives a measure of the average width of the localised temporal peaks in the noisy pulse train [210]. To determine a suitable measure of spectral width, we use the bandwidth $\Delta\omega_{\rm s}$ calculated at the -80 dB level in the wings of the spectrum.

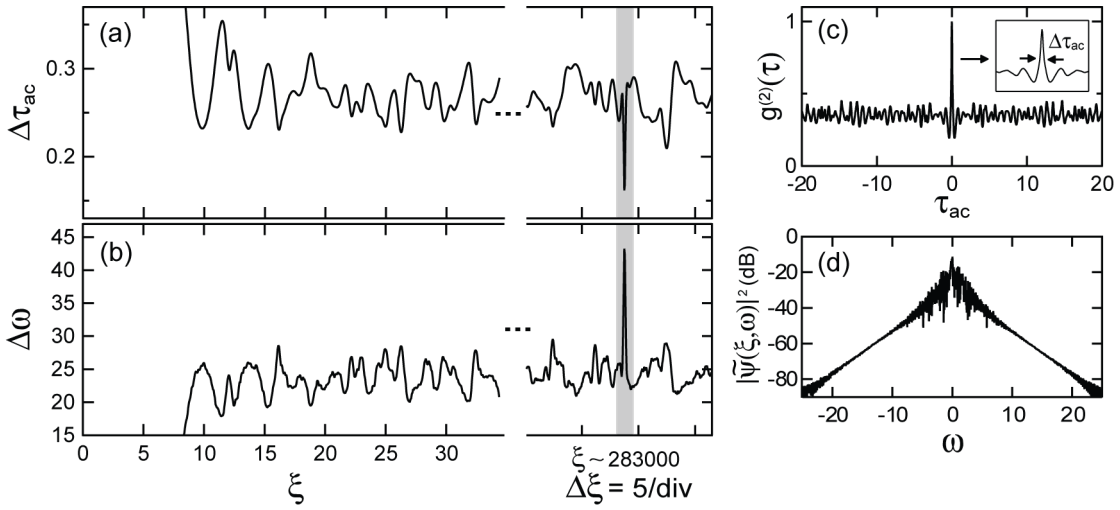

Figure 4.8: As a function of the propagation distance ξ, (a) and (b) plot the evolution of the width of the autocorrelation coherence peak and the -80 dB spectral width for the evolving MI field in Fig. 4.5. These results illustrate how spectral expansion is associated with the appearance of shorter temporal structures in the random AB pulse train. (c) and (d) show the autocorrelation and spectrum for the highest intensity peak associated with the collision between three breathers. The detail in (c) shows how the FWHM of the central autocorrelation coherence peak is determined.

Figs 4.8(a) and (b) respectively plot the evolution of the width $\Delta\tau_{\rm ac}$ of the central coherence peak and the bandwidth $\Delta\omega$ as a function of distance ξ. Although both the temporal and spectral characteristics fluctuate significantly with propagation, we nonetheless can clearly see by inspection how larger spectral widths are associated with shorter autocorrelation coherence peaks and vice-versa. We highlight in particular (using shading) the point at which the structure with shortest

temporal width and largest bandwidth emerges corresponding to the collision of 3 elementary breathers. At this distance, we also explicitly plot in Figs 4.8(c) and (d) the autocorrelation and spectrum, with the inset in the autocorrelation function showing detail of the coherence peak. Note that the -80 dB criterion chosen here is arbitrary and similar characteristics are observed for spectral width at e.g. -60 dB or -40 dB. Yet, we found that plotting the evolution of the spectral width at -80 dB allows for a better discrimination between the localisation characteristics of the various emerging coherent structures.

The evolution of the spectral width plotted in Fig. 4.8(b) can also give us a qualitative understanding of the behaviour of the system along the propagation. Comparing it to Fig. 4.5, we can see that the initial broadening of the spectrum corresponds to the initial compression in time domain that forms semi-periodic train of pulses at distance $\xi \approx 10$. This nonlinear amplification due to the MI then decays back close to its initial condition, which corresponds to the narrowing back of the spectrum, showing a trace of the FPU recurrence. Further propagation, however, is quickly turned into a more chaotic spatio-temporal evolution, shown by the random fluctuation of the spectral width [211].

4.5 Statistical analysis

In the previous section, we have seen that higher order breathers lead to higher intensity peaks and larger spectral widths. Understanding their significance to the physics of rogue waves however, requires an analysis of the associated statistics [7]. In this section, we present the statistical distribution and the rogue wave analysis of both the spatio-temporal and temporal dynamics (taken at a fixed distance) of the chaotic MI field governed by the NLSE. For each case, the statistical analysis is performed on the intensity (the relevant quantity in optics) and the amplitude (the relevant quantity in oceanography) of the MI field.

4.5.1 Spatio-temporal dynamics

Intensity

We plot in Fig.4.9(a) the histogram (in terms of the probability density) of the peak intensities of breathers structures detected in the spatio-temporal MI field, corresponding to the peak intensities used to plot the scatter plot shown in Fig. 4.7. The histogram shows an extremum at $|\psi|^2_{\max} \approx 5$ after which the tail of the distribution decays exponentially (linearly on the semi-logarithmic scale used in the figure).

It is important to mention that although the extremum of this histogram is shifted away from the AB intensity at maximum gain $|\psi|^2_{\max} \approx 5.8$ (see Fig. 4.2(b) and the discussion that follows), the calculated average peak intensity of the distribution (≈ 5.7) is in fact quite close to this value. A closer look at the evolution of the chaotic field shows that although most of the localised structures in the initial phase of the propagation are close to an AB structure with $a = 0.25$, further propagation transforms this semi-periodic structures into a chaotic field, accompanied by splitting and recombination (collision) of breathers (see Fig. 4.5(a)). Consequently, the distribution of peaks intensity that is initially centered at ≈ 5.6 is broadened by the generation of peaks with higher

intensities due to collision, accompanied by the generation of more peaks with lower intensities due to splitting.

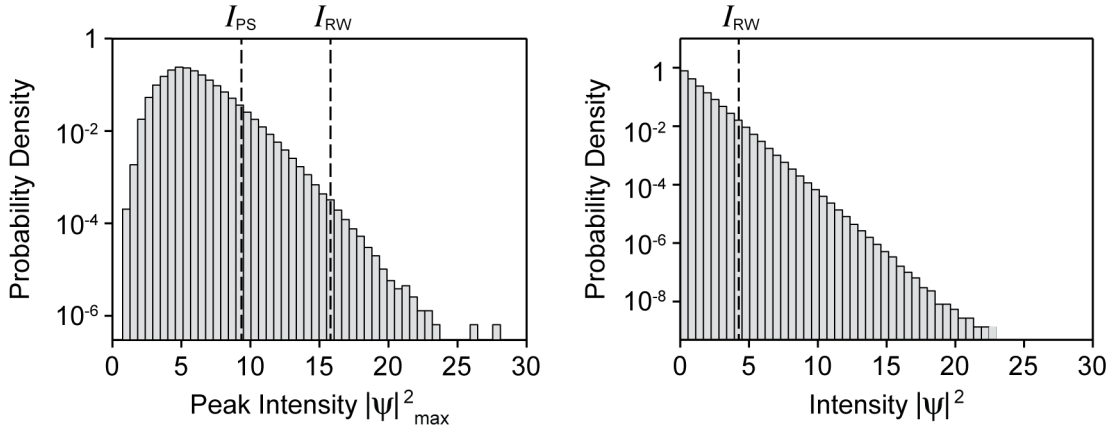

Figure 4.9: (a) Peak intensity statistics of the localised structures. (b) Distribution over the complete field intensity of the two-dimensional spatio-temporal computational window. The dashed lines indicate the Peregrine soliton threshold I_{PS} $\left(|\psi_{\mathrm{PS}}|^2_{\mathrm{max}}\right)$ and the rogue intensity threshold I_{RW}. Both distributions are plotted on semi-logarithmic scale.

On the interest of rogue wave study, we adapt the criterion commonly used in hydrodynamics to define rogue waves by introducing a *rogue wave intensity* threshold $I_{\mathrm{RW}} = 2\,I_{\mathrm{S}}$, with I_{S} defined as the "significant intensity" (the mean of the highest third of peaks). In this way, any localised structure with peak intensity $|\psi|^2_{\mathrm{max}} \geq I_{\mathrm{RW}}$ is considered as a candidate for a "rogue" event. For our simulation results, the rogue wave intensity $I_{\mathrm{RW}} \approx 15.8$ is indicated by the vertical line in the histogram plot of Fig. 4.9(a). Based on this criterion, only 0.04 % of the peaks in the ensemble have intensities exceeding this value.

Significantly, comparing this threshold with the the peak intensity of the PS ($|\psi_{\mathrm{PS}}|^2_{\mathrm{max}} = 9$), as the boundary between elementary and higher-order SFB solutions, we can see that it is only the structures arising from collisions of elementary breathers that satisfy the definition of rogue wave events. These results also show that Peregrine soliton is not, in this approach, statistically rare enough to be associated with rogue waves. Additionally, the percentage of rogue wave events we have here (0.04 %) is even significantly lower than the percentage of the total higher-order solutions which is about 6.2 % of the total intensity peaks, showing that these peaks can clearly be described as rare rogue wave events.

As well as taking the distribution of the peak intensity as we have just seen [7, 33, 155], the study of optical rogue waves is also often based on the distribution of the field intensity itself [35, 77, 146, 212]. For completeness, we plot in Fig. 4.9(b) the distribution taken over the complete field intensity of the two-dimensional spatio-temporal computational window shown in Fig. 4.5. In contrast to the distribution of peak intensity, the distribution we have here does not exhibit any extremum point. Instead, it follows an exponential statistics, showing higher population for lower intensity field, with the maximum at zero. In this case, the rogue wave threshold calculated under the same criterion used earlier yields $I_{\mathrm{RW}} \approx 4.3$, where about 1.54 % of the field intensity points exceeding this value. The large amount of events identified as rogue waves shows that the criteria $I_{\mathrm{RW}} = 2\,I_{\mathrm{S}}$ is only suitable to be applied on the statistics of peak intensity.

Additionally, notice also that the exponential distribution of the field intensity also shows that although the initial background intensity of the field is 1, the observable background intensity in the regime of chaotic MI field is actually closer to zero. From inspection of the density map plotted in Fig. 4.5(a), we can see that the uniform blue colour in the initial stage of $\xi < 10$ is transformed into darker blue background in the expense of breather emergence.

Amplitude

A similar analysis can also be performed in terms of the amplitude of the field (the envelope height) $A = |\psi|$, which is one of the quantities of interest in hydrodynamics [213]. To this end, we plot in Fig. 4.10(a) and (b) the distribution of the peak amplitude $|\psi|_{\max}$ and the field amplitude $|\psi|$ respectively. For a comparison with the intensity statistics presented above, we introduce here a *rogue wave amplitude* threshold $A_{\mathrm{RW}} = 2\,A_{\mathrm{S}}$, where A_{S} is the "significant amplitude" defined as the mean of the highest third of the population. In the case of peak amplitude, the calculated $A_{\mathrm{RW}} \approx 5.6$, while in the case of field amplitude, the calculated $A_{\mathrm{RW}} \approx 2.85$. These rogue wave thresholds are indictaed by vertical dashed lines in the corresponding histograms.

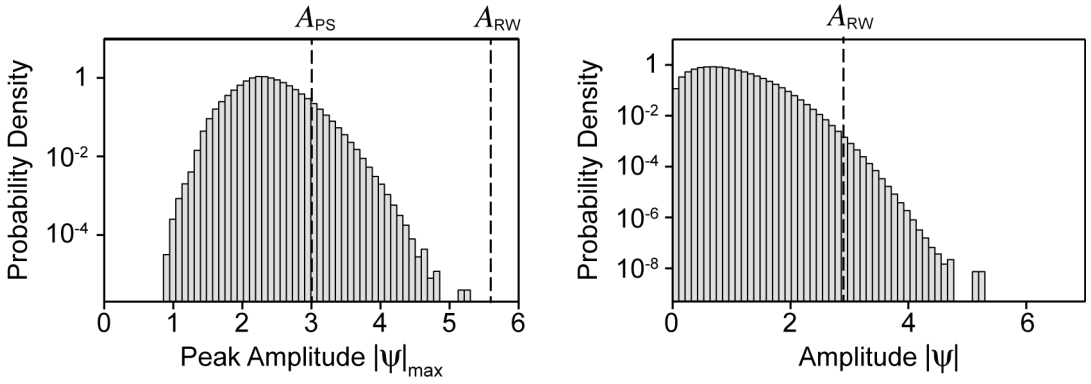

Figure 4.10: (a) Peak amplitude statistics obtained using the same peak detection method as used in Fig. 4.9. (a) Distribution over the complete field amplitude of the two-dimensional spatio-temporal computational window. The dashed lines indicate the Peregrine soliton threshold A_{PS} ($|\psi_{\mathrm{PS}}|_{\max}$) and the rogue amplitude threshold A_{RW}. Both distributions are plotted on semi-logarithmic scale.

Interestingly, we found from the peak amplitude distribution shown in Fig. 4.10(a) that even the highest amplitude breathers from our ensemble are not identified as rogue waves in this approach. Whilst applying this criterion on the field amplitude yields 0.03 % of rogue wave events. It is important to remember, however, that the terminology "field" we use here refers to the wave envelope and not the modulated wave carrier itself, thus the analysis performed here should still be adapted to the more commonly used quantity such as the wave height, in their comparison to the study of ocean wave statistics as shown for example in Ref. [213].

4.5.2 Temporal dynamics at fixed distance

The statistical analysis we have discussed above is performed over the two-dimensional spatio-temporal field, which is a suitable approach considering the double localisation property of rogue waves. The space-time measurement of the wave under study however is often still a challenge.

In oceanography, reliable measurement data is obtained from in situ instrumentation techniques measuring only the temporal dynamics of the ocean wave [15, 45]. In fibre optics, it is only the temporal dynamics of a fully random optical field that can be measured at the end of a fibre. Indeed, although the spatial evolution of optical pulses can be acquired by cut-back method, this approach is only applicable if the modulation instability is triggered by coherent seed, which is not the case in the study of spontaneous modulation instability, or if we want to characterize evolution in a statistical sense. Studies on temporal evolution and statistical analysis of chaotic MI field are therefore needed in order to provide relevant comparisons with measurement data.

For this purpose, we performed a similar simulation as earlier (MI in the NLSE simulation with a noise-perturbed plane wave) but with a much larger temporal window extending to $\tau_{\max} = \pm 72792$ (using 2^{21} τ -points) in order to have sufficient data for statistical analysis. We analyse the dynamics of the intensity envelope (Fig. 4.11(a)) and the modulated carrier wave under the envelope (Fig. 4.12(a)), taken from the temporal cross section at distance $\xi = 250$ (in the regime of chaotic MI field).

Intensity envelope (for fibre optics)

Statistical analysis on the temporal dynamics of light propagating in fibre optical system can be performed in the same way as earlier, by taking the statistics of the intensity fluctuations [78, 93, 152, 214] and the statistics of the intensity peaks [26, 90, 145, 215]. The comparison between these two approaches is shown in Fig. 4.11(b) and (c) respectively. For each case, the distribution taken from the spatio-temporal intensity field is also plotted in blue dashed line.

We notice first that while the statistics of the temporal field intensity follows closely the exponential statistics of the spatio-temporal field intensity, a significant difference is observed for the statistics of the peak intensity. Although the profile of the distributions is similar, the temporal peak intensity populations are much lower compared to the spatio-temporal peak intensity populations, leads to the compression of the distribution profile towards lower value. Specifically, we can see that the distribution of the temporal peak intensity shows an extremum point at $|\psi|^2_{\max} \approx 2$ (instead of at $|\psi|^2_{\max} \approx 5.6$) after which the tail decays exponentially, with the maximum intensity obtained from the ensemble is only $\approx$ 13.5. These significantly lower values can be expected because the temporal evolution of the chaotic MI field samples the breather structures at random positions along z instead of at the peak of each localised structure.

Applying the same criteria as earlier, the rogue wave intensity I_{RW} is calculated to be ≈ 9.1 with $\approx 0.26\,\%$ of the temporal intensity peaks exceeding this value. Note that although the rogue wave threshold here is just slightly higher than the peak intensity of PS $|\psi_{\mathrm{PS}}|^2_{\max}$, this does not mean that almost all of the higher-order breathers are categorised as rogue waves. Indeed, the temporal peak intensity $|\psi|^2_{\max} < 9$ is populated not only by the elementary breathers but also by the higher order breathers. However, we remark that the significantly higher percentage of rogue wave events calculated here suggests caution to the implementation of I_{RW} criteria that is defined as twice the "significant intensity" (the mean of the highest third of peaks) in fibre optics experiment.

In comparison with optical rogue wave experiment, it is important to note that most observations of rogue waves in optics to this date were made in the supercontinuum regime

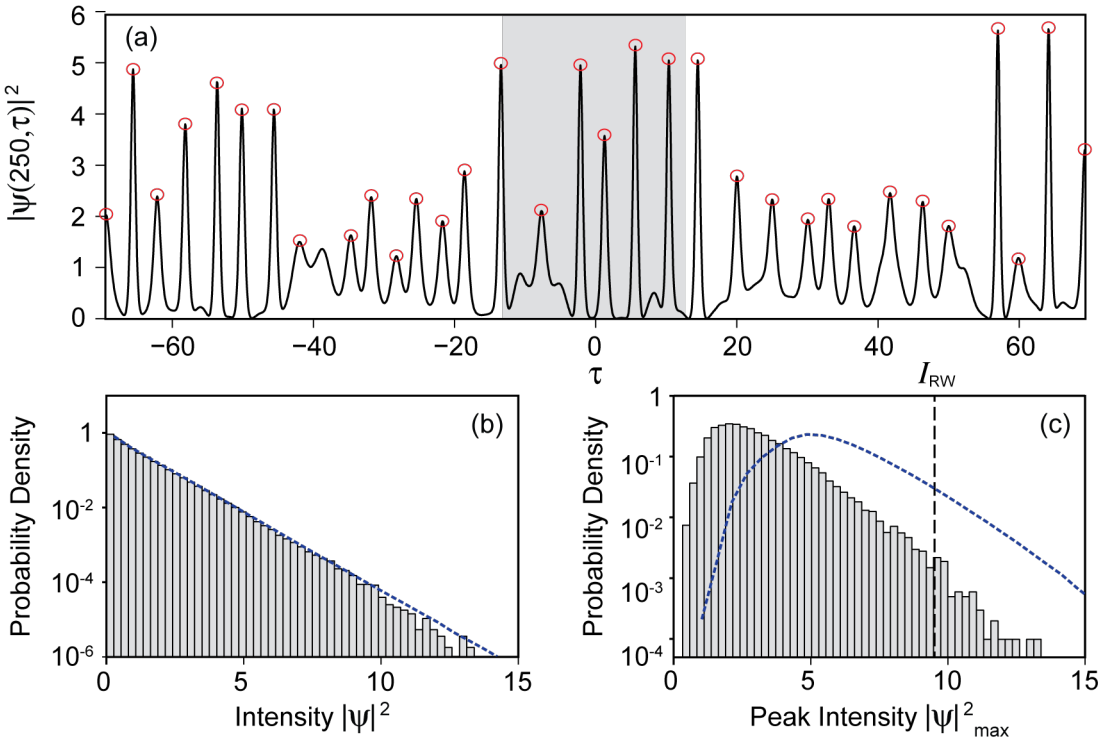

Figure 4.11: Statistical analysis of temporal dynamics of intensity envelope taken at distance $\xi = 250$ of simulated MI chaotic field. (a) Plots a small section of the intensity envelope fluctuation, with the distributions plotted in (b) taken over the whole intensity fluctuation and (c) taken only from the temporal intensity peaks (37385 temporal peaks are detected by applying relative minimum threshold of 0.4). The black dashed line indicates the rogue intensity threshold I_{RW}. For a comparison, dotted blue dashed curve plots the distributions of the spatio-temporal field intensity and peak intensity shown in Fig. 4.9.

instead of in the regime of SFB dynamics. Although these supercontinuum were generated from long pulses [26, 142] or even continuous wave pumping [143, 145, 216], it is important to remember that the higher-order effects beyond the basic NLSE played an important role in this regime. Therefore, the statistics presented here, are not to be compared with those obtained from the supercontinuum. Moreover, although approximate SFB solutions can exist even under these conditions [217], the observed rogue wave characteristics in this regime arose instead from the dynamics of background-free hyperbolic secant solitons, where the rogue waves emergence are due to the Raman shifted collision of the sech solitons instead of the breathers.

Carrier wave (for ocean wave)

The results we have discussed so far are focussed on the envelope evolution of wave propagation governed by the NLSE. The statistical analysis of the wave crest or the wave height in the study of oceanic rogue waves, however, are taken from the modulated surface wave and not from the envelope. To this end, we extract the modulated (carrier) wave of the temporal field shown in Fig. 4.11(a) by multiplying the complex envelope $|\psi|$ with a sinusoidal carrier wave of frequency ω. In this way, the phase information of the envelope is included in the construction of the modulated carrier wave. We plot in Fig. 4.12(a) a small part of this modulated wave, which corresponds to the gray shaded area in Fig. 4.11(a). Note that since the numerical simulations of the NLSE

performed here was originally performed using fibre optical parameters (before being normalised), the frequency of the modulated carrier waves is scaled down 100 times, in order to obtain the typical value found in deep water wave (≈ 3 wave cycles under a PS envelope).

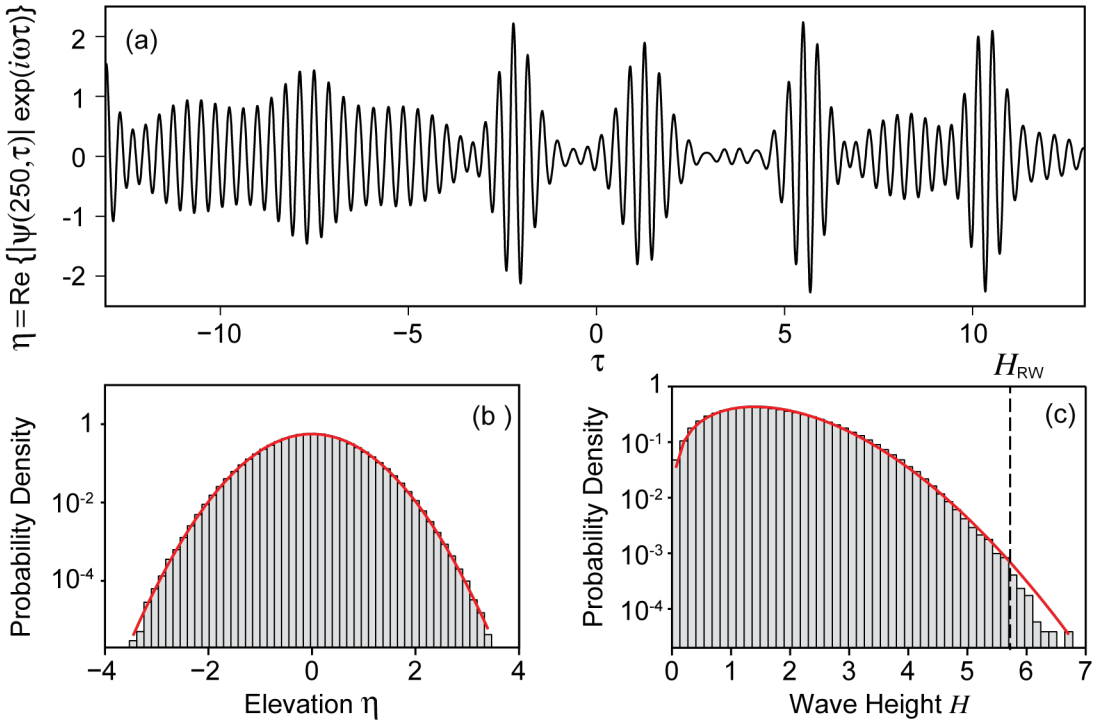

Figure 4.12: Statistical analysis of temporal dynamics of modulated carrier wave taken at distance $\xi = 250$ of simulated MI chaotic field. (a) Plots a small section of the modulated carrier wave (extracted from the intensity envelope that is highlighted in gray shaded area in Fig. 4.11(a)). (b) Plots the distributions of the wave fluctuation (corresponding to surface elevation of an ocean wave), and (c) plots the distribution of the wave height. The red solid lines plot the Gaussian and Rayleigh fit of the distributions. The black dashed line indicates the rogue wave height threshold H_{RW}.

The statistics of the wave elevation η and the trough-to-crest wave height H of this modulated wave are shown in Fig. 4.12(b) and (c) respectively. We compare these distributions with Gaussian distribution for the wave elevation and Rayleigh distribution for the wave height (see Section 2.2) and we found that the distributions are very well-fitted in both cases. The Gaussian fit curve (red solid line in Fig. 4.12(b)) follows the function $1/(\sqrt{2\pi}\sigma)\,\exp(-\eta^2/(2\sigma^2))$ with $\sigma = 0.7$, with the coefficient of determination $R^2 = 0.9994$. Whilst the Rayleigh fit curve (red solid line in Fig. 4.12(c)) follows the function $H/\sigma^2\,\exp(-H^2/(2\sigma^2))$ with $\sigma = 1.4$, with the coefficient of determination $R^2 = 0.9984$.

Significantly, these results in fact question the role of the third-order nonlinearity on the deviation of the statistics from the Gaussianity observed in the ocean waves, as has been suggested by many authors [98, 121, 218]. The results here suggest that in the steady state regime of a chaotic MI field, the third-order nonlinearity (at least for the propagation of one-dimensional wave) is not sufficient to modify the standard linear Gaussian statistics measured at a fixed point.

Using the standard criterion of rogue wave height $H_{\mathrm{RW}} = 2\,H_{\mathrm{S}}$, with the significant wave height H_{S} defined as the mean of the largest one third of wave heights, H_{RW} is found to be ≈ 5.7, where 0.015 % of the wave heights exceeding this value. Following the same argument as before,

the lower value of the rogue wave height threshold H_{RW} from the wave height of PS at the peak amplitude $H_{\mathrm{PS}} = 2\,|\psi_{\mathrm{PS}}|_{\max} = 6$, does not necessarily imply that the rogue waves identified here include the elementary breather structures. Instead, the off-centered breather structures captured in the temporal fluctuations of the spatio-temporally chaotic MI field in fact show that these rogue waves are more probably to be those from the higher-order breathers.

Furthermore, although the frequency of the sinusoidal carrier wave used here is much lower than the one for optical wave, we verified by the simulation that the same Gaussian and Rayleigh function are still obtained even when we use the frequency of the optical wave (100 times larger than the one plotted in Fig. 4.12(a)). In this case, the tail of the histogram follows even closer the tail of the Gaussian and Rayleigh fit function shown in Fig. 4.12(b) and (c), yielding slight increase on the percentage of rogue waves (waves with height $H > H_{\mathrm{RW}}$). On the contrary, we found that the tails of the fit functions do depend on the frequency of the carrier wave being used when the number of cycles below the envelope is significantly lower. Indeed, while higher number of cycles under envelope enables the extreme dynamics of the envelope to be followed by the carrier wave, the opposite signifies that only the slow dynamics of the envelope (thus low amplitude) can be detected.

4.6 Conclusions

We extend the previous studies in spontaneous modulation instability in various aspects. We first study the properties of spontaneously emergent coherent localised structures in a chaotic MI field over a large range of intensities. We show that the localised structures with intensity lower than the intensity of PS can well be described by the analytical elementary breather (SFB) solutions, while those with higher intensity can well be described by the higher-order breather (SFB) solutions in terms of collisions of ABs.

Significantly, we show that these breather solutions can be characterised by their specific peak intensity and temporal width, where plotting the relation between these two quantities provides an effective way to have a global comparison between the spontaneously emegent breather structures and the analytic prediction. The observed clustering of these characteristic quantities about the expected analytic prediction confirm that the analytic SFB solutions of the NLSE indeed provide a natural basis for interpreting rogue wave emergence in spontaneous MI.

Several properties characterising the evolution of the spontaneous MI field along the propagation are also investigated in this chapter. We first show that the emergence of higher-order breathers at certain distance in the spatio-temporal MI field can be detected from the width of the autocorrelation coherence peak and the width of the spectrum, where the two quantities are correlated. The emergence of an extreme higher-order breather therefore yields an extremely narrow width of autrocorrelation coherence peak and an extremely wide spectral width. We then also show that the evolution of the pump power along the propagation (providing the temporal window under study is sufficiently large) can provide a means to characterise the steady state regime of a spontaneous MI field.

We have also performed a significant amount of statistical analysis taken from the spatio-temporal and temporal dynamics of the chaotic MI field governed by the NLSE. Due to

the universality of this equation, the statistical analysis performed here is focussed not only on the intensity but also on the amplitude of the MI field, in order to facilitate the study in both optics and hydrodynamics, or in other physical systems governed by the NLSE.

Firstly, we highlight that our analysis of the statistical properties of the peak intensities shows that the Peregrine soliton is not statistically rare enough to be considered as a rogue wave in systems governed by the NLSE. Rather, our results confirm that the highest intensity NLSE rogue waves are most appropriately identified as collisions between elementary SFB solutions. In this regard, however, we remark that the association of the Peregrine soliton as a rogue wave prototype was initially made on qualitative grounds, simply noting that it is the highest intensity single-breather solution of the NLSE which is localised in both space and time [172, 174]. Subsequent studies of the Peregrine soliton as a rogue wave have focussed similarly on its intensity characteristics and its growth and decay, and not on its statistical rarity (see e.g. Ref. [137]). Based on our results, however, it appears that it is inappropriate to consider the Peregrine soliton as a statistical rogue wave, although it will certainly appear as a wave of intensity exceeding the mean in the associated probability distribution.

Secondly, we show the significant difference on the peak intensity statistics depending on whether it is obtained from the full two-dimensional spatio-temporal field or only over the time series taken at a fixed distance. For a meaningful comparison, the distance we use here is taken within the fully chaotic regime of the spontaneous MI field. The two statistics appear to share the same characteristics, but the temporal statistics shows lower intensity compared to the spatio-temporal statistics, where the distribution extremum located around 2 instead of 5.6. These results complement the same suggestion that had been made earlier, for example in the case of supercontinuum rogue solitons [6, 102] or ocean waves [51].

We also investigate the statistics of the carrier wave modulated by the envelope ψ governed by the NLSE. Significantly, we show that the statistics of the wave elevation taken at a distance within the chaotic regime of spontaneous MI field exhibits Gaussian distribution, while the statistics of the wave height exhibits Rayleigh distribution. These results therefore question the role of the third-order nonlinearity on increasing the probability of rogue wave occurrence.

Finally, we note the importance of developing techniques that allow accurate measurement of the spontaneous MI field in real time. In optics, this real-time measurement is still a challenge due to the fast random dynamics of the MI field. However, in the next chapter, we propose a technique that can be used to solve this problem. Also, the use of the dispersive Fourier transform method for real-time measurement of spectral fluctuations (see Chapter 5) has already represented a significant experimental advance [151, 219–221], and it is also possible that the strong temporal-spectral correlations that we have identified here may lead to sensitive real-time measurements of the wings of the MI spectrum that can provide evidence for collision events.

Additionally, we also note that techniques allowing measurement of space-time evolution of an MI field also need to be developed for further understanding and confirmation of this interesting phenomenon. A technique similar to the one shown in Ref. [222] might be applicable for this purpose.

Chapter 5

Real-time temporal measurement of spontaneous modulation instability

As discussed in the previous chapter, spontaneous modulation instability (MI) is an important phenomenon in the study of rogue waves in various areas of physics. In optics, this instability has been observed in different systems such as in optical fibre described by the NLSE, in spatial media with non-instantaneous nonlinearity [223, 224], in high power filamentation [225], and in discrete nonlinear arrays [226]. In optical fibre propagation, MI is known to yield a strong temporal modulation associated with the growth of spectral side bands [127, 162, 227].

Although fluctuations in the spectral properties when MI is generated from noise can be measured in real time using dispersive Fourier transform techniques [219, 220], the real-time temporal measurement of this phenomenon remains a challenge. A direct observation of noise-seeded MI temporal dynamics has never been realised experimentally due to the ultrafast non-repetitive (arbitrary) nature of the generated waveforms. We show here that this limitation can be overcome by the use an ultrafast time-lens magnifier system [8].

The concept of time-lens was first proposed as an extension of the well-known analogy between paraxial diffraction in space and chromatic dispersion in time [228]. It is the temporal equivalent of a thin lens, where instead of imparting a quadratic spatial phase on the propagating optical wave, a time-lens imparts a quadratic temporal phase on the waveform [8, 229–231]. Therefore, similar to the use of thin lens, a time-lens can be used to perform various optical processing tasks, such as imaging, magnification, Fourier transform, etc., which allows all-optical signal processing in the time domain to be realised in an effective way [8, 232, 233].

The application of the time-lens approach is of particular importance in the development of ultrafast fibre technology. Specifically, ultrafast waveform generation, characterisation, and processing have been demonstrated by the combination of time-lens and dispersion through various techniques, such as pulse compression [234, 235], temporal magnification (time-stretching) [236–238], time-to-frequency conversion [239, 240], spectral magnification [241], time-to-space conversion [242–244], and temporal cloaking [245, 246].

In this chapter, we explore the use of a time-lens to perform real-time measurements of spontaneously emerging breather structures measured at the output of an optical fibre. This is in

fact an experimental realisation of the theoretical study performed in the previous chapter (Chapter 2). In particular, the generation of the spontaneous MI from a narrowband continuous wave (CW) background field shown here allows a direct comparison with the theoretical analysis presented earlier. Moreover, similar statistical analysis as shown in Section 4.5.2 can also be performed conveniently due to the the ultrafast dynamics of the system (allowing large amount of data acquired in a very short time). Note that whilst participating in the set up and testing of the time lens experiment was performed as part of this thesis, the data sets that are presented here are from experiments performed by Dr C. Billet (FEMTO-ST), Mr M. Närhi (Tampere University of Technology) and Dr B. Wetzel (University of Québec), who have kindly given permission for these results to be included. Note that the work analysing and interpreting these experimental results do form an integral component of this thesis.

In what follows, a brief review on space-time duality is first given, focussing on the duality between diffraction and dispersion, thin lens and time-lens, and their combination in forming spatial and temporal imaging. This discussion focusses on presenting the physical concept of temporal magnification in the limit of large magnification, which is the regime we consider here to measure the ultrafast temporal dynamics of the spontaneous MI structures. It is then followed by a discussion of the experimental generation of spontaneous MI on a CW field in Section 5.2, and the working principle of the real-time temporal characterisation by a time-lens in Section 5.3. Finally, the measured time series of the MI field intensity envelope and their statistical analysis are presented in Section 5.4. The spontaneously emergent breather profiles measured from the experiments are also shown to be in good agreement with analytical predictions.

5.1 Space-time duality

Paraxial diffraction and narrowband dispersion

The analogy between diffraction of an electromagnetic beam and dispersion of an electromagnetic pulse (or modulated wave) has been known for many years, and is based on the mathematical equivalence of the propagation equation expressing both phenomena [228, 247–250]. In the case of diffraction, the frequency spectrum of the wave is assumed to be monochromatic and the evolution of the spatial envelope profile of the wave is assumed to vary slowly on the scale of a wavelength (narrowband spatial frequency) along the propagation direction z. Whilst in the case of dispersion, the spatial profile of the wave is assumed to be a plane wave and the evolution of the envelope wave is assumed to vary slowly in time on the scale of an optical cycle (narrowband temporal frequency) along the propagation direction z.

In paraxial diffraction, the electric field of the monochromatic beam can be written as $\mathbf{E}(x,y,z,t) = E(x,y,z)\exp\left[i\left(\omega_0 t - kz\right)\right]$, where $E(x,y,z)$ is a slowly varying envelope function of the transverse beam profile. A direct comparison with dispersion can easily be done by considering one-dimensional diffraction. It can be shown that the propagation of this spatial envelope profile is governed by

$$\frac{\partial E}{\partial z} = \frac{i}{2k}\frac{\partial^2 E}{\partial x^2}.$$

where k is the wave number of the propagating wave. Solving this equation in the transverse spatial frequency domain, one obtains

$$\widetilde{E}\left(k_x, z\right) = \widetilde{E}\left(k_x, 0\right) \exp\left(\frac{ik_x^2 z}{2k}\right), \tag{5.1}$$

This shows that diffraction can be seen as a result of a quadratic phase shift being imparted on the transverse k-vector upon propagation.

In narrowband dispersion, the electric field of the plane wave can be written as $\mathbf{E}(x, y, z, t) = A(z, t) \exp\left[i\left(\omega_0 t - \beta_0 z\right)\right]$, where $A(z, t)$ is a slowly varying envelope function of the travelling wave and β_0 is the wave number obtained from the expansion of the propagation constant $\beta(\omega)$ expressed in Eq. 2.19. It can be shown that the propagation of the wave envelope is governed by

$$\frac{\partial A}{\partial z} = \frac{i\beta_2}{2}\frac{\partial^2 A}{\partial T^2},$$

where β_2 is the group velocity dispersion (GVD) and $T = t - z/v_g$ is the retarded time, following the same formalism as in Section 2.4.2. Solving this equation in frequency domain, one obtains

$$\widetilde{A}\left(\Omega, z\right) = \widetilde{A}\left(\Omega, 0\right) \exp\left(\frac{-i\Omega^2\beta_2 z}{2}\right), \tag{5.2}$$

where $\Omega = \omega - \omega_0$ is the baseband angular frequency. This shows that dispersion can be seen as a result of quadratic phase shift being imparted on the angular spectrum of the pulse envelope upon propagation.

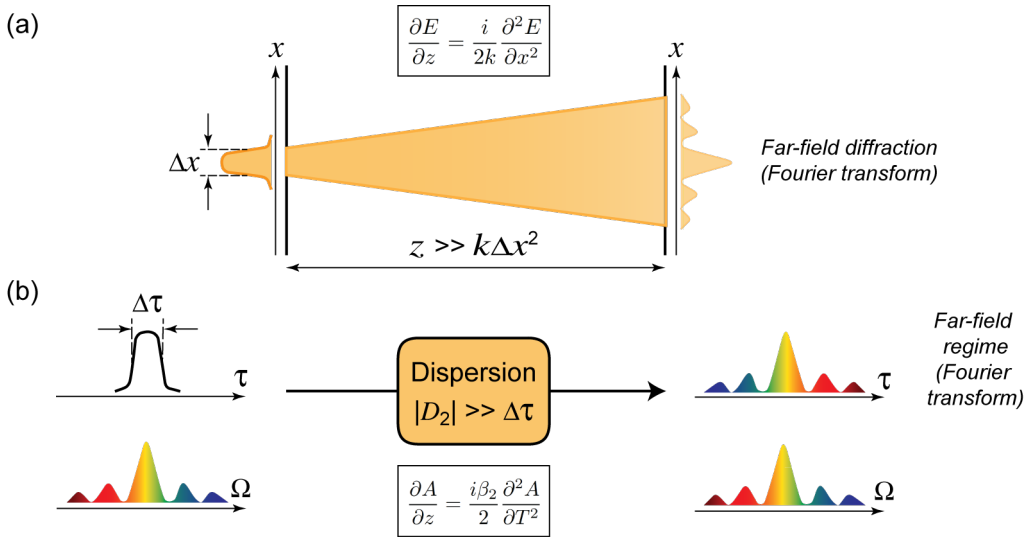

Figure 5.1: The space-time duality of diffraction and dispersion in the far-field regime. (a) Describes diffraction of a monochromatic beam resulting in the broadening of the beam profile. (b) Describes dispersion of a light pulse resulting in frequency chirp that broadens the pulse. In both cases, the far-field propagation leads to the Fourier transform of the input waveform (frequency-to-time conversion process). Adapted from Ref. [8].

Comparing Eq. 5.1 and 5.2, we can see that the scaled propagation distance z/k for diffraction is analogous to the product of the GVD parameter and the propagation distance $\beta_2 z$, which is called

the total group delay dispersion (GDD) D_2. This equivalence of the mathematical expressions shows that indeed diffraction in spatial imaging can be replaced by dispersion in temporal imaging (see Fig. 5.1a).

In analogy to the spatial Fourier transform observed in the far-field diffraction regime of a spatial light distribution, the intensity of a temporal field therefore evolves into its Fourier transform after sufficient propagation in a linear dispersive medium, yielding the mapping of the spectrum of the pulse into the waveform [251]. Considering the dispersion of a waveform of temporal width $\Delta\tau$, the condition of the far-field dispersion regime is $|D_2| \gg \Delta\tau$. This condition is in analogy to the spatial counterpart condition $z \gg k\Delta x^2$, where Δx is the width of the beam profile (Fig. 5.1b). As we shall see in the next chapter, this property can be used for real-time spectral measurement of ultrafast pulses, and can be realised simply by using a single-mode optical fibre [219].

Thin lens and time-lens

Contrary to the effect of diffraction, a thin lens is known to impart a quadratic phase shift directly to the spatial transverse parameter x, y of the input electric field [191]. In one-dimension, it is described as

$$\phi(x) = -\frac{kx^2}{2f},$$

where f is the focal length of the lens. The analogous time-lens can therefore be realised by imparting a quadratic phase shift to the local time variable T of the input waveform

$$\phi(T) = \frac{T^2}{2D_f}, \tag{5.3}$$

where D_f is the focal GDD of the time-lens.

Spatial and temporal imaging

Similarly, a temporal imaging system can be developed in analogy to the spatial imaging system. It generates a scaled replica of the input waveform at the output of the system, which allows temporal magnification (stretching) or compression of the waveform. Based on the space-time duality established above, temporal imaging can therefore be obtained by the combination of a time-lens with a suitable dispersive path preceding and following the time-lens [229, 230]. As shown in Fig. 5.2(a), a temporal image is formed when input waveform $A_{\text{in}}(\tau)$ is propagated consecutively through an input GDD D_{in}, a time-lens with focal GDD D_f, and an output GDD D_{out}, such that the imaging condition

$$\frac{1}{D_{\text{in}}} + \frac{1}{D_{\text{out}}} = \frac{1}{D_f} \tag{5.4}$$

is satisfied. Similar to spatial imaging, the magnification factor of temporal imaging is given by the ratio between the the output and the input GDD

$$M = -\frac{D_{\text{out}}}{D_{\text{in}}}. \tag{5.5}$$

The complete derivation of Eq. 5.4 and 5.5 can be found in Ref. [230]

(a) The analogy of spatial and temporal imaging (magnification)

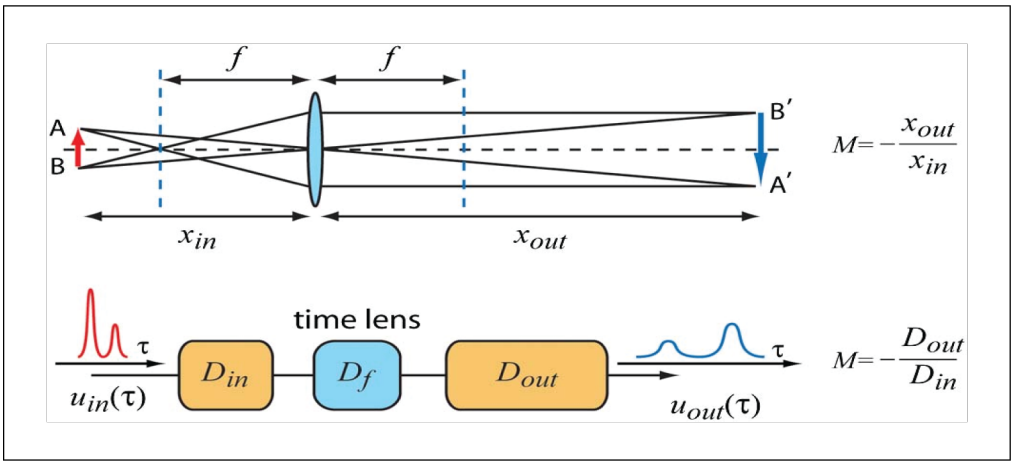

(b) In the limit of large magnification factor

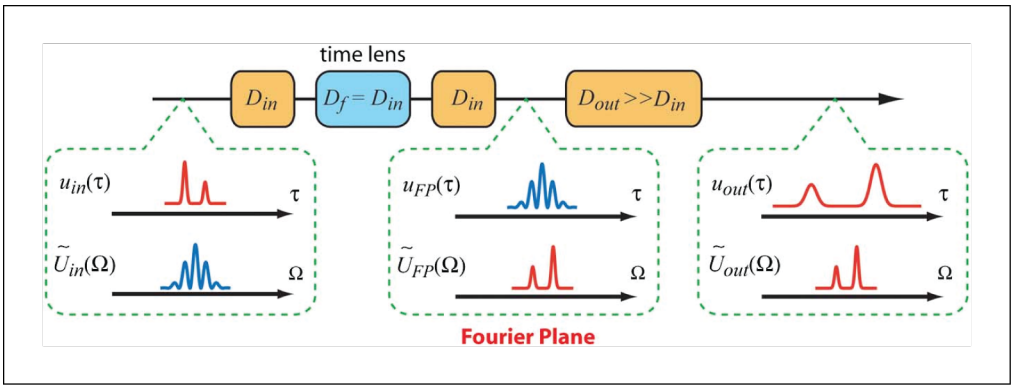

Figure 5.2: (a) The analogy between spatial and temporal imaging. A spatial magnification is realised by cascading input diffraction, lens, and output diffraction. Whilst a temporal magnification is realised by cascading input dispersion, time-lens, and output dispersion. (b) Spatial and temporal magnification in the limit of large magnification. The system can be seen to be constructed by a $2f$ Fourier processor time-to-frequency conversion realised by a temporal $2f$ Fourier processor, followed by a far-field frequency-to-time conversion. Here u_{in}, u_{FP}, and u_{out} denote the input, Fourier plane, and output electric field respectively, and $\tilde{U}_{in}$, $\tilde{U}_{FP}$, and $\tilde{U}_{out}$ denote the corresponding Fourier transform. *Source:* from Ref. [8].

From Eqs. 5.4 and 5.5, we can see that large magnification can be achieved when $D_{\text{out}} \gg D_{\text{in}}$ and $D_{\text{in}} \simeq D_f$. Indeed, this condition is similar to its spatial counterpart, where large spatial magnification can be achieved when object is located close to the focal length of the lens. This configuration can be viewed as $2f$ Fourier processor (analyzer) followed by a large dispersive path [237]. The waveform is first transformed from time-to-frequency by the $2f$ Fourier processor and subsequently transformed back to the temporal waveform by the large dispersive path, which results in the large temporal magnification of the waveform with factor $M = -D_{\text{out}}/D_{\text{in}}$ (see 5.2(b)).

5.2 Generation of spontaneous modulation instability on a continuous wave

In principle, modulation instability of continuous wave light can be generated through a simple propagation in a single-mode optical fibre, where the evolution of the field is governed by the NLSE (Eq. 2.21). The intensity dependent nonlinearity, anomalous dispersion, and low loss property of the fibre, allow a natural phase matching of the FWM process associated with the MI [127, 169].

However, due to the competition between the high power needed to observe the nonlinear effect and the low threshold power of stimulated Brillouin scattering (SBS) of silica, this process can not be realised straightforwardly [169]. Indeed, SBS in a single-mode optical fibre is known to cause backscattering of an incident light that limits the power that can be transmitted in the fibre [252, 253]. The backscattered light is frequency downshifted ($\approx$ 11 GHz, or $\approx$ 0.1 nm for 1550 nm light) and occurs when the power of the propagating light exceeds certain threshold. This threshold decreases with the increase of pulse width of the pump field (the decrease of the linewidth) due to the longer constructive interaction between the optical field and the generated density wave (the acoustic phonons) propagating in the fibre. Consequently, the SBS threshold is very low in a continuous wave or relatively wide pulses [162], and the study of MI in fibres are often realised by pulsed lasers (typically generated from mode locked lasers) [127, 254].

Experimental demonstration of MI on CW, however, can be realised under some situations. In 1989, the first experimental realisation was reported by Itoh by propagating a CW Nd: YAG laser of 1.319 μm (with broad spectral bandwidth) through a 5 km depressed-cladding silica fibre [255]. Following this work, other approaches have also been reported, such as the use of Fabry-Perot filter in the laser cavity to lower down the MI threshold power [256], the generation of MI in passive fibre cavities [257], and the use of CW Raman fibre laser as partially coherent source [258].

In the experiments reported here, we used a CW laser source generated from an external cavity laser (Agilent 81949A) centered at 1550.3 nm. This CW source was then phase-modulated using an electro-optic phase modulator driven by a $\sim$Gbit/s pseudo-random bit sequence of $\pm\pi$ phase swings (Textronix AWG7122C) for SBS suppression [259]. In order to have sufficient power for the generation of MI, this phase-modulated CW field was then amplified using an EDFA (Keopsys C40-PB) before injection in a single-mode fibre SMF-28 (with parameter $\beta_2 = -21.4\times10^{-27}$ s^2/m, $\beta_3 = 1.2\times10^{-41}$ s^3/m, $\gamma = 1.3\times10^{-3}$ W^{-1}/m, and linear loss of 0.18 dB/km). The input power of the CW field entering the fibre P_0 is 0.7 W. Here we characterised the output MI field after propagation in two different lengths of fibre: 11.7 km and 17.3 km. The schematic of this setup can be seen in Fig. 5.4(a).

For comparison with the experimental results, we also simulated the propagation of the noisy CW input field through these km-lengths of fibre. The input noise model used in our simulation includes the effects of the phase modulation and the amplified spontaneous emission (ASE) noise from the EDFA. For the latter, we used a -50 dB spectral background relative to the pump with random spectral phase, with the spectral background level obtained from experimental measurements using an optical spectrum analyser (OSA). The propagation of the CW field of $P_0 = 0.7$ W modified by this input noise was then simulated using the split-step Fourier method explained in Appendix B.3. For completeness, higher-order dispersion, inelastic Raman scattering and loss were included in the simulation [260].

Similar to what we have seen earlier in Chapter 4 (Fig. 4.5), the noisy CW field evolves into a chaotic MI field, starting from quasi-periodic breather structures emerging in the initial propagation, followed by a phase of random emergence of breathers. Measuring this MI field at a certain length along the fibre then gives us a temporal intensity fluctuation similar to the plot shown in Fig. 4.11(a). The typical temporal duration of these breathers obtained from the simulations is $2 - 5$ ps.

5.3 Real-time temporal measurement using time-lens

The ultrafast dynamics of the spontaneously emerging breathers generated in the system described above cannot be resolved by a direct measurement using real-time oscilloscope. The solution to overcome this problem is by temporally stretching the input waveform with a large magnification factor, which can be realised by the combination of dispersive paths and a time-lens. In this section, the experimental realisation of this concept is demonstrated using a four-wave mixing based time-lens.

5.3.1 Time-lens based on four-wave mixing

As discussed in Section 5.1, the function of a time-lens is essentially to impart a temporal quadratic phase to the input waveform. A straightforward approach to this problem is through a direct phase modulation using an electro-optic (EO) phase modulator driven with a quadratic voltage [261–266]. In practice, a sinusoidal modulating voltage can be used to provide a locally quadratic phase around its maxima and minima. However, the operation time window and the maximum phase shift that can be imparted to the input waveform of such a time-lens are limited and therefore is not suitable for ultrafast signal processing [232, 239].

A larger quadratic phase shift allowing temporal imaging with resolution down to subpicoseconds can be obtained from parametric processes, such as sum-frequency generation (SFG), difference-frequency generation (DFG), and four-wave mixing (FWM) [231, 240, 267–269]. This approach is based on an indirect phase modulation, where the temporal phase profile from the pump is imparted on the idler wave that is generated from the parametric wave-mixing between the pump and the signal. The quadratic temporal phase shift of the pump can be obtained by propagating a short pump pulse of bandwidth $\Delta\Omega_p$ through a dispersive path with total GDD D_p, such that the condition of far-field dispersion limit $\Delta\Omega_p^2 |D_p| \gg 1$ is fulfilled. In this way, the pump is linearly chirped with quadratic temporal phase

$$\phi_p(t) = -\frac{t^2}{2D_p}$$

which is extended through the full time window of the pump pulse and is independent of the power. However, it is important to notice that this approach leads to the dependency of the time-lens window profile on the spectral profile of the pump, thus a flat pump spectral profile is crucial to ensure equal conversion over the entire aperture of the time-lens.

We use in our setup a commercial (Picoluz UTM-1500) FWM based time-lens (Fig. 5.3), which allows the generation of idler wave with a wavelength close to the signal and pump wave,

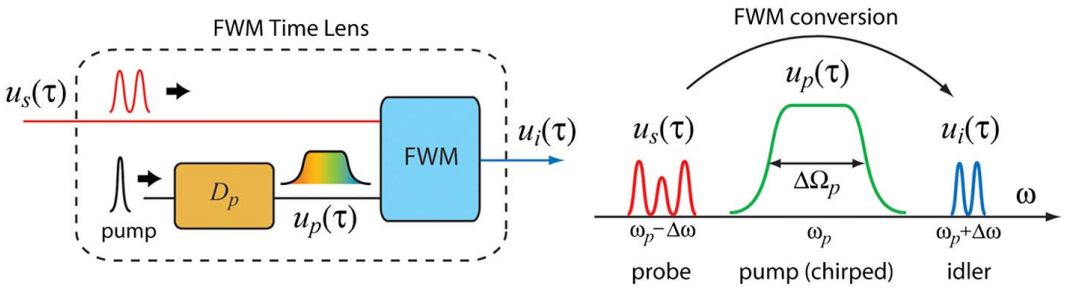

Figure 5.3: Time-lens system based on FWM. A signal wave is mixed with a linearly chirped (stretched) pump pulse through FWM process, generating an idler wave which is a replica of the input wave with an imparted quadratic phase. Here u_s, u_p, and u_i denote the electric field of the signal, pump, and idler respectively. *Source:* from Ref. [8].

such that the whole system can be operated within the telecommunication window [237, 238, 268]. The idler frequency ω_i satisfying the conservation of energy for FWM process can be calculated from the frequency of the pump ω_p and the signal ω_s, i.e. $\omega_i = 2\omega_p - \omega_s$, or in terms of wavelength can be written as

$$\lambda_i = \frac{\lambda_p \lambda_s}{2\lambda_s - \lambda_p}, \tag{5.6}$$

where λ_i, λ_p, and λ_s are the center wavelength of the idler, pump and the signal, respectively.

As we have seen earlier, the quadratic phase shift imparted by a time-lens to the input wave (the signal wave) can be calculated from its focal GDD D_f (Eq. 5.3). However, since the idler electric field $E_i(t)$ generated from the interaction of the pump $E_p(t)$ and the signal $E_s(t)$ follows the relation $E_i(t) \propto E_p^2(t)E_s^*(t)$, the focal GDD of the time-lens D_f is related to the GDD of the pump D_p through

$$D_f = -\frac{D_p}{2}, \tag{5.7}$$

which implies that the phase of the signal changes its sign when passing through the time-lens.

5.3.2 Experimental setup

Temporal imaging is formed by the combination of a time-lens with two dispersive paths placed before and after the time-lens (Section 5.1). These dispersive paths, together with the one used to stretch the pump pulse of the time-lens, are realised by dispersive propagation through optical fibres, which are included inside the ultrafast temporal magnifier module used here (Picoluz UTM-1500). The schematic of the experimental setup is shown in Fig. 5.4, presenting (a) the signal, (b) the pump, and (c) the temporal magnification process.

In our experiments, the temporal imaging was designed to give magnification of 76.4, which is defined by the ratio of the output to the input GDD (Eq. 5.5). The breather structures with 3 ps typical duration were then stretched into 0.23 ns duration pulses and can readily be captured in real time using our high-speed 38 GHz photoreceiver (New Focus 1474-A) connected to a 30 GHz channel of an ultrafast oscilloscope (LeCroy 845 Zi-A). The total temporal resolution of our time-lens system (taking into account the optical parameters of the time-lens and the electronic detection bandwidth) is < 300 fs. The detail of the experimental setup is discussed below.

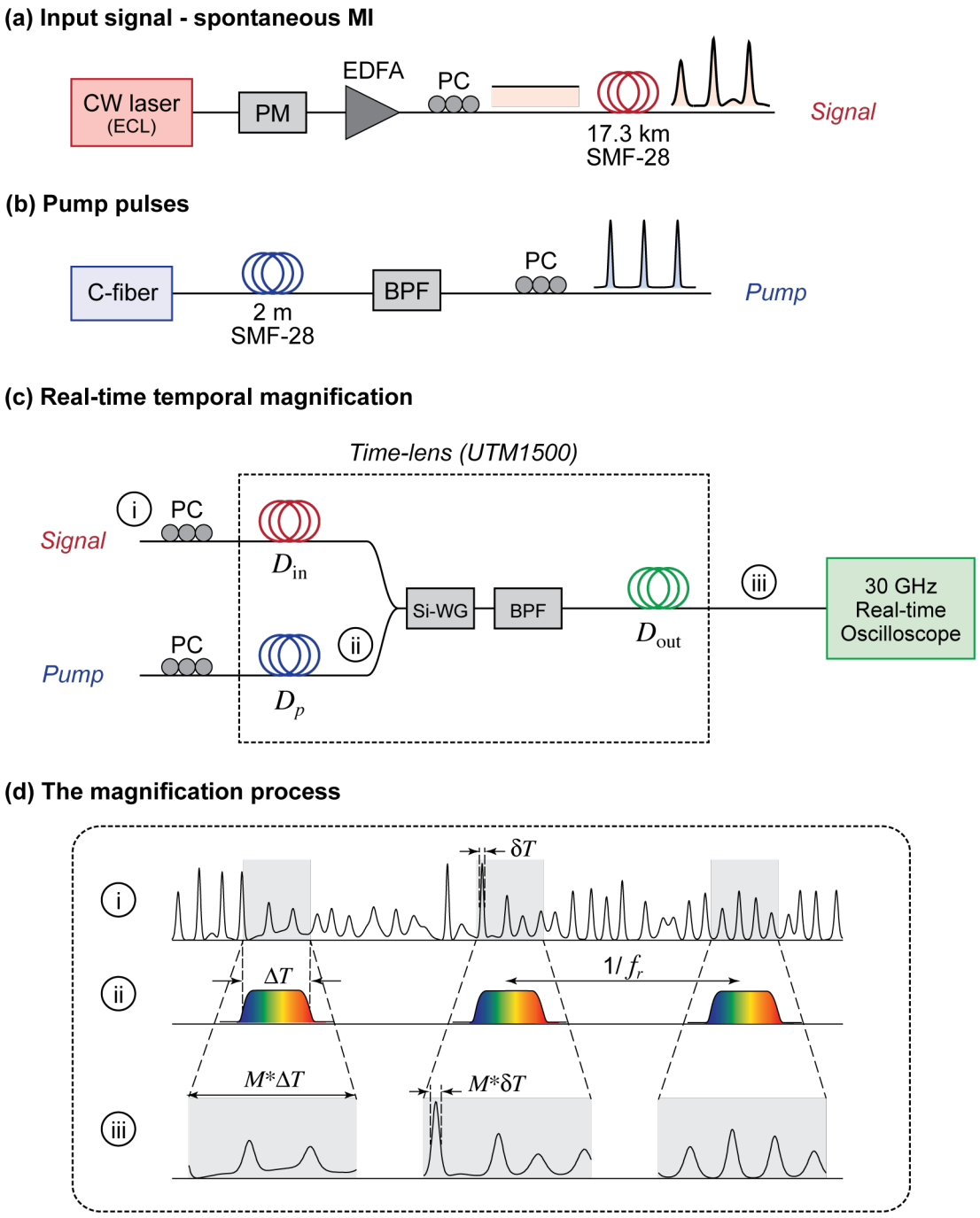

Figure 5.4: Experimental setup of the real-time temporal measurement of spontaneous MI on CW signal using ultrafast temporal magnifier (Picoluz UTM-1500). (a) The generation of the spontaneous MI on CW field. (b) The preparation of the ultra-short pump pulses. (c) The FWM based time-lens magnifier system. The signal and the idler were passed through dispersive propagation steps (D_{in} and D_{out}), before and after the time-lens system, respectively. The pump pulses were passed through dispersive propagation D_p before being combined with the signal in the silicon waveguide (Si-WG). This cascade process of the input dispersion, FWM based time-lens, and the output dispersion allows the signal waveform to be temporally magnified. (d) Illustration of the real-time temporal magnification process. (i) The temporal intensity profile of the breather structures with typical width $\delta T \approx 3$ ps. (ii) The linearly chirped pump pulses used to realise the time-lens system. (iii) The magnified breather structures (76.4×) ready to be measured by the ultrafast oscilloscope. The record length $M\,\Delta T \approx 5$ ns and refresh rate $f_r = 100$ MHz of the magnified waveforms are determined by the pump pulses.

Input dispersive path

In the temporal magnifier module (Fig. 5.4(c)), the spontaneous MI field was first propagated through the input dispersive path with GDD $D_{\text{in}} = 4.16$ ps/nm (-5.32×10^{-24} s^2), where it is related to the output GDD $D_{\text{out}} = 318$ ps/nm (-406.6×10^{-24} s^2) and the magnification factor through Eq. 5.5. A polarisation controller was required to optimise the idler power generated from the FWM process with the pump.

Pump dispersive path

Ultrashort pump pulses of ≈ 700 fs pulse width with repetition rate of ≈ 100 MHz were generated by a femtosecond fibre laser (Menlo C-fiber Sync and P100-EDFA). See Fig. 5.4(b). The pulse width measured at the output of the 2 m patchcord (connected to the C-fibre) was ≈ 140 fs. A band-pass filter (BPF) centered at wavelength ≈ 1570 nm with linewidth ≈ 12 nm was used to filter the spectrum of the pump in order to avoid the overlaps between the pump spectum and both the signal and the idler spectrum, while keeping the whole system to operate within the telecommunications window. For the optimisation of the FWM process, polarisation controller was used. The pump pulses entering the temporal magnifier system had an average power of ≈ 3 mW and pulse width of ≈ 90 ps.

In the temporal magnifier module (Fig. 5.4(c)), the pump pulses were then propagated through a dispersive path in order to generate highly chirped pump pulses. Following Eq. 5.7 and the condition for large magnification (the object is placed near to the focal length), the pump GDD D_p is required to be around twice the input GDD D_{in}. The pulse width of the pump pulse at the output of this dispersive path can be obtained by measuring the time-lens output of a CW signal (without the SMF-28), which determines the record length (aperture length) of the time-lens ΔT.

FWM

The time-lens imparts a temporally quadratic phase profile of the chirped pump pulses to the idler wave generated through the FWM process. The generated idler wave is centered around 1590 nm (following Eq. 5.6) and is sampled with the repetition rate of the pump (100 MHz). Indeed, the frequency conversion in the silicon waveguide occurs only under the presence of pump pulse. Consequently, the profile of the pump acts as a shutter or temporal pupil function, results in idler with temporal width approximately equal to the record length of the time-lens ΔT.

Idler dispersive path

As discussed earlier, in the limit of large temporal magnification, the time-lens functions as a Fourier processor which translates the intensity profile of the signal into the spectrum of the generated idler. This encoded input waveform in the spectrum of the idler is then converted back into its time domain intensity profile through a large dispersive propagation ($|D_{\text{out}}| \gg \Delta T^2$), which in this case is 76.4$\times$ larger than D_{in}. This real-time temporal magnification process is illustrated in Fig. 5.4(d), yielding the magnified temporal traces with record length of $M\,\Delta T \approx 5$ ns at the output of the time-lens magnifier system, which can be resolved by the ultrafast oscilloscope.

5.4 Experimental results and statistical analysis

The generation of the idler wave from the FWM process between the signal and the pump yields the magnified waveform to exhibit the intensity profile of the signal with background intensity from the pump pulses. In order to extract the intensity profiles of the breather pulses, the measured intensity therefore needs to be normalised to the mean background power $P/\langle P\rangle$. This mean background can be obtained from the average of the sampled waveform measured at the output of the time-lens magnifier system, generated either from the CW input (without passing through SMF-28), or by a numerical average of the measured chaotic MI signal. We verified that these two measurements gave the same mean background profile.

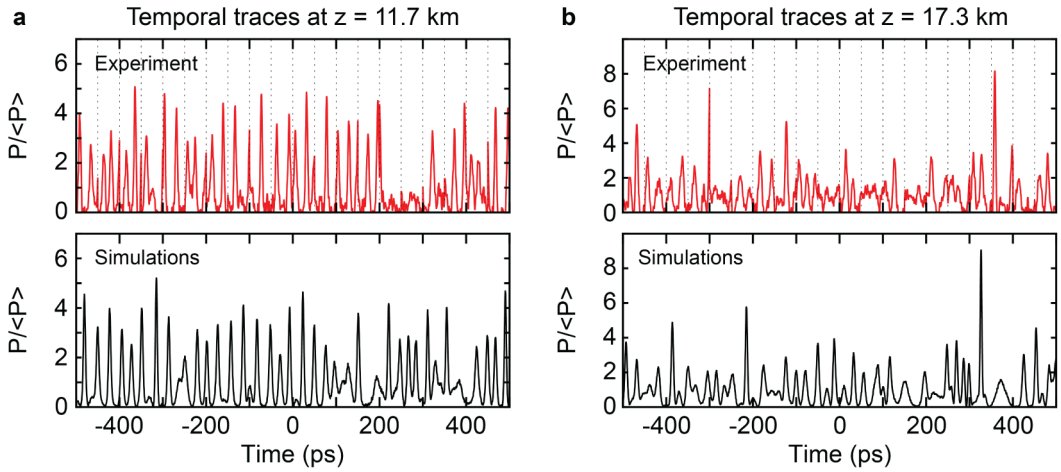

Figure 5.5: Intensity profiles obtained from the time-lens measurements (top, red) and simulations (black, bottom) at two different fibre length: (a) 11.7 km and (b) 17.3 km. Measured intensities P are normalised with respect to the mean output background intensity $\langle P\rangle$, plotted against the rescaled (demagnified) time. Experimental results from several measurement windows (indicated by dashed vertical lines) are concatenated for comparison with simulation.

The retrieved intensity fluctuations obtained from the time-lens measurements are shown in the top panel of Fig. 5.5 (red), characterising the breather pulses generated at fibre length of 11.7 km (in the initial MI compression regime) and 17.3 km (in the chaotic MI regime). Due to the limitation of the time window, the intensity profile shown here is constructed from the concatenation of breather pulses obtained from several time windows. Note that the breather structures were only detected over a central 3.8 ns window of the sampled traces (corresponding to a demagnified measurement window of 50 ps), with typically 5-10 distinct breathers resolved for each time window. Additionally, a low-pass filter was also applied to the measured temporal traces in order to remove high-frequency noise arising from the electronic detection system, such that both the intensity profile and the peak intensity of each breather structure can be retrieved accurately. In this way, the intensity time series $P/\langle P\rangle$ can be readily compared with the simulation shown in the bottom panel of this figure (black).

5.4.1 Spontaneously emergent breathers

In a similar way as we have seen in Section 4.3, the spontaneously emergent localised structures can be characterised by the analytic SFB solutions (breathers) structures. To this end, we plot in Fig. 5.6(a) and (b) the pulse duration (FWHM) against the corresponding normalised peak intensity $P/\langle P\rangle$ of the breather intensity profiles extracted from experiments (top, red points) and simulations (bottom, black points), compared to the theoretical curve. The scatter plots are obtained from around 30000 distinct pulses from experiments (only taken from pulses with peak intensity $P/\langle P\rangle > 2$) and 50000 distict pulses from simulations. Whilst the theoretical curve is calculated in the same way as shown in Fig. 4.7, evaluated at the point of maximum localisation of both the elementary and higher-order (in phase collision) breathers.

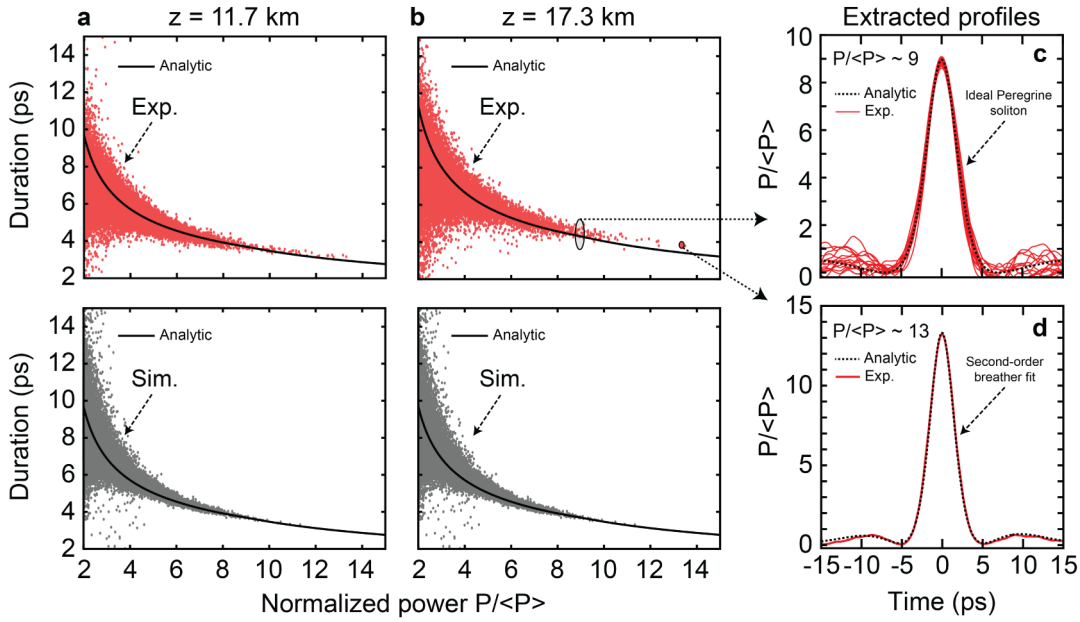

Figure 5.6: (a) and (b) show scatter plots of pulse duration against normalised power from the intensity profiles obtained from the experiments (top, red points) and simulations (bottom, black points), taken at 11.7 km and 17.3 km propagation distance respectively. For each case, the theoretical curve calculated from the elementary and higher-order breather solutions is also plotted as comparison. The figures on the right panel plot the intensity profiles extracted from the experimental results (red lines) compared to the analytical fits (black lines) for (c) $P/\langle P\rangle \approx 9$ and (d) $P/\langle P\rangle \approx 13$.

Significantly, these plots show that although the FWHM and the peak intensity of the chaotic MI breathers are not necessarily taken at the point of maximum localisation of the breathers, the scatter points clearly cluster around the theoretical curve. These experimental results confirm the earlier conclusion made in Chapter 4.1 that the analytic SFB solutions provide the natural basis to interpret the spontaneously emerging localised structures in a system governed by the NLSE.

We also compared the intensity profiles of the breathers extracted from the experiments with the analytic breather solutions. Fig. 5.6(c) superimposes 10 intesity profiles with maximum intensity $P/\langle P\rangle \approx 9$ (red lines) with the theoretical analytic Peregrine Soliton structure (dashed black line) [200], while Fig. 5.6(d) plots the intensity profile of a higher-order breather with maximum intensity $P/\langle P\rangle \approx 13$ (red line) with the analytic second-order breather solution

(dashed black line) constructed using the Darboux transformation discussed in Section 4.1.2 [204]. These fits show the remarkable agreement between the experimentally measured temporal profile and the analytical solutions.

5.4.2 Statistical analysis

The large amount of data acquired from the experiments allows a convenient statistical analysis. We plot in Fig. 5.7 the histogram (probability density) of the peak intensities of the chaotic pulses obtained from the experiments (red) and simulations (black), for the propagation distance of (a) 11.7 km and (b) 17.3 km. The inset shows the semi-logarithmic plot. In both cases, the experiments and simulations are in good agreement for peak intensity $P/\langle P\rangle < 9$, while only the distributions taken from the chaotic MI regime (Fig. 5.7(b), at 17.3 km propagation) agree well for higher peak intensities. The discrepancy observed in the Fig. 5.7(a) is attributed to uncertainties in modelling the input noise, which is crucial in determining the initial evolution of the MI field, but less significant for longer distances in the chaotic MI regime [211]. Notice that the distribution taken at distance 11.7 km exhibits a maximum at $P/\langle P\rangle \approx 3.5$ as a result of the more uniform AB-like pulses generated in this initial MI compression regime.

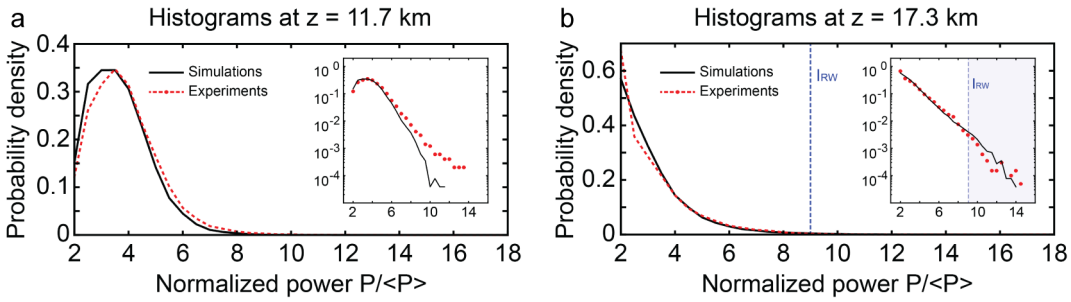

Figure 5.7: Histograms (probability density) of the peak intensities from the spontaneous MI pulses taken at propagation distance of (a) 11.7 km and (b) 17.3 km. The inset plots the histogram on semi-logarithmic axes. For each case, the histogram obtained from the experiment (red) is compared to the one from simulation (black). The dashed blue lines indicate the rogue wave intensity threshold I_{RW}.

Calculating the rogue wave intensity limit I_{RW} from the experimental data shown in Fig. 5.7(b), we obtained $I_{\mathrm{RW}} \approx 9.2$ with $\approx 0.3\,\%$ of the peak intensities exceeding this value, which is remarkably close to the simulation results obtained in the previous chapter ($I_{\mathrm{RW}} \approx 9.1$ with $\approx 0.26\,\%$ peak intensities defined as rogue waves).

5.5 Conclusions

In this chapter, we have reported results of the first real-time experimental study of noise-driven modulation instability in optical fibre. We have shown that the ultrafast temporal dynamics of the spontaneously emergent MI breathers can be measured in real time using a time-lens magnifier system. Significantly, the experimental results here confirm the simulation results obtained in the previous chapter, showing that indeed the temporal stuctures of the spontaneous MI can be described by the analytical SFB solutions. Furthermore, the large amount of data obtained from

the experiments allows statistical analysis of the peak intensity of the temporal MI pulses, again confirming the previous prediction of statistical rogue waves being associated with higher-order breathers.

Chapter 6

Stimulated modulation instability in optical fibres

In contrast to the study of spontaneous modulation instability (MI) conducted in the previous chapters (Chapter 4 and 5), we will study in this chapter the generation of rogue waves from a stimulated MI. Although the generation of MI in optical fibre induced by a co-propagating coherent field has been demonstrated from the very early development of MI study [169, 270, 271], our main concern here is on the spectral properties of MI that is triggered by a very weak coherent or partially-coherent seed. The MI studied here is generated on picosecond pulses and their shot-to-shot (pulse-to-pulse) spectral structures are recorded in real-time.

Apart from its significance linked to the understanding of rogue waves emergence in different physical systems, this study may also have an impact on the development of high-power broadband sources through the generation of supercontinuum (SC) in a fibre by using long pulses [272]. In particular, it has been both numerically and experimentally shown, that spectral structure and noise properties of MI driven SC generation, for both femtosecond and picosecond pulse pumping, is highly sensitive to the presence of a weak co-propagating seed [31, 273–276]. The fact that a low amplitude seed can strongly affect MI can be understood physically because the seed creates an initial modulation on the pump that will undergo preferential growth relative to the weaker broadband noise. In these previous studies, however, the SC are generated from strongly coherent seed and pump sources, using either a narrow linewidth continuous wave (CW) laser [276] or a low amplitude pulse replica derived from the pump [31].

In this study, we investigate the control of MI by coherent and partially-coherent seed in MI regime. In particular, using finite bandwidth amplified spontaneous emission (ASE) as the partially-coherent seed, we show that resonant enhancement of the MI spectral width and noise reduction can still be observed, although with somewhat weaker effects compared to the case of coherent seeding. Note also that in contrast to other studies of induced MI in the spatial domain using a strong incoherent pump and coherent seeds [223, 277, 278], the work here is conducted in the temporal domain using a coherent pump and a very weak partially-coherent seed.

6.1 Experimental setup

The experimental setup is shown in Fig. 6.1. The input pump pulses are first combined with a coherent or partially-coherent seed before being propagated through a highly nonlinear fibre (HNLF) where the MI process takes place. The shot-to-shot spectra of the seeded MI pulses are then measured in real-time with dispersive Fourier transform (DFT) method by passing the pulses through a long dispersion compensating fibre (DCF).

The input pump pulses centered at 1552 nm with repetition rate 20 MHz are generated from a picosecond fibre laser (Pritel FFL-500). The pulses are amplified by an erbium-doped fibre amplifier (EDFA) before being combined with the weak external seed. The amplified pump pulses are then characterized using an optical spectrum analyzer (OSA, Anritsu MS9710Bm, with 0.07 nm spectral resolution) and frequency-resolved optical gating (FROG). The measured temporal width (FWHM) of the pump pulses T_0 is 3.8 ps with time-bandwidth product $\Delta\tau\Delta\nu \approx 0.42$. The spectrum shows characteristic features of self-phase modulation.

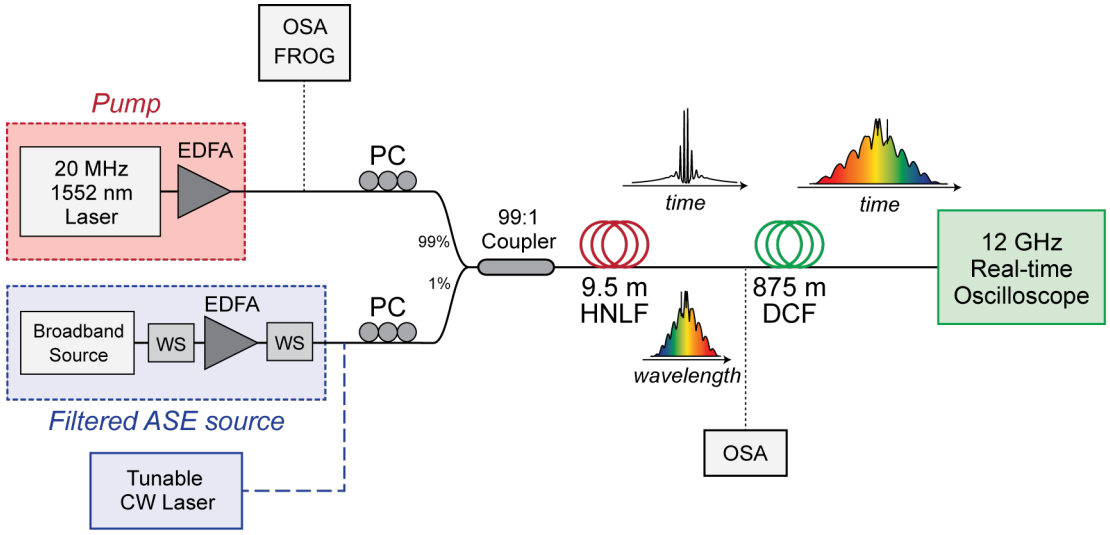

Figure 6.1: Experimental setup of coherent and partially-coherent seeded MI. A tunable continuous wave (CW) laser is used for the coherent source, while a filtered amplified spontaneous emission (ASE) was used for the partially-coherent source. The real-time (shot-to-shot) MI spectra are measured by using dispersive time stretching technique. EDFA: Erbium-doped fibre amplifier, WS: waveshaper, PC: polarisation controller, HNLF: highly nonlinear fibre, DCF: dispersion compensating fibre, OSA: optical spectrum analyser, FROG: frequency-resolved optical gating.

The coherent seed was generated from an external cavity laser (ECL) Agilent 81949A with wavelength tunable over 1520−1630 nm. The partially-coherent seed was derived from an amplified ASE source (Highwave HWT-BS-B1-2) which is spectrally shaped with a tunable filter (Finisar Waveshaper 4000S). This filtered ASE seed was then amplified in order to keep the same pump and coupler configuration used for the case of coherent seed. Another tunable filter (Finisar Waveshaper 4000S) was used to eliminate the unwanted amplified noise in order to obtain precise control over the spectral bandwidth. In this way, the ASE seed could be configured to have variable bandwidth from 1 to 36 nm with central wavelength tunable over 1527 − 1550 nm.

The pump pulses were combined with the coherent CW or partially-coherent ASE seed before entering a 9.5 m Ge-doped highly nonlinear fibre (OFS HNLF) with nonlinear coefficient γ =

10.5 $W^{-1}km^{-1}$ and dispersion parameters $\beta_2 = -5.24$ ps^2km^{-1} and $\beta_3 = 4.29 \times 10^{-2} ps^3km^{-1}$ at wavelength 1550 nm. The average pump power at the HNLF input was 6.4 mW ($P_0 = 68$ W peak power), the average CW seed power was 53 μW, and the average ASE seed power was 90 μW. Notice that the average power of the seeds are in the order of 10^6 times lower than the pump.

The shot-to-shot spectral fluctuations are directly measured by using dispersive time stretching technique, also known as dispersive Fourier transform (DFT) method [219–221]. This technique is based on the mathematical equivalence between paraxial diffraction and temporal dispersion, which has been discussed in Section 5.1 of the previous chapter; the intensity of a temporal field evolves into its Fourier transform after sufficient propagation in a linear dispersive medium [251].

For total dispersion $\beta_{2S}L$, where β_{2S} is the second order dispersion and L is the length of the "stretching" fibre, an input pulse $U(t)$ with Fourier transform $\tilde{U}(\omega)$ spreads in time to have intensity that is a scaled replica of the input spectrum at the fibre output

$$|U_L(t)|^2 \propto \left|\tilde{U}(t/(\beta_{2S}L))\right|^2.$$

The spectrum of the pulse ν can therefore be calculated using the relation

$$\omega = 2\pi\nu = \frac{t}{\beta_{2S}L}.$$

In this experiment, the dispersive time stretching was realised by propagating the pulses along 875 m dispersion compensating fibre (DCF) with total dispersion $\beta_{2S}L = 130$ ps^2. At the output of this dispersive fibre, the nanosecond stretched pulses with profile of their corresponding spectra can then be easily detected in real time by using a 20 GHz detector (New Focus Model 1414) and 12 GHz oscilloscope (Tektronix TDS 6124C). The equivalent spectral resolution with this setup was 0.8 nm. Additionally, we also recorded the average spectrum of the pulses by an OSA, which can then be compared with the calculated average of the real-time spectra.

6.2 Spontaneous, coherent seeded, and partially-coherent seeded MI

In order to understand the influence of the coherent and partially-coherent seed on the stimulated MI spectra, we present in this section numerical simulation results based on the setup in Fig. 6.1. Specifically, we compare the width and the noise fluctuation of the measured shot-to-shot spectra of the stimulated MI and the spontaneous MI. We use the GNLSE previously shown in Section 2.4.2 (Eq. 2.23) to model the propagation of the pump pulses with the co-propagating seed inside the HNLF. This equation has been commonly used to model the statistics of SC generation including dispersion to arbitrary order, self-steepening, and Raman scattering [279]. The parameters of the pump pulses entering the HNLF used in our simulation are taken from the FROG measurement, while the simulated ASE seed is fitted to the filtered spectrum (using Gaussian fit) with added random phase.

Higher-order terms in the GNLSE, however, were found to have negligible influence in the MI regime propagation of our 3.8 ps input pulses, which were confirmed by our simulations. Indeed,

third-order dispersion β_3 has significant contribution only when $T_0|\beta_2/\beta_3| \leq 1$, while the effect of self-steepening and Raman scattering in this case were found to be very small [162]. The pulse evolution can therefore be sufficiently modeled with the NLSE shown in Eq. 2.21.

6.2.1 Shot-to-shot MI spectral fluctuations

We compare the spectra of spontaneous MI, coherent seeded MI, and partially-coherent seeded MI in the lower panel of Fig. 6.2 (a), (b), and (c) respectively, plotting both the simulated shot-to-shot spectra (gray) and the calculated average (black). The simulations are performed with different initial random noises for 5000 individual realisations. The wavelength of the coherent and partially-coherent seed is centered around the maximum of the MI gain curve, at 1531 nm, as can be seen from the sideband location of the spontaneous MI spectra, and which can also be verified from the equation $\Omega_{\text{max}} = \pm\sqrt{2\gamma P_0/|\beta_2|}$ presented in Section 2.4.2. We can see a significant increase in the bandwidth of stimulated MI spectra in Fig. 6.2(b) and (c) ($\approx$ 200 nm at the -50 dB level) compared to the bandwidth of the spontaneous MI spectra in Fig. 6.2(a) ($\approx$ 100 nm at the -50 dB level).

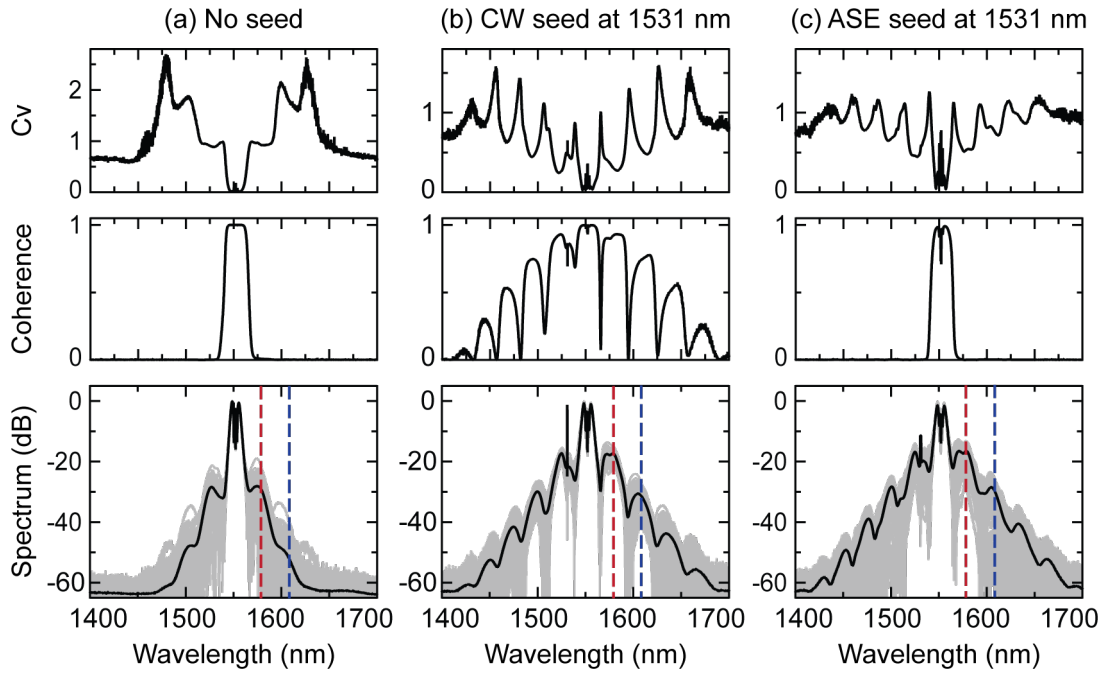

Figure 6.2: Simulation results. Bottom panel plots MI spectra for (a) no seed, (b) CW seed at 1531 nm, (c) 1 nm bandwidth ASE seed at 1531 nm. The spectral broadening in (a) is the results of spontaneous MI (noise seeded), while (b) and (c) are results of stimulated MI. Individual realisations are shown in gray (superposes 500 spectral traces) with the average in black. Vertical red and blue dashed lines indicate the wavelength of the first and second MI sideband, from where the distributions shown in Fig. 6.3 are taken. Upper panels show second-order spectral coherence and coefficient of variance C_v.

The upper panels of Fig. 6.2 compare the corresponding noise properties of the shot-to-shot spectra. The noise statistics are shown by means of the spectral coherence and coefficient of variation that are calculated from the simulation ensemble for each of the spectral component.

The spectral coherence g_{12} is defined as

$$|g_{12}(\omega)| = \left| \frac{\left\langle \tilde{A}_i^*(\omega)\tilde{A}_j(\omega) \right\rangle_{i\neq j}}{\sqrt{\left\langle |A_i(\omega)|^2 \right\rangle \left\langle |A_j(\omega)|^2 \right\rangle}} \right|,$$

where $\tilde{A}_i(\omega)$ is the amplitude of independent spectra. The coefficient of variation C_v is defined as $C_v = \sigma/\mu$, where σ and μ are the standard deviation and the mean of the spectral intensity distribution at a specific wavelength respectively. This coefficient is a suitable parameter of measuring the noise to signal ratio of the spectral fluctuations, as it measures the statistical dispersion of the spectral intensity for each frequency component [220, 274].

In the case of CW seeded MI, plotted in Fig. 6.2(b), we see a reduction in the shot-to-shot spectral fluctuations, marked by the lower value of C_v across the MI bandwidth. The improved coherence across the MI bandwidth in this case is expected because MI develops from low amplitude coherent modulation due to beating between the pump and the seed [273].

In the case of finite bandwidth ASE seeded MI, plotted in Fig. 6.2(c), similar reduction in the shot-to-shot spectral fluctuations is still observed, with C_v slightly higher compared to the one of CW seeded MI. Significantly, these simulation results show that even a very weak partially-coherent seed can still provide a stabilisation of spectral shot-to-shot fluctuations similar to that seen in the weak coherent seed case, which will be confirmed by the experimental results shown in the next section. However, in contrast to the CW seed case, the partially-coherent nature of the ASE seed does not yield coherence improvement across the bandwidth.

6.2.2 Sideband noise suppression

Although spectral fluctuations of the partially-coherent and coherent seeded MI are similar, a detailed examination of the coefficient of variation plots shown in Fig. 6.2 reveals some important differences. In particular, we can see that the C_v at the sidebands of the partially-coherent seeded MI are higher than at the sidebands of the coherent seeded MI, which indicates higher shot-to-shot spectral fluctuations. Further insight into the properties of the fluctuations can be gained by comparison of their spectral intensity distributions.

We compare in Fig. 6.3 the histograms of the spectral intensity components taken from the first MI sideband (1580 nm) and the second MI sideband (1607 nm), for the case of no seed, with CW seed, and with 1 nm bandwidth of ASE seed. In the case of no seed (Fig. 6.3(a)), the distributions of the spectral fluctuations in both sidebands are highly skewed, with longer tail observed on the distribution taken in the second sideband. When the MI is seeded by the CW (Fig. 6.3(b)), the spectral fluctuations in both sidebands are highly suppressed, yielding Gaussian-like distributions. Whilst when seeded by the ASE seed (Fig. 6.3(c)), the spectral fluctuations in the first sideband are highly suppressed, but much weaker suppression is observed for the second sideband. Notice that for each sideband, the distribution of the ASE seeded MI shows superposition profile between those of the spontaneous MI and the coherent seeded MI.

These results imply that an effective stabilisation of shot-to-shot spectral fluctuations by partially-coherent MI seeding can be obtained only in the first MI sideband region. These results

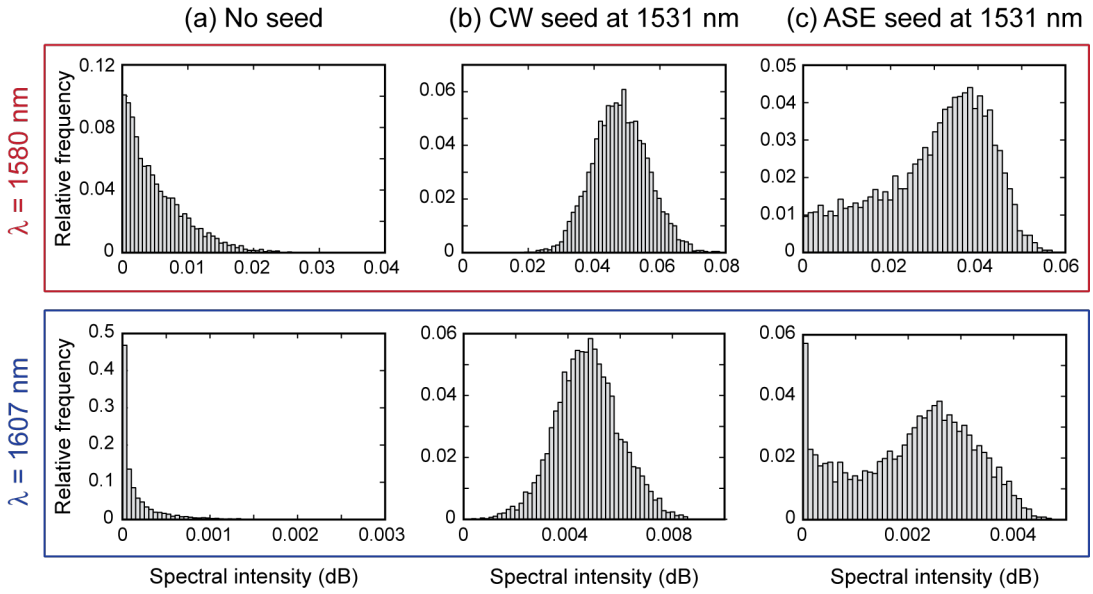

Figure 6.3: Histograms data of spectral fluctuations from first sideband at wavelength 1580 nm (top) and second sideband at wavelength 1607 nm (bottom). For each wavelength three cases of MI spectra are shown, for (a) no seed, (b) CW seed, (c) 1 nm bandwidth ASE seed. The histograms are calculated from 5000 realisations of the simulation data.

can be understood considering that the first sidebands are generated from a direct FWM process between the spectrally-broadened coherent pump and the partially-coherent seed, while the second (and the higher harmonics) MI sidebands are formed by subsequent cascaded FWM process. For this reason, in the next section we will only focus on the noise properties of the first sidebands.

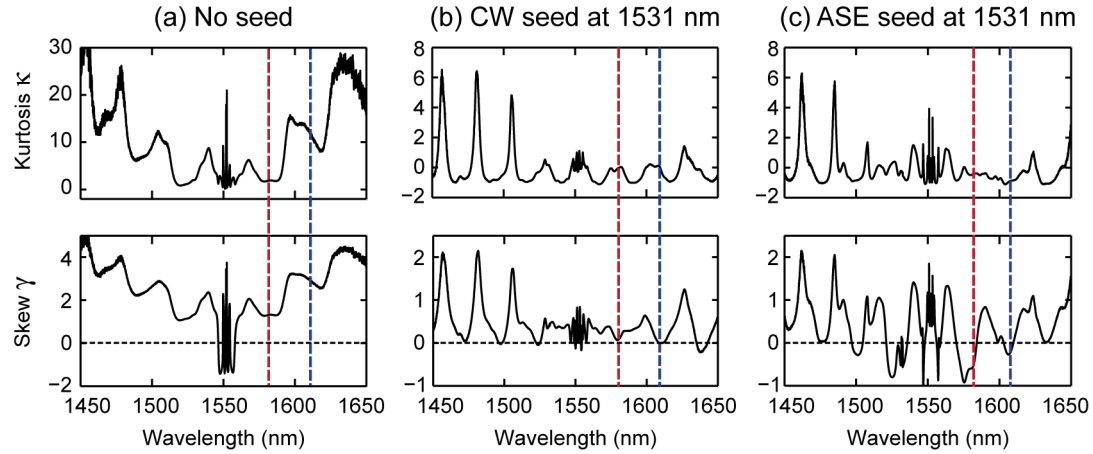

Figure 6.4: Calculated second-order moment (skew γ) and third-order moment (kurtosis κ) of the MI spectra for (a) no seed, (b) CW seed, (c) 1 nm bandwidth ASE seed. Vertical red and blue dashed lines indicate the wavelengths corresponding to the distributions shown in Fig. 6.3.

Additionally, the noise properties of each spectral component can also be quantified in terms of their higher-order statistical moments, as has been demonstrated in Ref. [220]. Similar to the coefficient of variation C_v plot shown in Fig. 6.2, we plot in Fig. 6.4 the skewness $\gamma = \mu_3/\sigma^3$ and the kurtosis $\kappa = \mu_4/\sigma^4 - 3$ of the distributions, where $\mu_n = \langle (I - \langle I \rangle)^n \rangle$ is the n^{th}-order

central moment and σ is the standard deviation. The skewness γ quantifies the asymmetry of the distribution, while the kurtosis κ quantifies the heaviness of the tail of the distribution.

These plots of higher-order moments can be compared directly with the distributions shown in Fig. 6.3. In the case of spontaneous MI, the skewness γ and the kurtosis κ of the spectral fluctuations at the second sidebands are higher than those at the first sidebands, corresponding to the more skewed and longer tailed distribution observed at the second sidebands. In the case of CW seeded MI, these two parameters are significantly low in all of the sidebands (near to 0), corresponding to their gaussian-like distribution profile due to the noise suppression. Whilst in the case of ASE seeded MI, the negative value of the skewness γ at the first sidebands corresponds to the negative-skewed distribution observed in the top panel of Fig. 6.3(c)

6.2.3 Effect on pump noise

Noise suppression at the stimulated MI sidebands can be expected because the MI spectrum is generated from the FWM interaction between the coherent pump with the coherent or partially-coherent seed. It is therefore interesting to see whether similar effect can also be observed on the pump spectral component. Specifically, whether the distribution of the spectral intensity is also transformed when the MI is seeded by coherent or partially-coherent seed. Since the pump spectrum has been broadened by the SPM, we compare here the statistics of the spectral intensity taken at the peaks of the SPM-broadened pump.

We plot in Fig. 6.5 a small portion of the simulated spectra and the skewness γ parameter around the center wavelength, together with the histograms of the shot-to-shot spectral fluctuations taken from the first peak (1553 nm) and the second peak (1556 nm) of the SPM-broadened pump spectra. Similarly as before, we compare the spectral fluctuations of the spontaneous MI (no seed), CW seeded MI, and ASE seeded MI.

First, we notice the pronounced transformation of the spectral intensity distributions in the case of seeded MI (bottom panels of Fig. 6.5). Highly-skewed distributions of spontaneous MI are transformed into Gaussian-like distributions when MI is seeded by coherent seed, and to less-skewed distributions when seeded by partially-coherent seed. These transformations can be seen from the skewness γ parameter plotted on the top panel of Fig. 6.5, where the negative value of γ at the peaks of the SPM-broadened pump spectra for the spontaneous MI is suppressed into nearly zero for the coherent seeded MI and the partially-coherent seeded MI.

Second, we contrast the histograms taken at the peaks of the SPM-broadened pump spectra shown here with those of the MI sidebands plotted in Fig. 6.3. We can see that these distributions seem to be negatively-correlated. For spontaneous MI, in contrast to the positively-skewed distributions observed in the MI sidebands, we obtain here negatively-skewed distributions. While we obtain symmetric Gaussian-like distributions for the CW seeded MI and superposition distribution profile for the ASE seeded MI, showing similar behaviour as earlier. This observation shows that the amplification of MI sidebands is indeed realised in the expense of the SPM-broadened pump spectra. This negative-correlation relation can also be seen from the correlation map shown in Ref. [220].

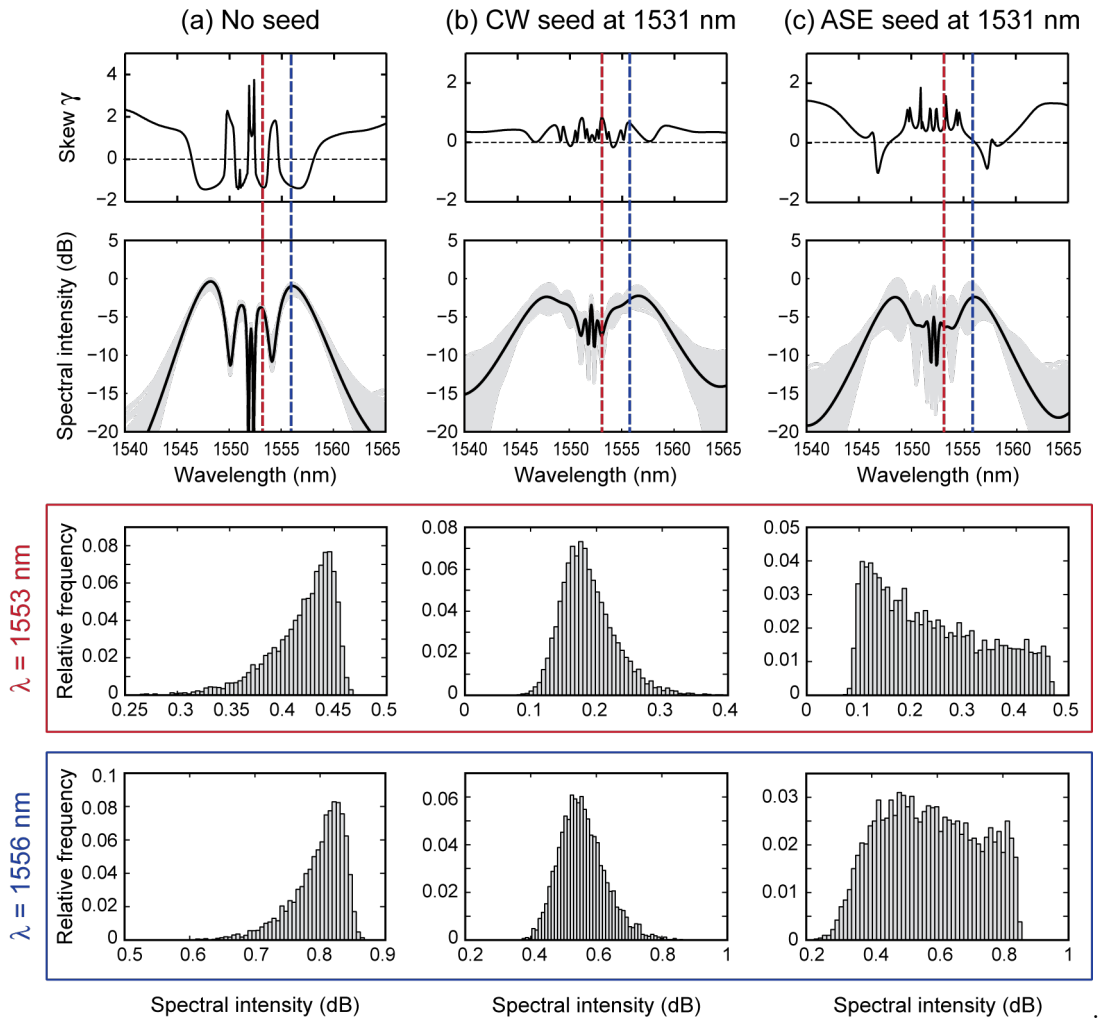

Figure 6.5: Seeding effect on spectral fluctuations of coherent pump. Upper panels show the calculated normalised third-order moments (skewness γ) and the spectra around the pump wavelength. Lower panels show the histogram data at wavelength 1553 nm and 1556 nm. The histograms and the skewness are calculated from 5000 realisations of the simulation data. Comparison is made for (a) no seed, (b) CW seed, (c) 1 nm bandwidth ASE seed.

6.3 Experimental results of seeded MI

In this section, we analyse the spectral broadening and noise suppression properties of partially-coherent seeded MI in more details. Specifically, we investigate the effect of varying the wavelength and the bandwidth of the partially-coherent seed. We show that the simulation results are in good agreement with the experiments.

6.3.1 Wavelength dependence

We examine first how the MI spectra structures and noise properties vary as a function of partially-coherent seed wavelength. Similarly as above, the partially-coherent seed here is derived from a filtered ASE source of 1 nm bandwidth.

As discussed in Section 2.4.2, the range of MI frequency extends from zero detuning up to a maximum frequency of $(1/(2\pi))(4\gamma P_0/|\beta_2|)^{1/2} = 3.72$ THz, with maximum MI gain at 2.63 THz. This range of frequency correponds to ±30 nm from the 1552 nm pump wavelength with maximum MI gain at ±21 nm. With our setup shown in Fig. 6.1, we were only able to generate the ASE seed within the shorter wavelength side of the pump (corresponding to the positive frequency detuning) which range from 1527 to 1550 nm. Nonetheless, we have tested in simulations that the same effect is observed when the MI is seeded using the opposite side of the wavelength.

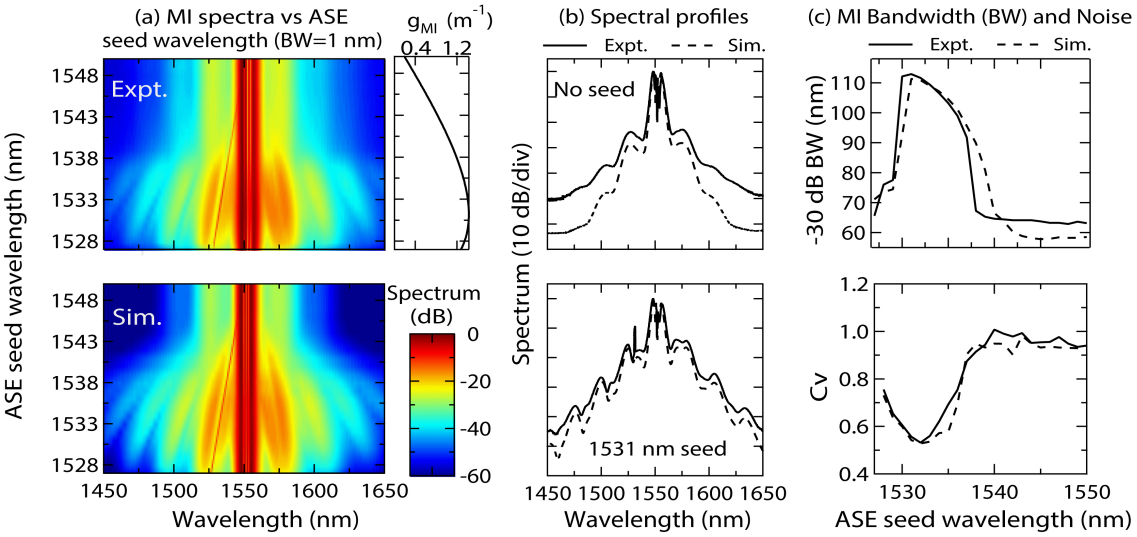

Figure 6.6: (a) MI spectral profiles as ASE seed wavelength is varied. The MI gain curve is shown beside the experimental density plot. (b) Experimental average spectra taken from 5000 single-shot spectra (solid) and numerical average spectra taken from 5000 numerical realisations (dashed) for unseeded (top) and for a 1531 nm seed (bottom). (c) Seed wavelength dependence of −30 dB MI bandwidth (top) and C_v at 1580 nm (bottom).

Figure 6.6(a) shows a false-color plot of the spectrum measured using an OSA when the partially-coherent seed is scanned across the MI gain curve. We can see that as the center wavelength of the seed is varied from 1527 to 1550 nm, the MI spectral structure is first broadend and then narrowed back, following the calculated MI gain curve. Maximum broadening of the spectrum with multiple MI sidebands structure is observed at wavelength around 1531 nm, while only little spectral modification is observed for wavelength corresponding to low MI gain. We compare these results with numerical simulations taking the average spectra of 500 numerical realisations for each seed wavelength, which is plotted in the lower panel of Fig. 6.6(a). We can see a remarkable visual correspondence between the simulation and the experimental results, where similar spectral structures are reproduced for all seed wavelengths.

A direct comparison between the simulated and measured spectra for unseeded and seeded at the MI peak gain are shown in Fig. 6.6(b). Note that the unseeded MI spectral structure is very similar to the MI spectra seeded at wavelength corresponding to very low MI gain. For these plots, the experimental average spectra are taken from 5000 single-shot spectra and the simulation average spectra are taken from 5000 numerical realisations.

The dependence of the spectral bandwidth and the shot-to-shot spectral fluctuations on the ASE seed wavelength is plotted in Fig. 6.6(c). The spectral bandwidth is taken at the −30 dB

level, while the spectral fluctuations are measured by the coefficient of variation C_v of the spectral intensity at 1580 nm wavelength. In both cases, the experimental results are compared with the stochastic numerical simulations and again are in very good agreement. These plots show that indeed the spectral bandwidth and the noise reduction are correlated to the MI gain.

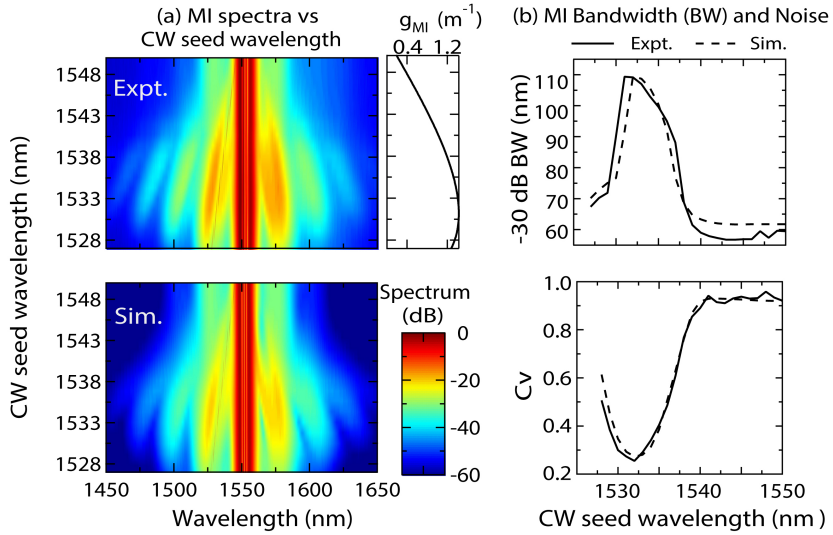

Figure 6.7: (a) MI spectral profiles as CW seed wavelength is varied. The MI gain curve is shown beside the experimental density plot. (b) Experimental average spectra (solid) and numerical results (dashed) for unseeded (top) and for a 1531 nm seed (bottom). (c) Seed wavelength dependence of −30 dB MI bandwidth (top) and C_v at 1580 nm (bottom).

For a comparison with the coherent seeded MI, we plot in Fig. 6.2 the experimental and simulation results of the CW seeded MI spectra, together with the spectral bandwidth and the coefficient of variation C_v, as a function of CW seed wavelength. Similarly, the spectral bandwidth is taken at the −30 dB level, while the C_v is calculated from the spectral intensity components at 1580 nm wavelength. Notice that although the spectral broadening does not show significant difference with the ASE seeded MI, the values of C_v here are much lower. Specifically, we can see that the C_v of the CW seeded MI at the maximum MI gain (1531 nm) reaches its minimum of ≈ 0.25, while it is only ≈ 0.52 in the case of ASE seeded MI. These results are expected considering that CW is the limit when ASE bandwidth approaches zero, as we shall see in the following experiments.

6.3.2 Bandwidth dependence

The comparable results of the ASE seeded MI to the CW seeded MI show that the initial modulation across the pump due to the partially-coherent seed still possessed sufficient amplitude stability to strongly influence the pump dynamics. To understand this physically, we compare the coherence time of the seed with the pump pulse duration. The coherence time of a 1 nm bandwidth ASE seed centered at wavelength $\lambda = 1531$ nm, calculated from $\tau_c = \lambda^2(c\Delta\lambda)^{-1}$ where c is the speed of light, is $\tau_c \approx 8$ ps, which is longer than the pump pulse width of 3.8 ps. The strong seeding effect can therefore still be expected due to the stable phase of the induced modulation across each pump pulse.

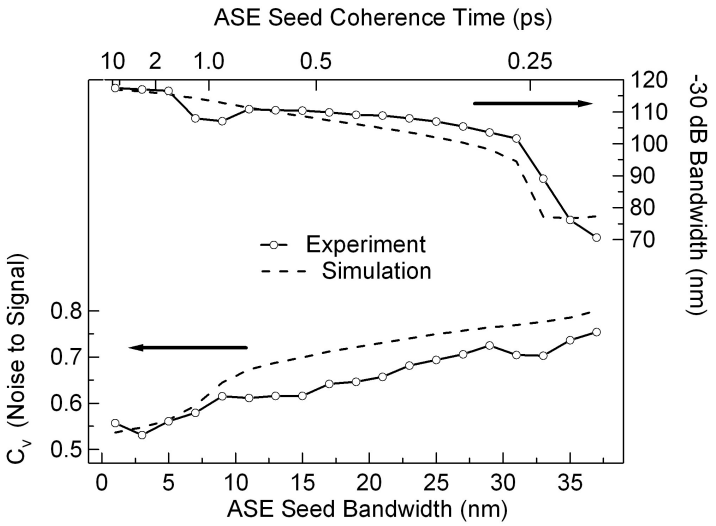

Figure 6.8: Experimental results showing the variation with ASE seed bandwidth centered at wavelength $\lambda = 1531$ nm of (top) -30 dB MI bandwidth and (bottom) C_v at 1580 nm.

This interpretation suggests that a broader ASE bandwidth (shorter coherence time) will result on a weaker seeding effect. To this end, we increase the ASE bandwidth using the filtering setup shown in Fig. 6.1 from 1 to 36 nm, which corresponds to the decrease of the coherence time from 8 to 0.21 ps. We plot the MI spectral bandwidth at -30 dB level and the coefficient of variation C_v at 1580 nm as a function of ASE bandwidth in Fig. 6.8, taken from both the simulation and the experimental spectra.

As expected, the MI spectral bandwidth and the noise reduction are significantly decreased for wider ASE seed bandwidths (shorter coherence times). We can see that for much shorter coherence time, the effect of the seed becomes negligible, where the MI bandwidth and the C_v become comparable to the case of unseeded MI. Taking the ASE seed bandwidth of 36 nm, corresponding to coherence time of 0.2 ps (more than 10 times smaller than the 3.8 ps pump duration), the MI bandwidth is 76 nm and the C_v is 0.75, comparable to the MI bandwidth of ≈ 60 nm and the C_v of 0.88 of the spontaneous MI spectra. Note that the differences between the experimental and simulation results can be explained due to the fact that the noise model used in the simulations can not be completely identical to the experimental noise of the pump or seed.

The dependence of the MI to the spectral bandwidth of the partially-coherent seed, in a way is similar to the study of MI for narrow-banded random waves developed by Alber in 1978 in the context of hydrodynamics (see Section 2.3.2) [135]. In this context, he showed that the parameter characterising the instability known as Benjamin-Feir index BFI, is essentially the ratio of the correlation to modulation length (Eq. 2.12). In optics, similar formulation of BFI for partially coherent optical wave has also been derived in Ref. [170] (Eq. 2.27), showing the suppression of MI for spectrum with bandwidth larger than the modulation frequency at maximum MI gain. In both cases, the instability is shown to be suppressed by the wave randomness characterised by the spectral bandwidth, which is similar to what we observe here. However, it is important to notice that in our case, the randomness is introduced by the perturbation (the seed) instead of the pump wave.

6.4 Conclusions

In this chapter, we study the spectral properties of stimulated MI on picosecond pulses triggered by low amplitude coherent and partially-coherent seed in a highly nonlinear fibre. In the first part of the chapter, we compare the spectral broadening and the shot-to-shot (pulse-to-pulse) spectral fluctuations of spontaneous MI, CW seeded MI and filtered ASE seeded MI obtained from stochastic numerical simulations. We show that significantly larger bandwidth and noise suppression characterised by lower value of coefficient of variation C_v are observed in the case of coherent and partially coherent seeded MI, where the profile of the C_v across the wavelengths of the spectrum is similar to the profile of the spectrum itself.

We also perform a detailed statistical analysis of the simulated spectral fluctuations taken at the MI sidebands and at the peaks of SPM-broadened pump spectra. In both cases, we show that highly skewed spectral intensity distributions of spontaneous MI spectra are transformed to symmetric Gaussian-like distributions for CW seeded MI spectra and superposition profile distributions for ASE seeded MI spectra. We have also shown that the statistics taken at the peaks of the SPM-broadened pump spectra is negatively-correlated with the statistics of the MI sidebands, indicating the power interchange between the pump and the MI sidebands. Further analysis of the spectral fluctuations has also been presented using higher order statistical moments taken across all wavelengths of the spectrum.

In the second part of the chapter, we investigate the influence of partially-coherent ASE seed on the bandwidth and noise properties of the MI spectra, through both experiments and numerical simulations. The shot-to-shot real-time spectral measurements are realised using dispersive time stretching method. Experiments varying the wavelength of the ASE seed across the MI gain spectrum show significant increase in the spectral bandwidth and noise reduction with maximum effects observed when the seed coincides with the modulation frequency of the maximum MI gain. Experiments varying the ASE bandwidth show that the influence of the ASE seed decreases with the increase of the ASE bandwidth, which is associated with shorter coherence time in comparison with the duration of the pump pulses. These results highlight the importance of a stable amplitude modulation for an effective seeding MI.

The MI spectra studied here are taken at the initial stage of long-pulse propagation (in the MI regime), therefore the results may have an impact on the general study of rogue waves generated from modulation instability. Additionally, it may also contribute to the study of supercontinuum generation from high-power pump sources, where a filtered ASE seed could still be an important tool to control the spectral properties of the supercontinuum.

Chapter 7

Conclusions and discussions

7.1 Conclusions

The study of optical rogue waves was first motivated by the analogy found between the propagation of light in optics and the propagation of water waves in the ocean, based on the similarity of the propagation equation governing both systems, i.e. the nonlinear Schrödinger equation (NLSE). In this context, the experimental studies of rogue waves in optical systems were performed in order to understand the infamous giant waves that appear and disappear without trace in the ocean. Indeed, an empirical study of oceanic rogue waves is a difficult task due to the vastness of the system, and therefore they are commonly studied only through theoretical (or numerical) approach or by means of wave tank experiments. The analogy found between the two systems therefore opened up the possibility to study this phenomenon by means of optical experiments which can be realised much more conveniently.

Various experimental realisations have been conducted in different optical systems, with or without the analogy with oceanic rogue waves. Optical rogue waves have therefore become an independent area of study, and many particular applications have been identified within the field of optics itself. The understanding of rogue wave formation from modulation instability for example, can be beneficial to the enhancement of supercontinuum generation, or the understanding of the mechanism causing spontaneous emission of very intense pulses in fibre optics can be beneficial in data communication. Understanding the generation of optical rogue waves possessing extremely high intensity field and at the same time highly confined in space and/or time is clearly a topic with many applications in optics.

In contrast to the broader definition of optical rogue waves, we focussed in this thesis only on particular optical systems which (under certain conditions) possess a close analogy with the phenomena of rogue waves in the ocean. To this end, we first presented in Chapter 2 the generating mechanisms of rogue waves known in both oceanography and optics, showing that similar linear and nonlinear mechanisms can be found in both systems. We then explored several possibilities to study these mechanisms in terms of optical systems. In the case of linear generating mechanisms, we investigated in Chapter 3 the role of spatial (geometrical) focussing which is also known as caustics. Whilst in the case of nonlinear generating mechanisms, we performed in Chapter 4 to 6

a series of numerical and experimental studies of rogue waves in an optical fibre system, where the propagation of light is governed by the NLSE.

Chapter 2 began with an introduction to the definition and statistical properties of rogue waves in general. In this part, we highlighted that although the terminology rogue waves clearly refers to extreme events that occur unexpectedly, an ambiguity on the specific definition of this term distinguishing it from the general definition of extreme events, still persists. In particular, the deviation of a statistical distribution from Gaussian wave statistics is in fact not an established criteria for a system exhibiting rogue waves. In this case, the classification of rogue waves is only based on the criteria of events having some quantity of interest (amplitude in oceanography, or intensity in optics) exceeding a certain (somewhat arbitrary) threshold. In the second part of this chapter, we discussed some possible generating mechanisms of rogue waves known in oceanography and optics, categorised into linear or nonlinear mechanisms. For the linear mechanisms, rogue waves can be formed by a spatial (geometrical) focussing or spatio-temporal (dispersive) focussing, whilst for the nonlinear mechanisms, rogue waves are often associated with the modulation instability. We showed that the similarity between these generating mechanisms in both systems allows (under certain circumstances) the study of rogue waves in one system by means of the other.

Linear mechanisms of rogue wave formation were addressed in Chapter 3, where the results were linked specifically to spatial focussing (caustic formation) discussed in Chapter 2 (Section 2.3 and 2.4). Using a free space propagation optical system, we showed that a random phase modulation of an optical beam can lead to the focussing of light into certain regions in space, forming high intensity localised light. In the first part of the chapter, we studied the two-dimensional evolution of a beam profile modulated only along one spatial direction, allowing a direct comparison of the results with the two-dimensional linear propagation of water waves. Whilst in the second part, we studied the three-dimensional evolution of a beam profile modulated in its two transverse directions. In this case, the formation of rogue waves is associated with the formation of caustic network in the initial stage of the light propagation. Additionally, we also showed that the optical system used in this experiment allows the generation of a spatial beam profile with field variation similar to the random two-dimensional ocean waves, where the elevation statistics follows Gaussian distribution and the wave height statistics follows Rayleigh distribution.

The nonlinear mechanisms of rogue wave formation are often associated with the phenomenon of modulation instability (MI), a wave amplification process leading to an exponential growth of a periodic perturbation on a continuous wave (CW) background. In this context, the propagation of ocean waves in deep water regime is analogous with the propagation of light in an optical fibre through the validity of the NLSE governing both systems. In order to study the spontaneous emergence of rogue waves due to a noise induced MI, we performed in Chapter 4 a detailed numerical study simulating the spatio-temporal evolution of a noise perturbed CW governed by the NLSE. We showed that the spontaneously emerged localised structures in the chaotic MI field can be described in terms of the analytical solutions of the NLSE in the form of "breather" or "soliton on finite background" (SFB) solutions. The correlation between the emergence of higher-order breathers and the broadening of the spectrum was then also reported, suggesting that the collision of breathers occurred at a certain distance along the propagation can be detected from the spectral width measured at that particular distance. Furthermore, we performed various statistical

analysis on the spontaneously emergent breathers and specifically highlighted that Peregrine soliton is not statistically rare enough to be considered as a rogue wave in a system governed by the NLSE.

The experimental realisation of spontaneous MI in an optical fibre was shown in Chapter 5. Using a time-lens magnifier system, the ultrafast temporal dynamics of the MI could be measured and the temporal breather structures could be characterised in real time. The experimental results shown in this chapter confirm the simulation results, showing that the SFB solutions indeed provides a natural basis to describe the localised structures emerged in a chaotic MI field. The statistical analysis of the measured peak intensities in the chaotic MI regime has also been shown to reproduce the statistics obtained from the simulation, confirming the association of statistical rogue waves exclusively to the higher-order breathers.

In contrast to Chapters 4 and 5, we studied in Chapter 6 the stimulated MI induced by coherent and partially-coherent wave. The purpose of this study was to investigate the role of wave coherence in the MI process, by examining the spectral properties of the stimulated MI on picosecond pulses. The real-time spectral measurement was realised using the dispersive Fourier transform technique, where the intensity profile of the pulses evolves into their spectral profile after being stretched in time by long dispersive propagation. We first showed that the broadening of the spectrum is dependent on the wavelength of the seed used to trigger the MI, which corresponds to the gain curve of the MI. Then, from the statistical analysis of these spectra, we showed that the fluctuations of the MI spectral sidebands are suppressed when the MI is seeded by coherent or partially-coherent wave. In the latter case, we also examined the effect of partially-coherent bandwidth, showing that both the spectral broadening and the noise suppression are diminished by the increase of the bandwidth of the partially-coherent seed.

In conclusion, we have investigated several optical systems exhibiting rogue wave behaviour, from where some analogies with the oceanic counterparts can be drawn (under certain circumstances). Through the optical simulations and experiments performed in this thesis, we have shown that further insight on both oceanic and optical rogue wave generating mechanisms can be gained. Specifically, by showing that optical rogue waves can be formed by both linear and nonlinear processes, we suggest that both mechanisms should be considered to play role in the generation of rogue waves in the ocean.

7.2 Discussions

As mentioned earlier, the definition of rogue waves is sometimes not distinguishable from a more general definition of extreme events. In some cases, the term rogue wave specifically refers to a system exhibiting heavy-tail statistics (deviation from Gaussian distribution) [17, 28], while in other cases, the criteria used is based only on certain statistical threshold [13, 14]. Due to the variety of the statistical analysis performed in the course of this thesis, we use here a simpler definition of rogue waves based on a certain threshold. In addition, we also want to emphasise here that the comparison of the statistics with Gaussian distribution should be adapted according to the quantity under study. The statistics of wave height for example, should be compared to Rayleigh distribution, and the statistics of wave intensity should be compared to an exponential distribution.

The role of linear and nonlinear effects on the formation of rogue waves is highlighted in this thesis in relation to the debate of whether nonlinearity is an absolute requirement for the generation of these giant waves appearing with probability higher than predicted by Gaussian distribution [28, 280]. Here we have shown that optical rogue waves can be formed by both linear and nonlinear mechanisms, and based on the analogy drawn to the ocean wave, we suggest that both effects also play an important role in the formation of oceanic rogue waves. These two effects can then act separately or interact in a certain way. In the latter case, the linear focussing can act for example as a trigger for the nonlinear effects [4, 107, 281].

One of the main challenge in this study is the lack of reliable measurement data of ocean waves. In particular, long-term wave time series measurements and space-time measurements are needed for the advancement of the study. Without these field measurement data, the real mechanisms of rogue wave formation could not be fully understood and a meaningful statistical comparison could not be made.

We have also shown in this thesis that the properties of oceanic rogue waves can be studied meaningfully by means of optical experiments, as long as a clear analogy between the two systems can be made. However, these analogies are valid only under certain conditions, and consequently the results obtained from this study is also limited only within this scope. Nevertheless, there are still many other optical experiments can be explored in this area and the progress made in any of these systems can always enforce the understanding and the development of rogue wave study in another system. Below we propose some recommendation for future work, which can be realised in the near future.

A linear focussing study similar to the one shown in Section 3.2 can also be studied in an optical fibre system. It can be realised by randomly modulating (with relatively long period) the phase of weak intensity chirped pulses and passing it through an optical fibre. In this case, the rogue waves will then be formed at random times along the pulses due to the dispersive focussing mechanism (instead of the spatial focussing).

The real-time temporal measurements allows the characterisation of ultrafast temporal dynamics. This technique can therefore be applied to many other optical rogue wave studies which were only measured before by the real-time spectral measurements, such as the study of stimulated MI reported in Chapter 6. In this case, the effect of noise stabilisation to the shot-to-shot temporal structures can also be studied.

To date, a real-time spatio-temporal characterisation of spontaneously emerging breather structures has not yet been realised. In optical fibre, cutback method can only be used for characterisation of pulses with repetitive temporal profile. Further research on the experimental realisation is therefore needed in order to gain better understanding on the two-dimensional nature of rogue waves.

Bibliography

[1] Adcock, T.A.A., Taylor, P.H., Yan, S., Ma, Q.W. & Janssen, P.A.E.M. Did the Draupner wave occur in a crossing sea? *Proceedings of the Royal Society A* 467, 3004–3021 (2011).

[2] Mori, N., Liu, P.C. & Yasuda, T. Analysis of freak wave measurements in the Sea of Japan. *Ocean Engineering* 29, 1399–1414 (2002).

[3] Hadjihosseini, A., Peinke, J. & Hoffmann, N.P. Stochastic analysis of ocean wave states with and without rogue waves. *New Journal of Physics* 16, 053037 (2014).

[4] Heller, E. Freak ocean waves and refraction of Gaussian seas. *Extreme Events in Nature and Society*. Springer Berlin Heidelberg, 189–210 (2006).

[5] Arecchi, F.T., Bortolozzo, U., Montina, A. & Residori, S. Granularity and inhomogeneity are the joint generators of optical rogue waves. *Physical Review Letters* 106, 153901 (2011).

[6] Dudley, J.M., Dias, F., Erkintalo, M. & Genty, G. Instabilities, breathers and rogue waves in optics. *Nature Photonics* 8, 755–764 (2014).

[7] Akhmediev, N., Soto-Crespo, J.M. & Ankiewicz, A. Extreme waves that appear from nowhere: On the nature of rogue waves. *Physics Letters A* 373, 2137–2145 (2009).

[8] Salem, R., Foster, M.A. & Gaeta, A.L. Application of space-time duality to ultrahigh-speed optical signal processing. *Advances in Optics and Photonics* 5, 274–317 (2013).

[9] Juran, J.M. Pareto, Lorenz, Cournot, Bernoulli, Juran and Others. *Industrial Quality Control* 17, 25 (1960).

[10] Pareto, V. *Manual of political economy*. Macmillan (1971).

[11] Hardy, M. Pareto's Law. *The Mathematical Intelligencer* 32, 38–43 (2010).

[12] Bryson, M. Heavy-tailed distributions: properties and tests. *Technometrics* 16, 61–68 (1974).

[13] Kharif, C. & Pelinovsky, E. Physical mechanisms of the rogue wave phenomenon. *European Journal of Mechanics-B/Fluids* 22, 603–634 (2003).

[14] Dysthe, K., Krogstad, H.E. & Müller, P. Oceanic Rogue Waves. *Annual Review of Fluid Mechanics* 40, 287–310 (2008).

[15] Kharif, C., Touboul, J. & Slunyaev, A. *Rogue Waves in the Ocean*. Springer Berlin Heidelberg (2009).

[16] Slunyaev, A., Didenkulova, I. & Pelinovsky, E. Rogue waters. *Contemporary Physics* 52, 571–590 (2011).

[17] Adcock, T.A.A. & Taylor, P.H. The physics of anomalous ('rogue') ocean waves. *Reports on Progress in Physics* 77, 105901 (2014).

[18] Akhmediev, N., Ankiewicz, A. & Taki, M. Waves that appear from nowhere and disappear without a trace. *Physics Letters A* 373, 675–678 (2009).

[19] Haver, S. A possible freak wave event measured at the Draupner jacket January 1 1995. *Rogue waves 2004 : proceedings of a workshop organized by Ifremer and held in Brest, France.* Ifremer, France, 1–8 (2004).

[20] Onorato, M., Residori, S., Bortolozzo, U., Montina, A. & Arecchi, F.T. Rogue waves and their generating mechanisms in different physical contexts. *Physics Reports* 528, 47–89 (2013).

[21] Christou, M. & Ewans, K. Field Measurements of Rogue Water Waves. *Journal of Physical Oceanography* 44, 2317–2335 (2014).

[22] Stenflo, L. & Marklund, M. Rogue waves in the atmosphere. *Journal of Plasma Physics* 76, 293–295 (2010).

[23] Moslem, W.M., Shukla, P.K. & Eliasson, B. Surface plasma rogue waves. *EPL (Europhysics Letters)* 96, 25002 (2011).

[24] Bludov, Y.V., Konotop, V.V. & Akhmediev, N. Matter rogue waves. *Physical Review A* 80, 033610 (2009).

[25] Höhmann, R., Kuhl, U., Stöckmann, H.J., Kaplan, L. & Heller, E.J. Freak waves in the linear regime: A microwave study. *Physical Review Letters* 104, 093901 (2010).

[26] Solli, D.R., Ropers, C., Koonath, P. & Jalali, B. Optical rogue waves. *Nature* 450, 1054–1057 (2007).

[27] The power of analogies. *Nature Photonics* 8, 1 (2013).

[28] Ruban, V., Kodama, Y., Ruderman, M., Dudley, J., Grimshaw, R., McClintock, P.V.E., Onorato, M., Kharif, C., Pelinovsky, E., Soomere, T., Lindgren, G., Akhmediev, N., Slunyaev, A., Solli, D., Ropers, C., Jalali, B., Dias, F. & Osborne, A. Rogue waves - towards a unifying concept?: Discussions and debates. *European Physical Journal: Special Topics* 185, 5–15 (2010).

[29] Kumar, C., Gupta, R., Goyal, A., Loomba, S., Raju, T. & Panigrahi, P. Controlled giant rogue waves in nonlinear fiber optics. *Physical Review A* 86, 025802 (2012).

[30] Dudley, J.M., Genty, G. & Eggleton, B.J. Harnessing and control of optical rogue waves in supercontinuum generation. *Optics Express* 16, 3644–3651 (2008).

[31] Solli, D.R., Ropers, C. & Jalali, B. Active control of rogue waves for stimulated supercontinuum generation. *Physical Review Letters* 101, 18–21 (2008).

[32] Bromberg, Y. & Cao, H. Generating non-rayleigh speckles with tailored intensity statistics. *Physical Review Letters* 112, 213904 (2014).

[33] Marsal, N., Caullet, V., Wolfersberger, D. & Sciamanna, M. Spatial rogue waves in a photorefractive pattern-forming system. *Optics Letters* 39, 3690–3693 (2014).

[34] McCabe, D.J., Tajalli, A., Austin, D.R., Bondareff, P., Walmsley, I.A., Gigan, S. & Chatel, B. Spatio-temporal focusing of an ultrafast pulse through a multiply scattering medium. *Nature Communications* 2, 447 (2011).

[35] Liu, C., van der Wel, R.E.C., Rotenberg, N., Kuipers, L., Krauss, T.F., Di Falco, A. & Fratalocchi, A. Triggering extreme events at the nanoscale in photonic seas. *Nature Physics* 11, 358–363 (2015).

[36] Draper, L. 'Freak'ocean waves. *Weather* 21, 2–4 (1964).

[37] Henderson, K., Peregrine, D. & Dold, J. Unsteady water wave modulations: fully nonlinear solutions and comparison with the nonlinear Schrödinger equation. *Wave Motion* 29, 341–361 (1999).

[38] Liu, P.C.P. A chronology of freauqe wave encounters. *Geofizika* 24, 57–70 (2007).

[39] Cartwright, J.H.E. & Nakamura, H. What kind of a wave is Hokusai's Great wave off Kanagawa? *Notes and Records of the Royal Society* 63, 119–135 (2009).

[40] Dudley, J.M., Sarano, V. & Dias, F. On Hokusai's Great wave off Kanagawa: localization, linearity and a rogue wave in sub-Antarctic waters. *Notes and records of the Royal Society of London* 67, 159–164 (2013).

[41] Bitner-Gregersen, E.M. & Magnusson, A.K. Extreme events in field data and in a second order wave model. *Rogue waves 2004 : proceedings of a workshop organized by Ifremer and held in Brest, France*. Ifremer, France, 20–22 (2004).

[42] Guedes Soares, C., Cherneva, Z. & Antao, E.M. Characteristics of abnormal waves in North Sea storm sea states. *Applied Ocean Research* 25, 337–344 (2003).

[43] de Pinho, U., Liu, P. & Ribeiro, C. Freak waves at Campos basin, Brazil. *Geofizika* 21, 53–67 (2004).

[44] Toffoli, A., Lefèvre, J.M., Bitner-Gregersen, E. & Monbaliu, J. Towards the identification of warning criteria: Analysis of a ship accident database. *Applied Ocean Research* 27, 281–291 (2005).

[45] Forristall, G.Z., Barstow, S.F., Krogstad, H.E., Taylor, P.H. & Tromans, P.S. Wave crest sensor intercomparison study: an overview of WACSIS. *Journal of Offshore Mechanics and Arctic Engineering* 126, 26–34 (2004).

[46] Lehner, S.H. & Gunther, H. Extreme wave statistics from radar data sets. *Proceedings of Geoscience and Remote Sensing Symposium, 2004. IGARSS'04*, volume 3. IEEE International, 1880–1883 (2004).

[47] Janssen, P. & Alpers, W. Why SAR wave mode data of ERS and Envisat are inadequate for giving the probability of occurrence of freak waves. *Proceedings of the SEASAR 2006 Workshop, ESA/ESRIN*, 613. 23–26 (2006).

[48] Fedele, F., Brennan, J., De León, S.P., Dudley, J. & Dias, F. Real world ocean rogue waves explained without the modulational instability. *Proceedings of Ocean and Polar Engineering Conference*. International Society of Offshore and Polar Engineers (2016).

[49] Benetazzo, A., Fedele, F., Gallego, G., Shih, P.C. & Yezzi, A. Offshore stereo measurements of gravity waves. *Coastal Engineering* 64, 127–138 (2012).

[50] Fedele, F. Space-time extremes in short-crested storm seas. *Journal of Physical Oceanography* 42, 1601–1615 (2012).

[51] Fedele, F., Benetazzo, A., Gallego, G., Shih, P.C., Yezzi, A., Barbariol, F. & Ardhuin, F. Space-time measurements of oceanic sea states. *Ocean Modelling* 70, 103–115 (2013).

[52] Ganshin, A.N., Efimov, V.B., Kolmakov, G.V., Mezhov-Deglin, L.P. & McClintock, P.V.E. Observation of an inverse energy cascade in developed acoustic turbulence in superfluid helium. *Physical Review Letters* 101, 065303 (2008).

[53] Shats, M., Punzmann, H. & Xia, H. Capillary rogue waves. *Physical Review Letters* 104, 104503 (2010).

[54] Bailung, H., Sharma, S. & Nakamura, Y. Observation of Peregrine solitons in a multicomponent plasma with negative ions. *Physical Review Letters* 107, 255005 (2011).

[55] Laveder, D., Passot, T., Sulem, P. & Sánchez-Arriaga, G. Rogue waves in Alfvénic turbulence. *Physics Letters A* 375, 3997–4002 (2011).

[56] Sverdrup, H. & Munk, W. *Wind, Sea, and Swell: Theory of Relations for Forecasting*. Hydrographic Office and the Supt. of Docs. (1947).

[57] Metzger, J.J., Fleischmann, R. & Geisel, T. Intensity fluctuations of waves in random media: What is the semiclassical limit? *Physical Review Letters* 111, 013901 (2013).

[58] Birkholz, S., Brée, C., Demircan, A. & Steinmeyer, G. Predictability of Rogue Events. *Physical Review Letters* 114, 213901 (2015).

[59] Bitner-Gregersen, E.M. & Toffoli, A. On the probability of occurrence of rogue waves. *Natural Hazards and Earth System Science* 12, 751–762 (2012).

[60] Bacon, S. Wind Waves. P. Bruce (Editor) *Heavy weather sailing*, chapter Wind waves. Bloomsbury Publishing, 4th edition (1991).

[61] Sand, S.E., Hansen, N.E.O., Klinting, P., Gudmestad, O.T. & Sterndorff, M.J. Freak wave kinematics. *Water Wave Kinematics*, volume 178. Kluwer, 535–549 (1990).

[62] White, B.S. & Fornberg, B. On the chance of freak waves at sea. *Journal of Fluid Mechanics* 355, 113–138 (1998).

[63] Haver, S. Freak waves: a suggested definition and possible consequences for marine structures. *Rogue waves 2004 : proceedings of a workshop organized by Ifremer and held in Brest, France*. Ifremer, France (2004).

[64] Longuet-Higgins, M. On the statistical distributions of sea waves. *Journal of Marine Research* 11, 245–265 (1952).

[65] Longuet-Higgins, M.S. The Statistical Analysis of a Random, Moving Surface. *Philosophical Transactions of the Royal Society of London A* 249, 321–387 (1957).

[66] Earle, M.D. Extreme wave conditions during Hurricane Camille. *Journal of Geophysical Research* 80, 377 (1975).

[67] Yasuda, T. & Mori, N. Occurrence properties of giant freak waves in sea area around Japan. *Journal of Waterway, Port, Coastal, and Ocean Engineering* 123, 209–213 (1997).

[68] Christou, M. & Ewans, K. Examining a Comprehensive Dataset Containing Thousands of Freak Wave Events. *Structures, Safety and Reliability* 2, 827–837 (2011).

[69] Stansell, P. Distributions of fAreak wave heights measured in the North Sea. *Applied Ocean Research* 26, 35–48 (2004).

[70] Onorato, M., Osborne, A.R., Serio, M. & Bertone, S. Freak waves in random oceanic sea states. *Physical Review Letters* 86, 5831–5834 (2001).

[71] Onorato, M., Osborne, A.R., Serio, M. & Damiani, T. Occurrence of Freak Waves from Envelope Equations in Random Ocean Wave Simulations. *Rogue waves 2000 : proceedings of a workshop organized by Ifremer and held in Brest, France.* Ifremer, France, 181–191 (2000).

[72] Haring, R., Osborne, A. & Spencer, L. Extreme wave parameters based on continental shelf storm wave records. *Coastal Engineering* 1, 151–170 (1976).

[73] Forristall, G.Z. On the statistical distribution of wave heights in a storm. *Journal of Geophysical Research* 83, 2353 (1978).

[74] Tayfun, B.M.A. & Tayfun, M. Distribution of large wave heights. *Journal of Waterway, Port, Coastal, and Ocean Engineering* 116, 686–707 (1990).

[75] Birkholz, S., Brée, C., Veselić, I., Demircan, A. & Steinmeyer, G. Random walks across the sea: the origin of rogue waves? *arXiv:1507.08102* (2015).

[76] Prat, M.C. *Overview of ocean wave statistics.* Ph.D. thesis, Universitat Politècnica de Catalunya (2008).

[77] Montina, A., Bortolozzo, U., Residori, S. & Arecchi, F.T. Non-gaussian statistics and extreme waves in a nonlinear optical cavity. *Physical Review Letters* 103, 173901 (2009).

[78] Randoux, S., Walczak, P., Onorato, M. & Suret, P. Intermittency in integrable turbulence. *Physical Review Letters* 113, 113902 (2014).

[79] Agafontsev, D.S. & Zakharov, V.E. Integrable turbulence and formation of rogue waves. *Nonlinearity* 28, 2791–2821 (2015).

[80] Kasparian, J., Béjot, P., Wolf, J.P. & Dudley, J.M. Optical rogue wave statistics in laser filamentation. *Optics Express* 17, 12070–12075 (2009).

[81] Demircan, A., Amiranashvili, S., Brée, C., Mahnke, C., Mitschke, F. & Steinmeyer, G. Rogue events in the group velocity horizon. *Scientific reports* 2, 850 (2012).

[82] Birkholz, S., Nibbering, E.T.J., Brée, C., Skupin, S., Demircan, A., Genty, G. & Steinmeyer, G. Spatiotemporal rogue events in optical multiple filamentation. *Physical Review Letters* 111, 243903 (2013).

[83] Demircan, A., Amiranashvili, S., Brée, C., Mahnke, C., Mitschke, F. & Steinmeyer, G. Rogue wave formation by accelerated solitons at an optical event horizon. *Applied Physics B* 115, 343–354 (2014).

[84] Leonetti, M. & Conti, C. Observation of three dimensional optical rogue waves through obstacles. *Applied Physics Letters* 106, 254103 (2015).

[85] Bonatto, C., Feyereisen, M., Barland, S., Giudici, M., Masoller, C., Leite, J.R.R. & Tredicce, J.R. Deterministic optical rogue waves. *Physical Review Letters* 107, 053901 (2011).

[86] Lecaplain, C., Grelu, P., Soto-Crespo, J.M. & Akhmediev, N. Dissipative rogue waves generated by chaotic pulse bunching in a mode-locked laser. *Physical Review Letters* 108, 233901 (2012).

[87] Bonazzola, C., Hnilo, A., Kovalsky, M. & Tredicce, J.R. Optical rogue waves in an all-solid-state laser with a saturable absorber: importance of the spatial effects. *Journal of Optics* 15, 064004 (2013).

[88] Zamora-Munt, J., Garbin, B., Barland, S., Giudici, M., Leite, J.R.R., Masoller, C. & Tredicce, J.R. Rogue waves in optically injected lasers: Origin, predictability, and suppression. *Physical Review A* 87, 035802 (2013).

[89] Pierangeli, D., Di Mei, F., Conti, C. & DelRe, E. Evidence of the universal dynamics of rogue waves. *arXiv:1511.01390* (2015).

[90] Hammani, K., Finot, C., Dudley, J.M. & Millot, G. Optical rogue-wave-like extreme value fluctuations in fiber Raman amplifiers. *Optics Express* 16, 16467–16474 (2008).

[91] Genty, G., de Sterke, C.M., Bang, O., Dias, F., Akhmediev, N. & Dudley, J.M. Collisions and turbulence in optical rogue wave formation. *Physics Letters A* 374, 989–996 (2010).

[92] Solli, D.R., Ropers, C. & Jalali, B. Measuring single-shot modulation instability and supercontinuum spectra at megahertz rates. *Nonlinearity* 26, R85–R92 (2013).

[93] Walczak, P., Randoux, S. & Suret, P. Optical Rogue Waves in Integrable Turbulence. *Physical Review Letters* 114, 143903 (2015).

[94] Foss, S., Korshunov, D. & Zachary, S. *An Introduction to Heavy-Tailed and Subexponential Distributions*. Springer Science and Business Media (2013).

[95] Holthuijsen, L. *Waves in oceanic and coastal waters*. Cambridge University Press (2007).

[96] Tomita, H. & Kawamura, T. Statistical analysis and inference from the in-situ data of the Sea of Japan with reference to abnormal and/or freak waves. *Proceedings of Offshore and Polar Engineering Conference*. International Society of Offshore and Polar Engineers (2000).

[97] Guedes Soares, C., Cherneva, Z. & Antao, E.M. Abnormal waves during Hurricane Camille. *Journal of Geophysical Research: Oceans* 109 (2004).

[98] Janssen, P.A.E.M. Nonlinear Four-Wave Interactions and Freak Waves. *Journal of Physical Oceanography* 33, 863–884 (2003).

[99] Mori, N. & Janssen, P.A.E.M. On Kurtosis and Occurrence Probability of Freak Waves. *Journal of Physical Oceanography* 36, 1471–1483 (2006).

[100] Fedele, F. On the kurtosis of deep-water gravity waves. *Journal of Fluid Mechanics* 782, 25–36 (2015).

[101] DeCarlo, L.T. On the meaning and use of kurtosis. *Psychological Methods* 2, 292–307 (1997).

[102] Erkintalo, M., Genty, G. & Dudley, J.M. On the statistical interpretation of optical rogue waves. *European Physical Journal: Special Topics* 185, 135–144 (2010).

[103] Zaviyalov, A., Egorov, O., Iliew, R. & Lederer, F. Rogue waves in mode-locked fiber lasers. *Physical Review A* 85, 013828 (2012).

[104] Peregrine, D.H. Interaction of Water Waves and Currents. *Advances in Applied Mechnaics* 16, 9–117 (1976).

[105] Smith, R. Giant waves. *Journal of Fluid Mechanics* 77, 417 (1976).

[106] Lavrenov, I.V. The wave energy concentration at the Agulhas Current off South Africa. *Natural Hazards* 17, 117–127 (1998).

[107] Heller, E.J., Kaplan, L. & Dahlen, A. Refraction of a Gaussian seaway. *Journal of Geophysical Research: Oceans* 113 (2008).

[108] Brown, M.G. Space-time surface gravity wave caustics: Structurally stable extreme wave events. *Wave Motion* 33, 117–143 (2001).

[109] Rapp, R.J. & Melville, W.K. Laboratory Measurements of Deep-Water Breaking Waves. *Philosophical Transactions of the Royal Society A* 331, 735–800 (1990).

[110] Toffoli, A., Babanin, A., Onorato, M. & Waseda, T. Maximum steepness of oceanic waves: Field and laboratory. *Geophysical Research Letters* 37 (2010).

[111] Benney, D.J. & Newell, A.C. The Propagation of Nonlinear Wave Envelopes. *Journal of Mathematics and Physics* 46, 133–139 (1967).

[112] Whitham, G.B. *Linear and nonlinear waves.* John Wiley & Sons (1975).

[113] Zakharov, V.E. Stability of periodic waves of finite amplitude on the surface of a deep fluid. *Journal of Applied Mechanics and Technical Physics* 9, 190–194 (1968).

[114] Osborne, A.R. The random and deterministic dynamics of 'rogue waves' in unidirectional, deep-water wave trains. *Marine Structures* 14, 275–293 (2001).

[115] Zakharov, V. & Shabat, A. Exact theory of two-dimensional self-focusing and one-dimensional self-modulation of waves in nonlinear media. *Soviet Physics JETP* 34, 62 (1972).

[116] Osborne, A.R., Onorato, M. & Serio, M. Nonlinear Fourier analysis of deep-water , random surface waves : theoretical formulation and experimental observations of rogue waves experimentally. *Proceedings of 14th Aha Huliko a Winter Workshop* (2005).

[117] Islas, A. & Schober, C. Predicting rogue waves in random oceanic sea states. *Physics of Fluids* 17, 031701 (2005).

[118] Slunyaev, A. Nonlinear analysis and simulations of measured freak wave time series. *European Journal of Mechanics-B/Fluids* 25, 621–635 (2006).

[119] Andonowati, Karjanto, N. & van Groesen, E. Extreme wave phenomena in down-stream running modulated waves. *Applied Mathematical Modelling* 31, 1425–1443 (2007).

[120] Huijsmans, R., Klopman, G. & Karjanto, N. Experiments on extreme wave generation using the soliton on finite background. *arXiv:1110.5119* (2011).

[121] Onorato, M., Osborne, A.R., Serio, M., Cavaleri, L., Brandini, C. & Stansberg, C.T. Observation of strongly non-Gaussian statistics for random sea surface gravity waves in wave flume experiments. *Physical Review E* 70, 67302 (2004).

[122] Zakharov, V.E. & Ostrovsky, L.A. Modulation instability: The beginning. *Physica D* 238, 540–548 (2009).

[123] Taniuti, T. & Washimi, H. Self-Trapping and Instability of Hydromagnetic Waves Along the Magnetic Field in a Cold Plasma. *Physical Review Letters* 21, 209–212 (1968).

[124] Watanabe, S. Self-modulation of a nonlinear ion wave packet. *Journal of Plasma Physics* 17, 487 (2009).

[125] Bailung, H. & Nakamura, Y. Observation of modulational instability in a multi-component plasma with negative ions. *Journal of Plasma Physics* 50, 231 (2009).

[126] Bespalov, V.V. & Talanov, V.V. Filamentary Structure of Light Beams in Nonlinear Media. *JETP Letters* 3, 307–310 (1966).

[127] Tai, K., Hasegawa, A. & Tomita, A. Observation of modulational instability in optical fibers. *Physical Review Letters* 56, 135–138 (1986).

[128] Salasnich, L., Parola, A. & Reatto, L. Modulational instability and complex dynamics of confined matter-wave solitons. *Physical Review Letters* 91, 080405 (2003).

[129] Lighthill, M.J. Contributions to the Theory of Waves in Non-linear Dispersive Systems. *IMA Journal of Applied Mathematics* 1, 269–306 (1965).

[130] Whitham, G.B. A general approach to linear and non-linear dispersive waves using a Lagrangian. *Journal of Fluid Mechanics* 22, 273–283 (1965).

[131] Benjamin, T.B. & Feir, J.E. The disintegration of wave trains on deep water Part 1. Theory. *Journal of Fluid Mechanics* 27, 417 (1967).

[132] Benjamin, T.B. & Hasselmann, K. Instability of Periodic Wavetrains in Nonlinear Dispersive Systems [and discussion]. *Proceedings of the Royal Society A* 299, 59–76 (1967).

[133] Whitham, G.B. Non-linear dispersion of water waves. *Journal of Fluid Mechanics* 27, 399–412 (1967).

[134] Yuen, H. & Lake, B. Nonlinear dynamics of deep-water gravity waves. *Advances in Applied Mechanics* 22, 67–229 (1982).

[135] Alber, I.E. The Effects of Randomness on the Stability of Two-Dimensional Surface Wavetrains. *Proceedings of the Royal Society A* 363, 525–546 (1978).

[136] Majus, D., Jukna, V., Valiulis, G., Faccio, D. & Dubietis, A. Spatiotemporal rogue events in femtosecond filamentation. *Physical Review A* 83, 025802 (2011).

[137] Kibler, B., Fatome, J., Finot, C., Millot, G., Dias, F., Genty, G., Akhmediev, N. & Dudley, J.M. The Peregrine soliton in nonlinear fibre optics. *Nature Physics* 6, 790–795 (2010).

[138] Hammani, K., Wetzel, B., Kibler, B., Fatome, J., Finot, C., Millot, G., Akhmediev, N. & Dudley, J.M. Spectral dynamics of modulation instability described using Akhmediev breather theory. *Optics Letters* 36, 2140–2142 (2011).

[139] Kibler, B., Fatome, J., Finot, C., Millot, G., Genty, G., Wetzel, B., Akhmediev, N., Dias, F. & Dudley, J.M. Observation of Kuznetsov-Ma soliton dynamics in optical fibre. *Scientific Reports* 2, 463 (2012).

[140] Frisquet, B., Kibler, B. & Millot, G. Collision of Akhmediev breathers in nonlinear fiber optics. *Physical Review X* 3, 041032 (2014).

[141] Nguyen, D.M., Godin, T., Toenger, S., Combes, Y., Wetzel, B., Sylvestre, T., Merolla, J.M., Larger, L., Genty, G., Dias, F. & Dudley, J.M. Incoherent resonant seeding of modulation instability in optical fiber. *Optics letters* 38, 5338–5341 (2013).

[142] Dudley, J.M., Genty, G., Dias, F., Kibler, B. & Akhmediev, N. Modulation instability, Akhmediev Breathers and continuous wave supercontinuum generation. *Optics Express* 17, 21497–21508 (2009).

[143] Kelleher, E.J.R., Travers, J.C., Popov, S.V. & Taylor, J.R. Role of pump coherence in the evolution of continuous-wave supercontinuum generation initiated by modulation instability. *Journal of the Optical Society of America B* 29, 502 (2012).

[144] Toenger, S., Godin, T., Billet, C., Dias, F., Erkintalo, M., Genty, G. & Dudley, J.M. Emergent rogue wave structures and statistics in spontaneous modulation instability. *Scientific Reports* 5, 10380 (2015).

[145] Mussot, A., Kudlinski, A., Kolobov, M., Louvergneaux, E., Douay, M. & Taki, M. Observation of extreme temporal events in CW-pumped supercontinuum. *Optics Express* 17, 17010–17015 (2009).

[146] Taki, M., Mussot, A., Kudlinski, A., Louvergneaux, E., Kolobov, M. & Douay, M. Third-order dispersion for generating optical rogue solitons. *Physics Letters A* 374, 691–695 (2010).

[147] Erkintalo, M., Genty, G. & Dudley, J.M. Rogue-wave-like characteristics in femtosecond supercontinuum generation. *Optics Letters* 34, 2468–2470 (2009).

[148] Hammani, K., Finot, C. & Millot, G. Emergence of extreme events in fiber-based parametric processes driven by a partially incoherent pump wave. *Optics Letters* 34, 1138–1140 (2009).

[149] Borlaug, D., Fathpour, S. & Jalali, B. Extreme value statistics in silicon photonics. *IEEE Photonics Journal* 1, 33–39 (2009).

[150] Kovalsky, M.G., Hnilo, A.A. & Tredicce, J.R. Extreme events in the Ti:sapphire laser. *Optics Letters* 36, 4449–4451 (2011).

[151] Runge, A.F.J., Aguergaray, C., Broderick, N.G.R. & Erkintalo, M. Raman rogue waves in a partially mode-locked fiber laser. *Optics Letters* 39, 319–322 (2014).

[152] Randoux, S. & Suret, P. Experimental evidence of extreme value statistics in Raman fiber lasers. *Optics Letters* 37, 500–502 (2012).

[153] Lushnikov, P.M. & Vladimirova, N. Non-Gaussian statistics of multiple filamentation. *Optics Letters* 35, 1965–1967 (2010).

[154] Pierangeli, D., Di Mei, F., Conti, C., Agranat, A.J. & DelRe, E. Spatial Rogue Waves in Photorefractive Ferroelectrics. *Physical Review Letters* 115, 093901 (2015).

[155] Mathis, A., Froehly, L., Toenger, S., Dias, F., Genty, G. & Dudley, J.M. Caustics and Rogue Waves in an Optical Sea. *Scientific Reports* 5, 12822 (2015).

[156] Residori, S., Bortolozzo, U., Montina, A., Lenzini, F. & Arecchi, F.T. Rogue Waves in Spatially Extended Optical Systems. *Fluctuation and Noise Letters* 11, 1240014 (2012).

[157] Vergeles, S. & Turitsyn, S.K. Optical rogue waves in telecommunication data streams. *Physical Review A* 83, 061801 (2011).

[158] Vergeles, S. & Turitsyn, S.K. Reply to "Comment on 'Optical rogue waves in telecommunication data streams' ". *Physical Review A* 84, 067802 (2011).

[159] Akhmediev, N., Dudley, J.M., Solli, D.R. & Turitsyn, S.K. Recent progress in investigating optical rogue waves. *Journal of Optics* 15, 60201 (2013).

[160] Lantz, E. Comment on "Optical rogue waves in telecommunication data streams". *Physical Review A* 84, 67801 (2011).

[161] Talanov, V. Self-focusing of wave beams in nonlinear media. *JETP Letters* 2, 138–141 (1965).

[162] Agrawal, G. *Nonlinear fiber optics*. Academic Press (2007).

[163] Boyd, R. *Nonlinear optics*. Academic Press (2003).

[164] Erkintalo, M., Genty, G., Wetzel, B. & Dudley, J.M. Limitations of the linear Raman gain approximation in modeling broadband nonlinear propagation in optical fibers. *Optics Express* 18, 25449–25460 (2010).

[165] Ostrovskii, L.A. Electromagnetic waves in nonlinear media with dispersion. *Soviet Physics-Technical Physics* 8, 679–681 (1964).

[166] Ostrovskii, L.A. Propagation of wave packets and space-time self-focusing in a nonlinear medium. *Soviet Physics JETP* 24, 797–800 (1967).

[167] Zagryadskaya, L.I. & Ostrovskii, L.A. Observed self-influence of modulated waves in a nonlinear line. *Radiophysics and Quantum Electronics* 11, 548–550 (1968).

[168] Ostrovskii, L.A. & Soustov, L.V. "Selfmodulation" of electromagnetic waves in nonlinear transmission lines. *Radiophysics and Quantum Electronics* 15, 182–187 (1972).

[169] Hasegawa, A. & Brinkman, W. Tunable coherent IR and FIR sources utilizing modulational instability. *IEEE Journal of Quantum Electronics* 16, 694 – 697 (1980).

[170] Chabchoub, A., Kibler, B., Finot, C. & Millot, G. The nonlinear Schrödinger equation and the propagation of weakly nonlinear waves in optical fibers and on the water surface. *Annals of Physics* 361, 490–500 (2015).

[171] Sauter, A., Pitois, S., Millot, G. & Picozzi, A. Incoherent modulation instability in instantaneous nonlinear Kerr media. *Optics Letters* 30, 2143–2145 (2005).

[172] Dysthe, K.B. & Trulsen, K. Note on Breather Type Solutions of the NLS as Models for Freak-Waves. *Physica Scripta* T82, 48–52 (1999).

[173] Dyachenko, A.I. & Zakharov, V.E. Modulation instability of Stokes wave - freak wave. *Journal of Experimental and Theoretical Physics Letters* 81, 255–259 (2005).

[174] Shrira, V.I. & Geogjaev, V.V. What makes the Peregrine soliton so special as a prototype of freak waves? *Journal of Engineering Mathematics* 67, 11–22 (2010).

[175] Gutshabash, Y. & Lavrenov, I. Swell transformation in the Cape Agulhas Current. *Izvestiya, Atmospheric and Oceanic Physics* 22, 494 – 497 (1986).

[176] Gerber, M. The interaction of deep-water gravity waves and an annular current: linear theory. *Journal of Fluid Mechanics* 248, 153–172 (1993).

[177] Fochesato, C., Grilli, S. & Dias, F. Numerical modeling of extreme rogue waves generated by directional energy focusing. *Wave Motion* 44, 395–416 (2007).

[178] Berry, M.V. & Upstill, C. IV Catastrophe Optics: Morphologies of Caustics and Their Diffraction Patterns. *Progress in Optics* 18, 257–346 (1980).

[179] Nye, J. & Wright, F.J. *Natural Focusing and Fine Structure of Light: Caustics and Wave Dislocations*. CRC Press (1999).

[180] Radder, A. On the parabolic equation method for water-wave propagation. *Journal of Fluid Mechanics* 95, 159–176 (1979).

[181] Born, M. & Wolf, E. *Principles of optics: electromagnetic theory of propagation, interference and diffraction of light*. CUP Archive (2000).

[182] Goodman, J.W. *Speckle phenomena in optics: theory and applications*. Roberts and Company (2007).

[183] Zwillinger, D. & White, B. Propagation of initially plane waves in the region of random caustics. *Wave Motion* 7, 207–227 (1985).

[184] Angelsky, O.V., Maksimyak, P.P., Maksimyak, A.P., Hanson, S.G. & Ushenko, Y.A. Role of caustics in the formation of networks of amplitude zeros for partially developed speckle fields. *Applied Optics* 43, 5744–5753 (2004).

[185] Sprague, R.A. Surface roughness measurement using white light speckle. *Applied Optics* 11, 2811–2816 (1972).

[186] Fujii, H. & Asakura, T. Effect of Surface Roughness on the Statistical Distribution of Image Speckle Intensity. *Optics Communications* 11, 35–38 (1974).

[187] Pedersen, H. The roughness dependence of partially developed, monochromatic speckle patterns. *Optics Communications* 12, 156–159 (1974).

[188] Beckmann, P. & Spizzichino, A. *The scattering of electromagnetic waves from rough surfaces*. Norwood, MA, Artech House, Inc. (1963).

[189] Pinel, N., Bourlier, C. & Saillard, J. Degree of roughness of rough layers: extensions of the rayleigh roughness criterion and some applications. *Progress In Electromagnetics Research B* 19, 41–63 (2010).

[190] Dainty, J. *Laser speckle and related phenomena*, volume 9. Springer-Verlag (1975).

[191] Goodman, J. *Introduction to Fourier Optics*. McGaw-Hill Physical and Quantum Electronics Series (1968).

[192] Goodman, J. Statistical properties of laser speckle patterns. *Laser speckle and related phenomena*, volume 9. Springer Berlin Heidelberg, 9–75 (1975).

[193] Ohtsubo, J. & Asakura, T. Statistical properties of laser speckle produced in the diffraction field. *Applied Optics* 16, 1742 (1977).

[194] Uozumi, J. & Asakura, T. The first-order statistics of partially developed non-Gaussian speckle patterns. *Journal of Optics* 12, 177–186 (1981).

[195] Fujii, H. Non-Gaussian speckle with correlated weak scatterers: a computer simulation. *Journal of the Optical Society of America* 69, 1573 (1979).

[196] Gerchberg, R. A practical algorithm for the determination of phase from image and diffraction plane pictures. *Optik* 35, 237 (1972).

[197] Pedrini, G., Osten, W. & Zhang, Y. Wave-front reconstruction from a sequence of interferograms recorded at different planes. *Optics Letters* 30, 833–835 (2005).

[198] Van Simaeys, G., Emplit, P. & Haelterman, M. Experimental demonstration of the Fermi-Pasta-Ulam recurrence in a modulationally unstable optical wave. *Physical Review Letters* 87, 033902 (2001).

[199] Akhmediev, N.N. & Korneev, V.I. Modulation instability and periodic solutions of the nonlinear Schrödinger equation. *Theoretical and Mathematical Physics* 69, 1089–1093 (1987).

[200] Peregrine, D.H. Water waves, nonlinear Schrödinger equations and their solutions. *Journal of the Australian Mathematical Society B* 25, 16–43 (1983).

[201] Kuznetsov E.A. Solitons in a parametrically unstable plasma. *Doklady Akademii Nauk SSSR* 236, 575–577 (1977).

[202] Ma, Y. The Perturbed Plane-wave Solutions of the Cubic Schrödinger Equation. *Studies in Applied Mathematics* 60, 43–58 (1979).

[203] Akhmediev, N., Ankiewicz, A. & Soto-Crespo, J.M. Rogue waves and rational solutions of the nonlinear Schrödinger equation. *Physical Review E* 80, 026601 (2009).

[204] Akhmediev, N. & Ankiewicz, A. *Solitons: nonlinear pulses and beams*. Chapman & Hall (1997).

[205] Dauxois, T. & Peyrard, M. *Physics of solitons*. Cambridge University Press (2006).

[206] Wang, L.H., Porsezian, K. & He, J.S. Breather and rogue wave solutions of a generalized nonlinear Schrödinger equation. *Physical Review E* 87, 069904 (2013).

[207] Baronio, F., Chen, S., Grelu, P., Wabnitz, S. & Conforti, M. Baseband modulation instability as the origin of rogue waves. *Physical Review A* 91, 033804 (2015).

[208] Genty, G. Private communication.

[209] Frosz, M.H. Validation of input-noise model for simulations of supercontinuum generation and rogue waves. *Optics Express* 18, 14778–14787 (2010).

[210] Trebino, R. *Frequency-Resolved Optical Gating: The Measurement of Ultrashort Laser Pulses: The Measurement of Ultrashort Laser Pulses*. Springer US (2000).

[211] Wabnitz, S. & Wetzel, B. Instability and noise-induced thermalization of Fermi-Pasta-Ulam recurrence in the nonlinear Schrödinger equation. *Physics Letters A* 378, 2750–2756 (2014).

[212] Soto-Crespo, J.M., Devine, N. & Akhmediev, N. Integrable Turbulence and Rogue Waves: Breathers or Solitons? *Physical Review Letters* 116, 103901 (2016).

[213] Janssen, P. On a random time series analysis valid for arbitrary spectral shape. *Journal of Fluid Mechanics* 759, 236–256 (2014).

[214] Gorbunov, O.A., Sugavanam, S. & Churkin, D. Revealing statistical properties of quasi-CW fibre lasers in bandwidth-limited measurements. *Optics Express* 22, 28071 (2014).

[215] Lecaplain, C. & Grelu, P. Rogue waves among noiselike-pulse laser emission: An experimental investigation. *Physical Review A* 90, 013805 (2014).

[216] Martin-Lopez, S., Gonzalez-Herraez, M., Corredera, P., Hernanz, M.L., Carrasco, A. & Mendez, J.A. Temperature effects on supercontinuum generation using a continuous-wave Raman fiber laser. *Optics Communications* 267, 193–196 (2006).

[217] Ankiewicz, A., Soto-Crespo, J.M., Chowdhury, M.A. & Akhmediev, N. Rogue waves in optical fibers in presence of third-order dispersion, self-steepening, and self-frequency shift. *Journal of the Optical Society of America B* 30, 87 (2012).

[218] Onorato, M., Osborne, A.R., Serio, M. & Cavaleri, L. Modulational instability and non-Gaussian statistics in experimental random water-wave trains. *Physics of Fluids* 17, 078101 (2005).

[219] Solli, D.R., Herink, G., Jalali, B. & Ropers, C. Fluctuations and correlations in modulation instability. *Nature Photonics* 6, 463–468 (2012).

[220] Wetzel, B., Stefani, A., Larger, L., Lacourt, P.A., Merolla, J.M., Sylvestre, T., Kudlinski, A., Mussot, A., Genty, G., Dias, F. & Dudley, J.M. Real-time full bandwidth measurement of spectral noise in supercontinuum generation. *Scientific Reports* 2, 882 (2012).

[221] Godin, T., Wetzel, B. & Sylvestre, T. Real time noise and wavelength correlations in octave-spanning supercontinuum generation. *Optics Express* 21, 994–999 (2013).

[222] Husko, C.A., Wulf, M., Combrie, S., De Rossi, A., Kuipers, K. & Eggleton, B.J. Near-field measurements of soliton fission in nanophotonic waveguides. *CLEO: QELS_Fundamental Science*. Optical Society of America (2014).

[223] Kip, D., Soljacic, M., Segev, M., Eugenieva, E. & Christodoulides, D.N. Modulation instability and pattern formation in spatially incoherent light beams. *Science* 290, 495–498 (2000).

[224] Levi, L., Schwartz, T., Manela, O. & Segev, M. Spontaneous pattern formation upon incoherent waves: From modulation-instability to dynamic equilibrium. *Conference on Quantum Electronics and Laser Science (QELS) - Technical Digest Series* 16, 7818–7831 (2007).

[225] Boyd, R.W., Lukishova, S.G. & Shen, Y.R. (Editors) *Self-focusing: Past and Present*. Springer (2009).

[226] Meier, J., Stegeman, G.I., Christodoulides, D.N., Silberberg, Y., Morandotti, R., Yang, H., Salamo, G., Sorel, M. & Aitchison, J.S. Experimental observation of discrete modulational instability. *Physical Review Letters* 92, 163902 (2004).

[227] Greer, E., Patrick, D., Wigley, P. & Taylor, J. Generation of 2 THz repetition rate pulse trains through induced modulational instability. *Electronics Letters* 25, 1246 (1989).

[228] Akhmanov, S., Chirkin, A., Drabovich, K., Kovrigin, A., Khokhlov, R. & Sukhorukov, A. Nonstationary nonlinear optical effects and ultrashort light pulse formation. *IEEE Journal of Quantum Electronics* 4, 598–605 (1968).

[229] Kolner, B.H. & Nazarathy, M. Temporal imaging with a time lens. *Optics Letters* 14, 630–632 (1989).

[230] Kolner, B.H. Space-time duality and the theory of temporal imaging. *IEEE Journal of Quantum Electronics* 30, 1951–1963 (1994).

[231] Bennett, C. & Kolner, B. Principles of parametric temporal imaging. I. System configurations. *IEEE Journal of Quantum Electronics* 36, 430–437 (2000).

[232] Howe, J.V. & Xu, C. Ultrafast optical signal processing based upon space-time dualities. *Journal of Lightwave Technology* 24, 2649–2662 (2006).

[233] Foster, M.A., Salem, R. & Gaeta, A.L. Ultrahigh-Speed Optical Processing Using Space-Time Duality. *Optics and Photonics News* 22, 29–35 (2011).

[234] Almeida, P.J., Petropoulos, P., Thomsen, B.C., Ibsen, M. & Richardson, D.J. All-optical packet compression based on time-to-wavelength conversion. *IEEE Photonics Technology Letters* 16, 1688–1690 (2004).

[235] Foster, M.A., Salem, R., Okawachi, Y., Turner-Foster, A.C., Lipson, M. & Gaeta, A.L. Ultrafast waveform compression using a time-domain telescope. *Nature Photonics* 3, 581–585 (2009).

[236] Bennett, C.V. & Kolner, B.H. Upconversion time microscope demonstrating 103x magnification of femtosecond waveforms. *Optics Letters* 24, 783–785 (1999).

[237] Salem, R., Foster, M.A., Turner-Foster, A.C., Geraghty, D.F., Lipson, M. & Gaeta, A.L. High-speed optical sampling using a silicon-chip temporal magnifier. *Optics Express* 17, 4324–4329 (2009).

[238] Okawachi, Y., Salem, R., Johnson, A.R., Saha, K., Levy, J.S., Lipson, M. & Gaeta, A.L. Asynchronous single-shot characterization of high-repetition-rate ultrafast waveforms using a time-lens-based temporal magnifier. *Optics Letters* 37, 4892–4894 (2012).

[239] Kauffman, M.T., Banyai, W.C., Godil, A.A. & Bloom, D.M. Time-to-frequency converter for measuring picosecond optical pulses. *Applied Physics Letters* 64, 270–272 (1994).

[240] Foster, M.A., Salem, R., Geraghty, D.F., Turner-Foster, A.C., Lipson, M. & Gaeta, A.L. Silicon-chip-based ultrafast optical oscilloscope. *Nature* 456, 81–84 (2008).

[241] Okawachi, Y., Salem, R., Foster, M.A., Turner-Foster, A.C., Lipson, M. & Gaeta, A.L. High-resolution spectroscopy using a frequency magnifier. *Optics Express* 17, 5691–5697 (2009).

[242] Sun, P.C., Mazurenko, Y.T. & Fainman, Y. Femtosecond pulse imaging:ultrafast optical oscilloscope. *Journal of the Optical Society of America A* 14, 1159 (1997).

[243] Chung, J.H. & Weiner, A.M. Real-time detection of femtosecond optical pulse sequences via time-to-space conversion in the lightwave communications band. *Journal of Lightwave Technology* 21, 3323–3333 (2003).

[244] Takagi, Y., Yamada, Y., Ishikawa, K., Shimizu, S. & Sakabe, S. Ultrafast single-shot optical oscilloscope based on time-to-space conversion due to temporal and spatial walk-off effects in nonlinear mixing crystal. *Japanese Journal of Applied Physics* 44, 6546–6549 (2005).

[245] Fridman, M., Farsi, A., Okawachi, Y. & Gaeta, A. Demonstration of temporal cloaking. *Nature* 481, 62–65 (2012).

[246] Lukens, J.M., Leaird, D.E. & Weiner, A.M. A temporal cloak at telecommunication data rate. *Nature* 498, 205–208 (2013).

[247] Tournois, P. Analogie optique de la compression d'impulsion. *Comptes Rendus de l'Académie des Sciences I* 258, 3839–3842 (1964).

[248] Tournois, P., Vernet, J. & Bienvenu, G. Sur l'analogie optique de certains montages électroniques: formation d'images temporelles de signaux électriques. *Comptes Rendus de l'Académie des Sciences I* 267, 375–378 (1968).

[249] Treacy, E.B. Optical Pulse Compression With Diffraction Gratings. *IEEE Journal of Quantum Electronics* 5, 454–458 (1969).

[250] Caputi, W.J. Stretch: a time-transformation technique. *Aerospace and Electronic Systems, IEEE Transactions* AES-7, 269–278 (1971).

[251] Jannson, T. Real-time Fourier transformation in dispersive optical fibers. *Optics Letters* 8, 232–234 (1983).

[252] Ruffin, A. Stimulated brillouin scattering: an overview of measurements, system impairments, and applications. *Symposium of Optical Fiber Measurements, National Institute of Standards and Technology*. Boulder, CO, 23–28 (2004).

[253] Kobyakov, A., Sauer, M. & Chowdhury, D. Stimulated Brillouin scattering in optical fibers. *Advances in Optics and Photonics* 2, 1–59 (2010).

[254] Murdoch, S., Leonhardt, R. & Harvey, J. Polarization modulation instability in weakly birefringent fibers. *Optics Letters* 20, 866–868 (1995).

[255] Itoh, H., Davis, G. & Sudo, S. Continuous-wave-pumped modulational instablity in an optical fiber. *Optics Letters* 14, 1368–1370 (1989).

[256] Yoshida, E. & Nakazawa, M. Low-threshold 115-GHz continuous-wave modulational-instability erbium-doped fiber laser. *Optics Letters* 22, 1409–1411 (1997).

[257] Coen, S. & Haelterman, M. Continuous-wave ultrahigh-repetition-rate pulse-train generation through modulational instability in a passive fiber cavity. *Optics Letters* 26, 39–41 (2001).

[258] Mussot, A., Lantz, E., Maillotte, H., Sylvestre, T., Finot, C. & Pitois, S. Spectral broadening of a partially coherent CW laser beam in single-mode optical fibers. *Optics Express* 12, 2838–2843 (2004).

[259] Hadjifotiou, A. & Hill, G.A. Suppression of stimulated Brillouin backscattering by PSK modulation for high-power optical-transmission. *IEEE Proceedings J - Optoelectronics* 133, 256–258 (1986).

[260] Dudley, J.M., Genty, G. & Coen, S. Supercontinuum generation in photonic crystal fiber. *Reviews of Modern Physics* 78, 1135–1184 (2006).

[261] Giordmaine, J., Duguay, M. & Hansen, J. Compression of optical pulses. *IEEE Journal of Quantum Electronics* 4, 252–255 (1968).

[262] Duguay, M. & Hansen, J. Compression of Pulses from a Mode-Locked He-Ne Laser. *Applied Physics Letters* 14, 14–16 (1969).

[263] Kolner, B. Active pulse compression using an integrated electro-optic phase modulator. *Applied Physics Letters* 52, 1122–1124 (1988).

[264] Kauffman, M.T., Godil, A.A., Auid, B.A., Banyai, W.C. & Bloom, D.M. Applications of time lens optical systems. *Electronics Letters* 29, 4–5 (1993).

[265] Godil, A.A., Auld, B.A. & Bloom, D.M. Picosecond time-lenses. *IEEE Journal of Quantum Electronics* 30, 827–837 (1994).

[266] Berger, N., Levit, B., Atkins, S. & Fischer, B. Time-lens-based spectral analysis of optical pulses by electrooptic phase modulation. *Electronics Letters* 36, 1644–1646 (2000).

[267] Bennett, C.V., Scott, R.P.R. & Kolner, B.H.B. Temporal magnification and reversal of 100 Gb/s optical data with an up-conversion time microscope. *Applied Physics Letters* 65, 2513–2515 (1994).

[268] Salem, R., Foster, M.A., Turner, A.C., Geraghty, D.F., Lipson, M. & Gaeta, A.L. Optical time lens based on four-wave mixing on a silicon chip. *Optics Letters* 33, 1047–1049 (2008).

[269] Pasquazi, A., Park, Y., Chu, S.T., Little, B.E., Légaré, F., Morandotti, R., Azaña, J. & Moss, D.J. Time-lens measurement of subpicosecond optical pulses in CMOS compatible high-index glass waveguides. *IEEE Journal on Selected Topics in Quantum Electronics* 18, 629–636 (2012).

[270] Hasegawa, A. Generation of a train of soliton pulses by induced modulational instability in optical fibers. *Optics Letters* 9, 288–290 (1984).

[271] Tai, K., Tomita, A., Jewell, J.L. & Hasegawa, A. Generation of subpicosecond solitonlike optical pulses at 0.3 THz repetition rate by induced modulational instability. *Applied Physics Letters* 49, 236–238 (1986).

[272] Genty, G. & Dudley, J.M. New approaches to supercontinuum control in the long pulse regime. *Proceedings of SPIE* 7212 (2009).

[273] Genty, G., Dudley, J.M. & Eggleton, B.J. Modulation control and spectral shaping of optical fiber supercontinuum generation in the picosecond regime. *Applied Physics B* 94, 187–194 (2009).

[274] Sørensen, S.T., Larsen, C., Møller, U., Moselund, P.M., Thomsen, C.L. & Bang, O. Influence of pump power and modulation instability gain spectrum on seeded supercontinuum and rogue wave generation. *Journal of the Optical Society of America B* 29, 2875 (2012).

[275] Li, Q., Li, F., Wong, K.K.Y., Lau, A.P.T., Tsia, K.K. & Wai, P.K.A. Investigating the influence of a weak continuous-wave-trigger on picosecond supercontinuum generation. *Optics Express* 19, 13757–13769 (2011).

[276] Cheung, K.K.Y., Zhang, C., Zhou, Y., Wong, K.K.Y. & Tsia, K.K. Manipulating supercontinuum generation by minute continuous wave. *Optics Letters* 36, 160–162 (2011).

[277] Chen, Z., Klinger, J. & Christodoulides, D.N. Induced modulation instability of partially spatially incoherent light with varying perturbation periods. *Physical Review E* 66, 066601 (2002).

[278] Dylov, D.V. & Fleischer, J.W. Modulation instability of a coherent-incoherent mixture. *Optics Letters* 35, 2149–2151 (2010).

[279] Drummond, P.D. & Corney, J.F. Quantum noise in optical fibers. I. Stochastic equations. *Journal of the Optical Society of America B* 18, 139–152 (2001).

[280] Akhmediev, N. & Pelinovsky, E. Editorial - Introductory remarks on "Discussion & Debate: Rogue Waves - Towards a Unifying Concept?". *The European Physical Journal Special Topics* 185, 1–4 (2010).

[281] Ying, L.H., Zhuang, Z., Heller, E.J. & Kaplan, L. Linear and nonlinear rogue wave statistics in the presence of random currents. *Nonlinearity* 24, R67–R87 (2011).

Appendix A

Some theoretical results

A.1 Transformation between different forms of NLSE

The *space* NLSE to the *time* NLSE of deep water waves

The *space* NLSE involves the second derivative with respect to spatial variable to describe the diffraction of the propagating wave, and the *time* NLSE involves the second derivative with respect to time to describe the dispersion of the propagating wave. These two seemingly different forms are related to each other as the group velocity v_g of the propagating wave relates the spatial and the time variable through $x = v_g t$.

The *space* NLSE governing the propagation of deep water waves (Eq. 2.6) is

$$i\left(\frac{\partial A}{\partial t} + v_g \frac{\partial A}{\partial x}\right) - \frac{\omega_0}{8k_0^2}\frac{\partial^2 A}{\partial x^2} - \frac{1}{2}\omega_0 k_0^2 |A|^2 A = 0,$$

where $A(x,t)$ is the slowly varying wave envelope, ω_0 and k_0 are the central frequency and the central wave number of the propagating wave respectively.

Since the space and time derivative can be related to each other through the chain rule and the $x = v_g t$ relation

$$\begin{aligned}
\frac{\partial A}{\partial t} &= \frac{\partial A}{\partial x}\frac{\partial x}{\partial t} = v_g \frac{\partial A}{\partial x} \\
\frac{\partial A}{\partial x} &= \frac{\partial A}{\partial t}\frac{\partial t}{\partial x} = \frac{1}{v_g}\frac{\partial A}{\partial t} \\
\frac{\partial^2 A}{\partial x^2} &= \frac{\partial}{\partial t}\left(\frac{1}{v_g}\frac{\partial A}{\partial t}\right)\frac{\partial t}{\partial x} = \frac{1}{v_g^2}\frac{\partial^2 A}{\partial t^2},
\end{aligned}$$

the *space* NLSE can be transformed into the *time* NLSE (Eq. 2.7)

$$i\left(\frac{\partial A}{\partial x} + \frac{1}{v_g}\frac{\partial A}{\partial t}\right) - \frac{k_0}{\omega_0^2}\frac{\partial^2 A}{\partial t^2} - k_0^3 |A|^2 A = 0.$$

The *time* NLSE to the *dimensionless time* NLSE of deep water waves

The following retarded time transformation relates the independent variable of space and time, x and t, with X and T as

$$\begin{aligned} X &= x \\ T &= t - \frac{1}{v_g} x. \end{aligned} \tag{A.1}$$

Therefore, the *time* NLSE in the *co-moving / retarded frame* can be written as

$$i\frac{\partial A}{\partial X} - \frac{k_0}{\omega_0^2}\frac{\partial^2 A}{\partial T^2} - k_0^3 |A|^2 A = 0.$$

In order to obtain a dimensionless equation, dimensionless variables are introduced, defined as

$$\xi = -k_0^3 A_0^2 X$$

$$\tau = \frac{1}{\sqrt{2}}\omega_0 k_0 A_0 T \tag{A.2}$$

$$\psi = \frac{A}{A_0}. \tag{A.3}$$

The *dimensionless time* NLSE then becomes

$$\boxed{i\frac{\partial \psi}{\partial \xi} + \frac{1}{2}\frac{\partial^2 \psi}{\partial \tau^2} + |\psi|^2 \psi = 0}$$

The *time* NLSE to the *dimensionless time* NLSE of electromagnetic waves

The *time* NLSE governing the propagation of optical waves in an optical fibre (Eq. 2.20) is

$$\left(\frac{\partial A}{\partial z} + \beta_1 \frac{\partial A}{\partial t}\right) + i\frac{\beta_2}{2}\frac{\partial^2 A}{\partial t^2} - i\gamma |A|^2 A = 0,$$

where $A(x,t)$ is the slowly varying wave envelope, $\beta_1 = c/n_g$, β_2 is the group velocity dispersion (GVD), and γ is the fibre nonlinearity.

The following retarded time transformation relates the independent variable of space and time, z and t, with Z and T as

$$\begin{aligned} Z &= z \\ T &= t - \beta_1 z. \end{aligned} \tag{A.4}$$

Therefore, the *time* NLSE in the *co-moving / retarded frame* can be written as

$$i\frac{\partial A}{\partial Z} - \frac{\beta_2}{2}\frac{\partial^2 A}{\partial T^2} + \gamma |A|^2 A = 0.$$

In order to obtain a dimensionless equation, dimensionless variables are introduced, defined as

$$\xi = \gamma P_0 Z$$

$$\tau = \sqrt{\frac{\gamma P_0}{|\beta_2|}} T \tag{A.5}$$

$$\psi = \frac{A}{\sqrt{P_0}}, \tag{A.6}$$

where P_0 is the incident power.

The *dimensionless time* NLSE then becomes

$$\boxed{i\frac{\partial \psi}{\partial \xi} + \frac{1}{2}\frac{\partial^2 \psi}{\partial \tau^2} + |\psi|^2 \psi = 0} \tag{A.7}$$

A.2 Properties of elementary breather structures

The NLSE governs the evolution of wave envelope ψ as a function of space and time. However, the measurable quantity of this solution is generally either the amplitude $|\psi|$ (the absolute value of the envelope ψ) for the surface elevation of ocean waves, or the intensity $|\psi|^2$ (the squared of absolute value of the envelope ψ) of optical waves.

In this part, we derive the maximum amplitude $|\psi|_{\max}$ and intensity $|\psi|^2_{\max}$ of both Akhmediev breather and Peregrine soliton solutions, together with their corresponding temporal width in terms of the full width at half maximum (FWHM). Associated with the study conducted in Chapter 4, these properties are derived for the *dimensionless time* NLSE.

Akhmediev breather (AB) for $0 < a < 0.5$

The AB solutions of the NLSE shown in Eq. A.7 can be written in the form

$$\psi(\xi, \tau) = \left[1 + \frac{2(1-2a)\cosh(b\xi) + ib\sinh(b\xi)}{\sqrt{2a}\cos(\omega\tau) - \cosh(b\xi)}\right] e^{i\xi}, \tag{A.8}$$

with $b = \sqrt{8a(1-2a)}$ and $\omega = 2\sqrt{1-2a}$, showing that the properties of this solution can be determined by a single parameter a ($a \neq 0.5$). The PS solution for $a = 0.5$ is given later. At the distance of maximum compression $\xi = 0$, the temporal profile is

$$\psi(0, \tau) = 1 + \frac{2(1-2a)}{\sqrt{2a}\cos(\omega\tau) - 1}. \tag{A.9}$$

The measurable quantity of this solution is in general either the amplitude $|\psi|$ (the absolute value of the envelope ψ) for the surface elevation of ocean waves, or the intensity (the squared of absolute value of the envelope ψ) of optical waves. Plotting the temporal cross section of these measurable quantities as a function of a, we can see two different kinds of profile, either a smooth variation of train of pulses, or a train of pulses with "wings" between the pulses. Fig. A.1(a-c) show

different temporal profiles corresponding to different values of a. We can see that as the amplitude of the AB solution increases, the maximum of the envelope ψ goes to positive value, forming the "wings" in the temporal profiles of the absolute value of the function.

The threshold between these two different kinds of temporal profile is obtained when the maximum of the envelope ψ reaches zero.

$$\psi_{\max} = \psi\left(0, \frac{\Delta\tau}{2}\right) = \psi\left(0, \frac{\pi}{2\sqrt{1-2a}}\right) = 0,$$

where $\Delta\tau$ is the temporal period of the AB structure calculated from $\Delta\tau = 2\pi/\omega = \pi/\sqrt{1-2a}$. Using Eq. A.9, the value of a can be calculated by setting the maximum envelope $\psi_{\max}$ (the minimum amplitude $|\psi|_{\min}$)

$$|\psi|_{\min} = \psi_{\max} = 1 - \frac{2(1-2a)}{\sqrt{2a}+1} = 2\sqrt{2a} - 1$$

equals zero, which gives the value of $a = 0.125$ (see Fig. A.1(b)).

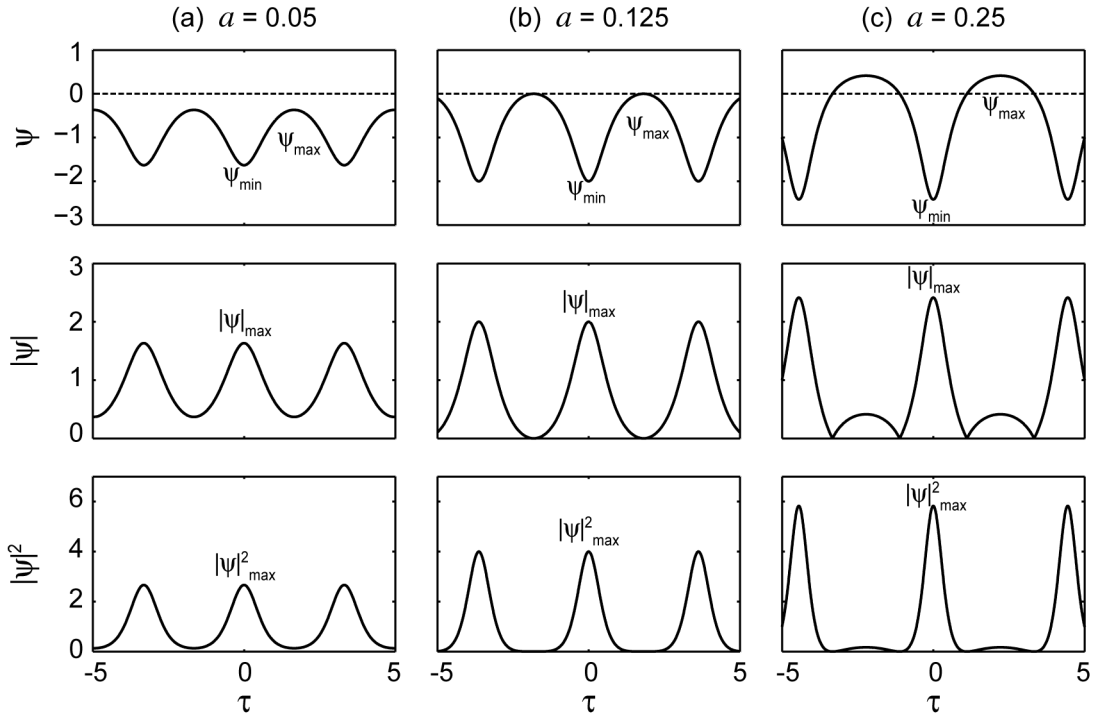

Figure A.1: Temporal profiles of AB solutions for different a parameter: (a) 0.1, (b) 0.125, (c) 0.25.

Peak amplitude $|\psi|_{\max}$ and the corresponding temporal width $\delta\tau^A$

As can be seen from Fig. A.1, the maximum amplitude $|\psi|_{\max}$ of the solution corresponds to the minima of the envelope ψ, which is located at time $\tau = 0$. It can therefore be calculated by

$$|\psi|_{\max} = |\psi(0,0)| = \left|1 + \frac{2(1-2a)}{\sqrt{2a}-1}\right| = 2\sqrt{2a} + 1.$$

The associated FWHM temporal width of the amplitude pulse $\delta\tau^A$ is two times the time span of the amplitude at half maximum $|\psi|_{\text{HM}}$, which we denote here as τ^A_{HM}. From Eq. A.9, this implies that

$$-|\psi|_{\text{HM}} = 1 + \frac{2(1-2a)}{\sqrt{2a}\cos(\omega\tau^A_{\text{HM}}) - 1},$$

from where we obtain

$$\delta\tau^A = 2\,\tau^A_{\text{HM}} = \frac{1}{\sqrt{1-2a}}\cos^{-1}\left[\frac{1}{\sqrt{2a}}\left(1 - \frac{2(1-2a)}{|\psi|_{\text{HM}}+1}\right)\right]. \tag{A.10}$$

For $a \leq 0.125$,

$$|\psi|_{\text{HM}} = \frac{1}{2}\left(|\psi|_{\min} + |\psi|_{\max}\right) = -1,$$

while for $a \geq 0.125$,

$$|\psi|_{\text{HM}} = \frac{1}{2}|\psi|_{\max} = \sqrt{2a} + \frac{1}{2}.$$

Peak intensity $|\psi|^2_{\max}$ and the corresponding temporal width $\delta\tau^I$

Similarly, the maximum intensity of the solution as a function of a correponds to the intensity at time $\tau = 0$

$$|\psi|^2_{\max} = |\psi(0,0)|^2 = \left(2\sqrt{2a}+1\right)^2.$$

Whilst the FWHM temporal width of the intensity pulse $\delta\tau^I$ can be obtained from the relation

$$-\sqrt{|\psi|^2_{\text{HM}}} = 1 + \frac{2(1-2a)}{\sqrt{2a}\cos(\omega\tau^I_{\text{HM}}) - 1},$$

which yields

$$\delta\tau^I = 2\,\tau^I_{\text{HM}} = \frac{1}{\sqrt{1-2a}}\cos^{-1}\left[\frac{1}{\sqrt{2a}}\left(1 - \frac{2(1-2a)}{\sqrt{|\psi|^2_{\text{HM}}}+1}\right)\right]. \tag{A.11}$$

For $a \leq 0.125$,

$$|\psi|^2_{\text{HM}} = \frac{1}{2}\left(|\psi|^2_{\min} + |\psi|^2_{\max}\right) = 8a + 1,$$

while for $a \geq 0.125$,

$$|\psi|^2_{\text{HM}} = \frac{1}{2}|\psi|^2_{\max} = \frac{1}{2}\left(\sqrt{2a} + \frac{1}{2}\right)^2.$$

Note that although Eq. A.11 seems to be very similar to Eq. A.10, these two quantities are not the same due to the fact that $|\psi|^2_{\text{HM}} \neq \left(|\psi|_{\text{HM}}\right)^2$, as can be seen from the last two equations.

PS $(a = 0.5)$

In the limit $a \to 0.5$ the solution written in Eq. A.8 is replaced by the rational Peregrine soliton (PS) solution [200]

$$\psi_{\text{PS}}(\xi,\tau) = \left[1 - \frac{4(1+2i\xi)}{1+4\tau^2+4\xi^2}\right]e^{i\xi}.$$

At the distance of maximum compression $\xi = 0$, the temporal profile is

$$\psi_{\text{PS}}(0,\tau) = 1 - \frac{4}{1+4\tau^2}. \tag{A.12}$$

Peak amplitude $|\psi_{\text{PS}}|_{\max}$ and the corresponding temporal width $\delta\tau^A_{\text{PS}}$

The maximum amplitude of PS soliton $|\psi_{\text{PS}}|_{\max}$, correponding to the amplitude at time $\tau = 0$ is

$$|\psi_{\text{PS}}|_{\max} = |\psi_{\text{PS}}(0,0)| = 3.$$

The temporal width of the PS amplitude $\delta\tau^A_{\text{PS}}$ can be obtained from

$$-|\psi_{\text{PS}}|_{\text{HM}} = 1 - \frac{4}{1+4(\tau^A_{\text{HM}})^2},$$

where $|\psi_{\text{PS}}|_{\text{HM}} = \frac{1}{2}|\psi_{\text{PS}}|_{\max} = \frac{3}{2}$, yielding

$$\delta\tau^A_{\text{PS}} = 2\,\tau^A_{\text{HM}} = \sqrt{\frac{3}{5}} \approx 0.77$$

Peak intensity $|\psi_{\text{PS}}|^2_{\max}$ and the corresponding temporal width $\delta\tau^I_{\text{PS}}$

The maximum intensity of PS soliton $|\psi_{\text{PS}}|^2_{\max}$, correponding to the intensity at time $\tau = 0$ is

$$|\psi_{\text{PS}}|^2_{\max} = |\psi_{\text{PS}}(0,0)|^2 = 9.$$

The temporal width of the PS intensity $\delta\tau^I_{\text{PS}}$ can be obtained from

$$-\sqrt{|\psi_{\text{PS}}|^2_{\text{HM}}} = 1 - \frac{4}{1+4(\tau^I_{\text{HM}})^2},$$

where $|\psi_{\text{PS}}|^2_{\text{HM}} = \frac{1}{2}|\psi_{\text{PS}}|^2_{\max} = \frac{9}{2}$, yielding

$$\delta\tau^I_{\text{PS}} = 2\,\tau^I_{\text{HM}} = \sqrt{\frac{3\left(\sqrt{2}-1\right)}{3+\sqrt{2}}} \approx 0.53$$

Appendix B

Numerical Methods

B.1 The angular spectrum of plane waves

In terms of Fourier optics in spatial domain, an arbitrary wavefront can be decomposed into infinite number of plane waves propagating in different angular directions. If we consider a field A across a plane parallel to the xy-plane propagating in the z-direction, the Fourier spectrum (angular spectrum) $\tilde{A}$ can then be related to A as

$$A(x, y; z) = \iint_{-\infty}^{\infty} \tilde{A}(k_x, k_y; z) \exp(-j2\pi(k_x x + k_y y))\mathrm{d}k_x \mathrm{d}k_y.$$

While the propagation of a monochromatic electromagnetic field in a charge-free, homogeneous, and linear medium is governed by the Helmholtz equation

$$\nabla^2 A + k^2 A = 0,$$

with $k^2 = k_x^2 + k_y^2 + k_z^2$ and $k = 2\pi/\lambda$, where λ is the wavelength of the light. This means that the field A must satisfy the differential equation

$$\frac{\mathrm{d}^2}{\mathrm{d}z^2}\tilde{A}\left(k_x, k_y; z\right) + \left(k^2 - k_x^2 - k_y^2\right)\tilde{A}\left(k_x, k_y; z\right) = 0,$$

which yields a solution of

$$\tilde{A}\left(k_x, k_y; z\right) = \tilde{A}\left(k_x, k_y; 0\right) \exp\left(j\sqrt{k^2 - k_x^2 - k_y^2}z\right). \tag{B.1}$$

This exponential term representing the phase shift is the transfer function of the propagation in linear medium of distance z.

B.2 Phase retrieval algorithm

The wavefront of light at any distance along the propagation can be calculated by the method shown above once the amplitude and phase of the light at one position is known. Experimental

measurement of light by optical detectors however, records only the intensity of the light and not the electric field itself. Analysis of the complex amplitude of the recorded data can therefore only be done by extracting the phase information of the field.

In the setup we have in Chapter 3, two-dimensional intensity patterns of modulated light beam at different positions along propagation were recorded by displacing the imaging system (CCD camera). Following a similar algorithm as reported in Ref. [197], the phase of the recorded intensity patterns can be retrieved by applying an iterative algorithm based on the Gerchberg-Saxton algorithm [196].

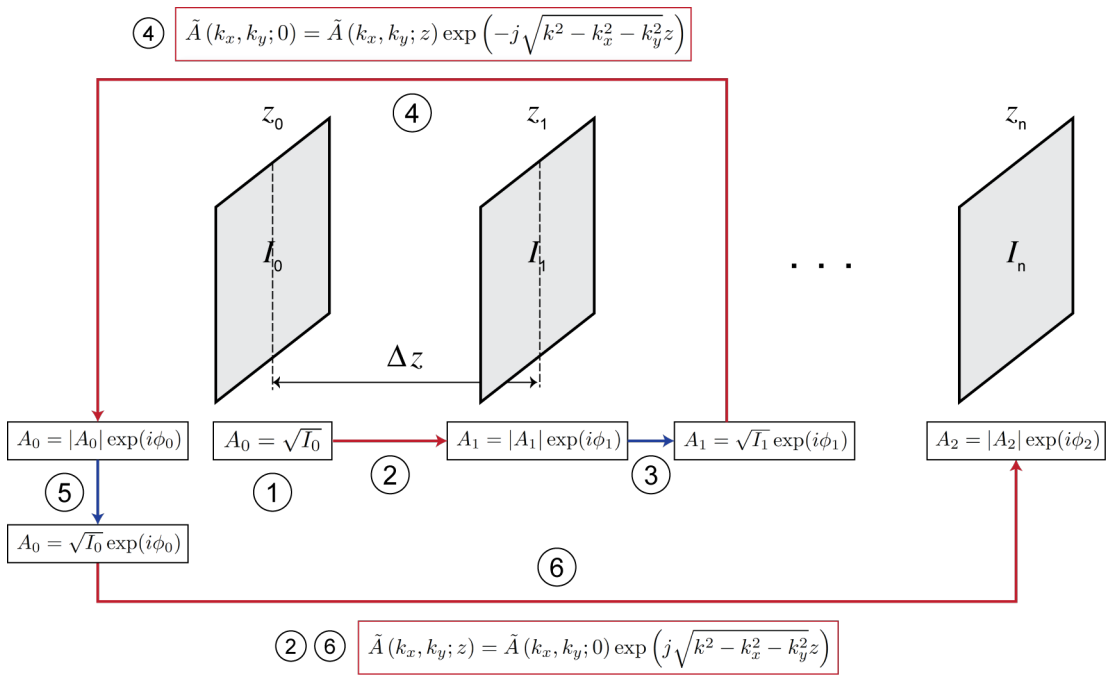

Figure B.1: Schematic of phase retrieval algorithm used to reconstruct the amplitude distribution from the recorded intensity volume.

As depicted in Fig. B.1, the procedure of phase retrieval algorithm we applied is as follows:

1. We take the square root of the recorded intensity pattern at z_0 (first recorded plane) $A_0 = \sqrt{I_0}$ and assume that the phase $\phi_0 = 0$.

2. The wavefront $A_0 = |A_0|\exp(i\phi_0)$ is then propagated from z_0 to $z_0 + \Delta z$ by using the diffraction relation described above (Eq. B.1), resulting in complex amplitude $A_1 = |A_1|\exp(i\phi_1)$.

3. We take the square root of recorded intesity pattern at $z_0+\Delta z$ and replace the amplitude $|A_1|$ with this value, such that the complex amplitude at this position is now $A_1 = \sqrt{I_1}\exp(i\phi_1)$.

4. The wavefront A_1 is then back-propagated from $z_0+\Delta z$ to z_0 by using the diffraction relation, yielding a new complex amplitude at the first plane $A_0 = |A_0|\exp(i\phi_0)$.

5. We then replace this new amplitude $|A_0|$ with the square root of the recorded intensity pattern and obtain $A_0 = \sqrt{I_0}\exp(i\phi_0)$.

6. Step 2 until 5 are then repeated for all recorded intensity pattern at distance $z_0 + n\Delta z$, with n being the number of the recorded plane.

7. This overall procedure can be repeated for improvement of the results.

B.3 The split-step Fourier method

The NLSE can only be solved analytically in some specific cases where inverse scattering method can be applied. Understanding the evolution of an arbitrary input field along the propagation in an optical fiber therefore requires numerical approach. Specifically, split-step Fourier method provides a reasonably accurate solutions for the MI studies conducted in Chapter 4 - 6 with a relatively short calculation time. As we will see below, this method performs separately the linear and the nonlinear effects in small steps computation, where the linear step is made in the frequency domain and the nonlinear step in the time domain.

In terms of dispersion and nonlinearity, the NLSE can be written as

$$\frac{\partial A}{\partial z} = \left(\hat{D} + \hat{N}\right) A,$$

where $\hat{D}$ is a differential operator taking into account the linear effects of the material (dispersion and losses) and $\hat{N}$ is a nonlinear operator taking into account the fiber nonlinearities. In the case of the GNLSE shown in Eq. 2.23, these operators are

$$\begin{aligned} \hat{D} &= -\frac{i\beta_2}{2}\frac{\partial^2}{\partial T^2} + \frac{\beta_3}{6}\frac{\partial^3}{\partial T^3} - \frac{\alpha}{2} \\ \hat{N} &= i\gamma\left(|A|^2 + \frac{i}{\omega_0}\frac{1}{A}\frac{\partial}{\partial T}(|A|^2 A) - T_R\frac{\partial |A|^2}{\partial T}\right). \end{aligned} \tag{B.2}$$

The split-step Fourier method is based on an approximation that the dispersive and the nonlinear effects can be assumed to act independently on the propagating optical field over a sufficiently small distance h. The exact solution of the NLSE

$$A(z+h,T) = \exp\left[h\left(\hat{D} + \hat{N}\right)\right] A(z,T)$$

can therefore be replaced by

$$A(z+h,T) \approx \exp(h\hat{D})\exp(h\hat{N})A(z,T),$$

which can then be evaluated in two steps.

In the first step, only $\exp(h\hat{N})$ is operated on $A(z,T)$:

$$B(z,T) \approx \exp(h\hat{N})A(z,T)$$

In the second step, $\exp(h\hat{D})$ operates on the results of the first step:

$$C(z+h,T) \approx \exp(h\hat{D})B(z,T).$$

The evaluation of the operator $\exp(h\hat{D})$ can be done straighforwardly in the frequency domain by replacing $\frac{\partial}{\partial T}$ in the operator $\hat{D}$ shown in Eq. B.2 by $-i\omega$, where ω is the frequency. This equation can therefore be expressed as

$$C(z+h,T) = FT^{-1}\left\{\exp\left[h\hat{D}(-i\omega)\right] FT\left\{B(z,T)\right\}\right\}$$

These two steps are then repeated sequentially in an iterative way.

Appendix C

Explicit form of higher-order breathers

The explicit forms used to plot the higher-order breathers in Chapter 4 are given here. The formulas of the higher-order breather generated from AB collision are adopted from Ref. [7], while the ones of the higher-order rational solutions are adopted from Ref. [203].

C.1 Collision of ABs

An m-order breather ψ_m is a superposition of m ABs, each can be described by a complex number

$$l_m = \mu_m + i\nu_m, \tag{C.1}$$

with the real number μ corresponds to the velocity of the AB and the imaginary number ν corresponds to the modulation frequency a through $\nu = \sqrt{2a}$.

Depending on the order of the breather, the following functions need first to be evaluated

$$\begin{aligned} r_m &= \left\{ A \exp\left[\frac{i}{2}\left(2\chi_m + \kappa_m\tau + l_m\kappa_m\xi\right)\right] - B \exp\left[-\frac{i}{2}\left(2\chi_m + \kappa_m\tau + l_m\kappa_m\xi\right)\right]\right\} \exp\left(-i\frac{\xi}{2}\right) \\ s_m &= \left\{ A \exp\left[\frac{i}{2}\left(-2\chi_m + \kappa_m\tau + l_m\kappa_m\xi\right)\right] + B \exp\left[-\frac{i}{2}\left(-2\chi_m + \kappa_m\tau + l_m\kappa_m\xi\right)\right]\right\} \exp\left(i\frac{\xi}{2}\right), \end{aligned} \tag{C.2}$$

for all the contituent ABs, with

$$\begin{aligned} A &= \exp\left[\frac{1}{2}\left(il_m\kappa_m\xi_{0m} - i\kappa_m\tau_{0m} - i\frac{\pi}{2}\right)\right] \\ B &= \exp\left[\frac{1}{2}\left(-il_m\kappa_m\xi_{0m} + i\kappa_m\tau_{0m} + i\frac{\pi}{2}\right)\right], \end{aligned}$$

where

$$\kappa_m = 2\sqrt{1+l_m^2}$$
$$\chi_m = \frac{1}{2}\arccos\left(\frac{\kappa_m}{2}\right).$$

Parameter ξ_{0m} and τ_{0m} in these equations take into account the spatial and temporal phase shift of the AB. For an AB centered at the origin $(0,0)$ both parameters can then be set to zero.

First-order breather

The first solution obtained from Darboux transformation is

$$\psi_1 = \psi_0 + \frac{2(l_1^* - l_1)s_1 r_1^*}{|r_1|^2 + |s_1|^2}, \tag{C.3}$$

where parameter l_1, r_1, and s_1 can be obtained straightforwardly from Eq. C.1 and Eq. C.2 by replacing m with 1. The seeding solution ψ_0 is assumed to be a plane wave of amplitude 1

$$\psi_0 \quad = \quad \exp(i\xi)$$

Second-order breather

The second-order solution as the superposition of two ABs with $l_1 = \mu_1 + i\nu_1$ and $l_2 = \mu_2 + i\nu_2$ is

$$\psi_{12} \quad = \quad \psi_1 + \frac{2(l_2^* - l_2)s_{12} r_{12}^*}{|r_{12}|^2 + |s_{12}|^2}, \tag{C.4}$$

where ψ_1 is the function of the first AB following Eq. C.3, while r_{12} and s_{12} written in terms of r_1, s_1, r_2, and s_2 (obtained from Eq. C.2) are

$$\begin{aligned} r_{12} &= \frac{(l_1^* - l_1)s_1^* r_1 s_2 + (l_2 - l_1)|r_1|^2 r_2 + (l_2 - l_1^*)|s_1|^2 r_2}{|r_1|^2 + |s_1|^2} \\ s_{12} &= \frac{(l_1^* - l_1)s_1 r_1^* r_2 + (l_2 - l_1)|s_1|^2 s_2 + (l_2 - l_1^*)|r_1|^2 s_2}{|r_1|^2 + |s_1|^2}. \end{aligned} \tag{C.5}$$

Third-order breather

The third-order solution as superposition of three ABs with $l_1 = \mu_1 + i\nu_1$, $l_2 = \mu_2 + i\nu_2$, and $l_3 = \mu_3 + i\nu_3$ is

$$\psi_{123} \quad = \quad \psi_{12} + \frac{2(l_3^* - l_3)s_{123} r_{123}^*}{|r_{123}|^2 + |s_{123}|^2},$$

where ψ_{12} is the second-order breather solution shown in Eq. C.3, while r_{123} and s_{123} are functions of r_{12}, s_{12}, r_{13}, and s_{13}

$$r_{123} = \frac{(l_2^* - l_2)s_{12}^* r_{12} s_{13} + (l_3 - l_2)|r_{12}|^2 r_{13} + (l_3 - l_2^*)|s_{12}|^2 r_{13}}{|r_{12}|^2 + |s_{12}|^2}$$
$$s_{123} = \frac{(l_2^* - l_2)s_{12} r_{12}^* r_{13} + (l_3 - l_2)|s_{12}|^2 s_{13} + (l_3 - l_2^*)|r_{12}|^2 s_{13}}{|r_{12}|^2 + |s_{12}|^2}.$$

Similar to Eq. C.5, r_{13} and s_{13} can be written in terms of r_1, s_1, r_3, and s_3 (obtained from Eq. C.2) as

$$r_{13} = \frac{(l_1^* - l_1)s_1^* r_1 s_3 + (l_3 - l_1)|r_1|^2 r_3 + (l_3 - l_1^*)|s_1|^2 r_3}{|r_1|^2 + |s_1|^2}$$
$$s_{13} = \frac{(l_1^* - l_1)s_1 r_1^* r_3 + (l_3 - l_1)|s_1|^2 s_3 + (l_3 - l_1^*)|r_1|^2 s_3}{|r_1|^2 + |s_1|^2}.$$

C.2 Higher-order rational solutions

The rational solution of the NLSE of any order can be written as

$$\psi_n^{\text{RS}} = \left[(-1)^n + \frac{G_n(\xi,\tau) + i\xi H_n(\xi,\tau)}{D_n(\xi,\tau)}\right] e^{i\xi}.$$

Below are the explicit forms of the second-order and the third-order rational solutions.

Second-order rational solution

$$\psi_2^{\text{RS}} = \left[1 + \frac{G_2 + i\xi H_2}{D_2}\right] e^{i\xi},$$

where G_2, H_2, and D_2 are given by

$$G_2 = \frac{3}{8} - 3\tau^2 - 2\tau^4 - 9\xi^2 - 10\xi^4 - 12\tau^2\xi^2$$
$$H_2 = \frac{15}{4} + 6\tau^2 - 4\tau^4 - 2\xi^2 - 4\xi^4 - 8\tau^2\xi^2$$
$$D_2 = \frac{1}{8}\left[\frac{3}{4} + 9\tau^2 + 4\tau^4 + \frac{16}{3}\tau^6 + 33\xi^2 + 36\xi^4 + \frac{16}{3}\xi^6 - 24\tau^2\xi^2 + 16\tau^4\xi^2 + 16\tau^2\xi^4\right]$$

Third-order rational solution

$$\psi_3^{\text{RS}} = \left[-1 + \frac{G_3 + i\xi H_3}{D_3}\right] e^{i\xi}$$

where G_3, H_3, and D_3 are given by

$$G_3(\xi,\tau) = \sum_{n=0}^{5} g_{2n}(\tau)(2\xi)^{2n}$$
$$H_3(\xi,\tau) = \sum_{n=0}^{5} h_{2n}(\tau)(2\xi)^{2n}$$
$$D_3(\xi,\tau) = \sum_{n=0}^{6} d_{2n}(\tau)\xi^{2n}$$

g_{2n} polynomials

$$g_0(\tau) = 1 - (2\tau)^2 - \frac{2}{3}(2\tau)^4 + \frac{14}{45}(2\tau)^6 + \frac{1}{45}(2\tau)^8 + \frac{1}{675}(2\tau)^{10}$$
$$g_2(\tau) = -3 - 20(2\tau)^2 + \frac{2}{3}(2\tau)^4 + \frac{4}{45}(2\tau)^6 + \frac{1}{45}(2\tau)^8$$
$$g_4(\tau) = 2\left[-\frac{17}{3} + 5(2\tau)^2 - \frac{1}{9}(2\tau)^4 + \frac{1}{27}(2\tau)^6\right]$$
$$g_6(\tau) = \frac{2}{45}\left[73 + 14(2\tau)^2 + \frac{7}{3}(2\tau)^4\right]$$
$$g_8(\tau) = \frac{1}{15}\left[11 + (2\tau)^2\right]$$
$$g_{10}(\tau) = \frac{11}{675}$$

h_{2n} polynomials

$$h_0(\tau) = 2\left[7 + 7(2\tau)^2 - 2(2\tau)^4 - \frac{2}{27}(2\tau)^6 - \frac{1}{45}(2\tau)^8 + \frac{1}{675}(2\tau)^{10}\right]$$
$$h_2(\tau) = \frac{2}{3}\left[-11 - 28(2\tau)^2 - 2(2\tau)^4 - \frac{28}{45}(2\tau)^6 + \frac{1}{45}(2\tau)^8\right]$$
$$h_4(\tau) = \frac{4}{15}\left[-107 + 19(2\tau)^2 - \frac{7}{3}(2\tau)^4 + \frac{1}{9}(2\tau)^6\right]$$
$$h_6(\tau) = \frac{4}{45}\left[-29 - 2(2\tau)^2 + \frac{1}{3}(2\tau)^4\right]$$
$$h_8(\tau) = \frac{2}{27}\left[1 + \frac{1}{5}(2\tau)^2\right]$$
$$h_{10}(\tau) = \frac{2}{675}$$

d_{2n} polynomials

$$
\begin{aligned}
h_0(\tau) &= \frac{1}{8}\left[1 + 6(2\tau)^2 + \frac{5}{3}(2\tau)^4 + \frac{52}{54}(2\tau)^6 + \frac{1}{15}(2\tau)^8 + \frac{2}{675}(2\tau)^{10} + \frac{1}{2025}(2\tau)^{12}\right] \\
h_2(\tau) &= 23 - 9(2\tau)^2 + \frac{10}{3}(2\tau)^4 + \frac{2}{15}(2\tau)^6 - \frac{1}{45}(2\tau)^8 + \frac{1}{675}(2\tau)^{10} \\
h_4(\tau) &= 2\left[71 + \frac{116}{3}(2\tau)^2 - \frac{2}{3}(2\tau)^4 - \frac{4}{45}(2\tau)^6 + \frac{1}{135}(2\tau)^8\right] \\
h_6(\tau) &= \frac{32}{3}\left[\frac{17}{3} + 5(2\tau)^2 + \frac{1}{45}(2\tau)^4 + \frac{1}{135}(2\tau)^6\right] \\
h_8(\tau) &= \frac{32}{15}\left[\frac{83}{3} + 2(2\tau)^2 + \frac{1}{27}(2\tau)^4\right] \\
h_{10}(\tau) &= \frac{2^8}{225}\left[7 + \frac{1}{3}(2\tau)^2\right] \\
h_{12}(\tau) &= \frac{2^9}{2025}
\end{aligned}
$$

Publication List

A. Scientific journals:

1. M. Närhi, B. Wetzel, C. Billet, S. Toenger, T. Sylvestre, J.M. Merolla, R. Morandotti, F. Dias, G. Genty, J. M. Dudley, "*Real-time rogue waves: measurement of ultrafast spontaneous breathers in noise-driven modulation instability*" (submitted).

2. A. Mathis, L. Froehly, S. Toenger, F. Dias, G. Genty, J. M. Dudley, "*Caustics and Rogue Waves in an Optical Sea*", Scientific Reports **5**, 12822 (2015).

3. S. Toenger, T. Godin, C. Billet, F. Dias, M. Erkintalo, G. Genty, J. M. Dudley, "*Emergent rogue wave structures and statistics in spontaneous modulation instability*", Scientific Reports **5**, 10380 (2015).

4. D. M. Nguyen, T. Godin, S. Toenger, Y. Combes, B. Wetzel, T. Sylvestre, J. M. Merolla, L. Larger, G. Genty, F. Dias, J. M. Dudley, "*Incoherent resonant seeding of modulation instability in optical fiber*", Optics Letters **38** (24), 5338-5341 (2013).

B. Scientific conferences:

1. S. Toenger, T. Godin, C. Billet, F. Dias, M. Erkintalo, G. Genty, J. M. Dudley, "*Dynamics of Rogue Wave and Soliton Emergence in Spontaneous Modulation Instability*". In CLEO : QELS_Fundamental Science (FW4D-2). San Jose (United States), 10-15 May 2015. OSA.

2. S. Toenger, G. Genty, F. Dias, M. Erkintalo, J. M. Dudley, "*Rogue Wave Structures in Spontaneous Modulation Instability*". In Nonlinear Photonics (NM3A-3). Barcelona (Spain), 27-31 July 2014. OSA.

3. T. Godin, D. M. Nguyen, S. Toenger, Y. Combes, B. Wetzel. T. Sylvestre, G. Genty, F. Dias, J. M. Dudley, "*Controlling modulation instability using an incoherent low amplitude seed*". In SPIE Photonics Europe (Nonlinear Optics and Its Application VIII; and Quantum Optics III, 91360N). Brussels (Belgium), 14-17 April 2014.

4. G. Genty, F. Dias, M. Erkintalo, S. Toenger, J. M. Dudley, "*Extreme localization of light in optical systems*". In PQE - the Winter Colloqium on the Physics of Quantum Electronics. Snowbird (United States), 5-9 January 2014.

Document réalisé avec LaTeX et :
le style LaTeX pour Thèse de Doctorat créé par S. Galland — http://www.multiagent.fr/ThesisStyle
la collection de paquets `tex-upmethodology` — http://www.arakhne.org/tex-upmethodology/

Résumé :

Ces travaux de thèse présentent l'étude des différantes classes d'effets linéaires et non-linéaires en optique qui génèrent des événements extrêmes dont les propriétés sont analogues à celles des « vagues scélérates » destructrices qui apparaissent à la surface des océans. La thèse commence avec un bref aperçu de l'analogie physique entre la localisation d'onde dans les systèmes hydrodynamique et les systèmes optique, pour lesquels nous décrivons les mécanismes de génération de vagues scélérates linéaire et non-linéaire. Nous présentons ensuite quelques résultats numérique et expérimentaux de la génération de vagues scélérates dans un système optique linéaire dans le cas d'une propagation spatiale d'un champ optique qui présente une phase aléatoire, où nous interprétons les résultats obtenus en terme de caustiques optiques localisées. Nous considérons ensuite les vagues scélérates obtenues dans des systèmes non-linéaires qui présentent une instabilité de modulation décrite par l'équation de Schrödinger non-linéaire (ESNL). Nous présentons une étude numérique détaillée comparant les caractéristiques spatio-temporelles des structures localisées obtenues dans les simulation numérique avec les différentes solutions analytiques obtenues à partir de l'ESNL. Deux études expérimentales d'instabilités de modulation sont ensuite effectuées. Dans la première, nous présentons des résultats expérimentaux qui étudient les propriétés d'instabilité de modulation en utilisant un système d'agrandissement temporel par lentille temporelle; dans la deuxième, nous rapportons des résultats expérimentaux sur les propriétés des instabilités de modulation dans le domaine fréquentiel en utilisant une technique de mesure spectrale en temps-réel. Cette dernière étude examine l'effet sur la bande spectrale et sur la stabilité d'un faible champ perturbateur. Tous les résultats expérimentaux sont comparés avec la simulation d'ESNL et abordés en termes des propriétés qualitatives d'instabilité de modulation. Dans toutes ces études, différentes propriétés statistiques sont analysées en rapport avec l'apparition des vagues scélérates.

Mots-clés : Vague Scélérates, Événments Extrêmes, Instabilité de Modulation, Équation de Schrödinger non-linéaire, Optique non-linéaire ultra-rapide, Fibre Optique, Tavelures Optiques, Caustique Optique

Abstract:

This thesis describes the study of several different classes of linear and nonlinear effects in optics that generate large amplitude extreme events with properties analogous to the destructive “rogue waves” on the surface of the ocean. The thesis begins with a brief overview of the analogous physics of wave localisation in hydrodynamic and optical systems, where we describe linear and nonlinear rogue wave generating mechanisms in both cases. We then present numerical and experimental results for rogue wave generation in a linear optical system consisting of free space propagation of a spatial optical field with random phase. Computed statistics between experiment and modelling are in good agreement, and we interpret the results obtained in terms of the properties of localised optical caustics. We then consider rogue waves in the nonlinear system of modulation instability described by the Nonlinear Schrodinger Equation (NLSE), and a detailed numerical study is presented comparing the spatio-temporal characteristics of localised structures seen from numerical simulations with different known analytic solutions to the NLSE. Two experimental studies of modulation instability are then reported. In the first, we present experimental results studying the properties of modulation instability using a time-lens magnifier system; in the second, we report experimental results studying the frequency-domain properties of modulation instability using real-time spectral measurements. The latter study examines the effect of a weak seed field on spectral bandwidth and stability. All experimental results are compared with the NLSE simulations and discussed in terms of the qualitative properties of modulation instability, in order to gain new insights into the complex dynamics associated with nonlinear pulse propagation. In all of these studies, different statistical properties are analised in relation to the emergence of rogue waves.

Keywords: Rogue Waves, Extreme Events, Modulation Instability, Nonlinear Schrödinger equation, Ultrafast nonlinear optics, Fibre Optics, Optical Speckle, Optical Caustics

SPIM

■ École doctorale SPIM 16 route de Gray F - 25030 Besançon cedex

■ tél. +33 (0)3 81 66 66 02 ■ ed-spim@univ-fcomte.fr ■ www.ed-spim.univ-fcomte.fr

UFC
UNIVERSITÉ
DE FRANCHE-COMTÉ